

**Synthesis of MoS<sub>2</sub> Incorporated Copper Cobalt Sulphide  
Nanocomposites and Investigation of Their Structural and  
Electrochemical Properties**

by

Sajjad Hasan

MASTER OF SCIENCE IN PHYSICS

Department of Physics





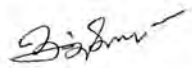
BANGLADESH UNIVERSITY OF ENGINEERING AND TECHNOLOGY

December 2021

## Certification

This thesis titled “Synthesis of MoS<sub>2</sub> Incorporated Copper Cobalt Sulphide Nanocomposites and Investigation of Their Structural and Electrochemical Properties” submitted by Sajjad Hasan, Roll No: 1018142507F Session: October–2018 has been accepted as satisfactory in partial fulfillment of the requirement for the degree MASTER OF SCIENCE IN PHYSICS on 11 December, 2021.

### BOARD OF EXAMINERS

- (  )  
1. Dr. Mohammed Abdul Basith (Supervisor) Chairman  
Professor  
Department of Physics, BUET, Dhaka-1000
- (  )  
2. Dr. Md. Rafi Uddin Member  
Professor & Head (Ex-Officio)  
Department of Physics, BUET, Dhaka-1000
- (  )  
3. Dr. Md. Forhad Mina Member  
Professor  
Department of Physics, BUET, Dhaka-1000
- (  )  
4. Dr. Md. Azizar Rahman Member  
Associate Professor  
Department of Physics, BUET, Dhaka-1000
- (  )  
5. Dr. A. B. M. Obaidul Islam Member  
Professor (External)  
Department of Physics, University of Dhaka, Dhaka

## Declaration

It is hereby declared that this thesis or any part of it has not been submitted elsewhere for the award of any degree or diploma.

سجاد حسن

Sajjad Hasan

## Dedication

*To my parents.  
For their support, sacrifice, inspiration, love and affection.*

## Acknowledgements

I want to take this opportunity to thank everyone who made this work possible.

With pleasure, I express my sincerest gratitude to my supervisor Dr. Mohammed Abdul Basith, Professor, Department of Physics, Bangladesh University of Engineering and Technology (BUET), for his supervision and continuous encouragement during the whole period of this research. My sincere thankfulness to Professor Basith for frequently providing the required corrections, valuable suggestions, and worthy comments during the writing up of this thesis.

My gratitude to Professor Dr. Md. Rafi Uddin, Head, Department of Physics, BUET, for ensuring all administrative support during this degree program. I want to convey my deep gratitude to all other respected teachers of the Department of Physics, BUET, for their kind cooperation.

My sincere gratefulness to Md. Akter Hossain Reaz and Subrata Das for their support in the analysis of the results and discussion. I would also like to thank Manifa Noor for helping me with the Rietveld refinement via the X'Pert High-Score Plus software package. My heartiest gratitude to Dr. Chanchal Kumar Roy, Assistant Professor, Department of Chemistry, BUET, for allowing me to use the electrochemical workstation during this pandemic.

I want to acknowledge the Committee for Advanced Studies and Research (CASR), BUET, for sincerely providing the required financial grant for this research. I am thankful to the Department of Glass and Ceramic Engineering, BUET, and Atomic Energy Commission, Dhaka, for providing me the FESEM and XRD facilities. I greatly appreciate the Ministry of Science and Technology of Bangladesh for providing me National Science and Technology Fellowship for the year 2019-2020.

I want to thank all the members of the Nanotechnology Research Laboratory for supporting me during the whole period of my study.

Finally, I would like to thank my family members, especially my parents, for their love, support, and blessings. And lastly, I want to convey my gratitude towards Urbi Shyamolima Orchi for her constant motivation.

## Abstract

In the present investigation, MoS<sub>2</sub> incorporated CuCo<sub>2</sub>S<sub>4</sub> nanocomposite has been successfully synthesized by a hydrothermal technique. High resolution transmission electron microscopy imaging demonstrated the successful synthesis of CuCo<sub>2</sub>S<sub>4</sub>-MoS<sub>2</sub> nanocomposite. The electrochemical capacitor performance of the nanocomposite has been evaluated both in three-electrode and symmetric two-electrode systems. In the three-electrode cell, a specific capacitance of 820 Fg<sup>-1</sup> was achieved for CuCo<sub>2</sub>S<sub>4</sub>-MoS<sub>2</sub> electrode at the current density of 0.5 Ag<sup>-1</sup> which is considerably higher than that of CuCo<sub>2</sub>S<sub>4</sub> electrode (249 Fg<sup>-1</sup>). It was observed that the charge storage capacity, conductivity and stability of CuCo<sub>2</sub>S<sub>4</sub> had improved significantly due to the incorporation of MoS<sub>2</sub>. Finally, an asymmetric supercapacitor was fabricated by assembling the CuCo<sub>2</sub>S<sub>4</sub>-MoS<sub>2</sub> electrode with an activated carbon electrode which demonstrated a large stable working potential window of 1.6 V. A long-term cyclic stability of 89% retention after 1000 galvanostatic charge-discharge cycles were found. As a solid state device, it delivered a high energy density of 38.22 Whkg<sup>-1</sup> at a power density of 400 Wkg<sup>-1</sup> and lit up one red LED for 290 s, indicating its superiority over the conventional CuCo<sub>2</sub>S<sub>4</sub> based supercapacitors.

# Contents

Candidate's declaration	iii
Dedication	iv
Acknowledgements	v
Abstract	vi
List of figures	ix
List of tables	xiii
List of abbreviations	xiv
<b>CHAPTER 1: INTRODUCTION</b>	<b>1</b>
1.1 Background . . . . .	1
1.2 Objectives of the Present Study . . . . .	2
1.3 Outline of the Thesis . . . . .	3
<b>CHAPTER 2: LITERATURE REVIEW AND THEORETICAL ASPECTS</b>	<b>4</b>
2.1 The $\text{CuCo}_2\text{S}_4$ as Electrode Material . . . . .	4
2.2 The Composite of $\text{CuCo}_2\text{S}_4$ Based Electrode . . . . .	10
2.3 Fundamental of Electrochemistry in Energy Storage . . . . .	14
2.3.1 Supercapacitor . . . . .	14
2.3.2 Mechanism of supercapacitor . . . . .	15
2.3.2.1 Electrochemical double-layer capacitor . . . . .	15
2.3.2.2 Pseudo-capacitor . . . . .	16
2.3.2.3 Hybrid capacitor . . . . .	17
<b>CHAPTER 3: MATERIALS AND METHODS</b>	<b>18</b>
3.1 Sample Preparation . . . . .	18
3.1.1 Synthesis of nanostructured $\text{CuCo}_2\text{S}_4$ . . . . .	18
3.1.2 Synthesis of $\text{CuCo}_2\text{S}_4$ - $\text{MoS}_2$ nanocomposite . . . . .	19
3.2 Structural Characterisation Techniques . . . . .	19
3.2.1 X-ray diffraction . . . . .	19
3.2.2 Rietveld refinement . . . . .	21

3.3	Morphological and Elemental Composition Analyses Techniques . . . . .	22
3.3.1	Field Emission Scanning Electron Microscopy . . . . .	22
3.3.2	Transmission Electron Microscopy . . . . .	24
3.3.3	Fourier Transform Infrared Spectroscopy . . . . .	25
3.4	Electrochemical Characterisation Techniques . . . . .	27
3.4.1	Electrochemical cell setup . . . . .	27
3.4.1.1	Three-electrode system . . . . .	28
3.4.1.2	Two-electrode system . . . . .	28
3.4.2	Preparation of electrodes . . . . .	29
3.4.3	Cyclic Voltammetry . . . . .	30
3.4.4	Galvanostatic Charge-Discharge . . . . .	31
3.4.5	Electrochemical Impedance Spectroscopy . . . . .	32
3.4.6	Determination of energy density and power density . . . . .	33
<b>CHAPTER 4: RESULTS AND DISCUSSION</b>		<b>35</b>
4.1	Structural, Morphological and Elemental Characterisations . . . . .	35
4.1.1	Crystal structure . . . . .	35
4.1.2	Surface morphology . . . . .	37
4.1.3	Chemical composition . . . . .	40
4.2	Electrochemical Performance . . . . .	42
4.2.1	Electrochemical performance in three-electrode system . . . . .	42
4.2.2	Electrochemical performance in symmetric two-electrode system . . . . .	48
4.2.3	Electrochemical performance of the asymmetric CuCo <sub>2</sub> S <sub>4</sub> - MoS <sub>2</sub> //AC device . . . . .	57
<b>CHAPTER 5: SUMMARY AND CONCLUSIONS</b>		<b>64</b>
5.1	Summary . . . . .	64
5.2	Conclusions . . . . .	65
5.3	Scope for Future Work . . . . .	65
<b>References</b>		<b>67</b>
<b>List of publications</b>		<b>77</b>



## List of figures

<b>Fig. 2.1</b>	Scanning electron microscopy images of (a) $\text{CuCo}_2\text{S}_4$ -Water, (b) $\text{CuCo}_2\text{S}_4$ -Glycol and (c) $\text{CuCo}_2\text{S}_4$ -Glycerol ; (d) Nitrogen adsorption/desorption isotherms of $\text{CuCo}_2\text{S}_4$ -Water, $\text{CuCo}_2\text{S}_4$ -Glycol and $\text{CuCo}_2\text{S}_4$ -Glycerol. . . . .	5
<b>Fig. 2.2</b>	(a) Cyclic voltammetry curves at $5 \text{ mVs}^{-1}$ , (b) galvanostatic charge-discharge curves at $20 \text{ Ag}^{-1}$ and (c) electrochemical impedance spectroscopy plots of $\text{CuCo}_2\text{S}_4$ -Water, $\text{CuCo}_2\text{S}_4$ -Glycol and $\text{CuCo}_2\text{S}_4$ -Glycerol; (d) cycling performances of $\text{CuCo}_2\text{S}_4$ -Glycerol electrode at $70 \text{ Ag}^{-1}$ for 2000 cycles. . . . .	6
<b>Fig. 2.3</b>	(a) The specific capacitance of the as-prepared three $\text{CuCo}_2\text{S}_4$ electrodes (b) The cycling stability of the as-prepared three $\text{CuCo}_2\text{S}_4$ electrodes at a current density of $3 \text{ Ag}^{-1}$ . . . . .	7
<b>Fig. 2.4</b>	Scanning electron microscopy image of (a) $\text{CuCo}_2\text{S}_4$ (Water) (b) $\text{CuCo}_2\text{S}_4$ (Water/Ethanol) and (c) $\text{CuCo}_2\text{S}_4$ (Ethanol). . . . .	8
<b>Fig. 2.5</b>	Scanning electron microscopy images of $\text{CuCo}_2\text{S}_4$ materials under different magnifications, (a,b) CCS-RT, (c,d) CCS-100, (e,f) CCS-150, (g,h) CCS-200. . . . .	9
<b>Fig. 2.6</b>	Temperature dependence of specific capacitance of $\text{CuCo}_2\text{S}_4$ electrodes with increasing current density. . . . .	10
<b>Fig. 2.7</b>	Scanning electron microscopy image of (a) GA, (b-c) $\text{CuCo}_2\text{S}_4$ /GA, and in the inset of (c) $\text{CuCo}_2\text{S}_4$ . . . . .	11
<b>Fig. 2.8</b>	(a) Cyclic voltammetry curves at scan rate of $5 \text{ mVs}^{-1}$ ; (b) Galvanostatic charge-discharge curves at a current density of $1.0 \text{ Ag}^{-1}$ ; (c) Nyquist plots of $\text{CuCo}_2\text{S}_4$ @ $\text{NiCo}_2\text{S}_4$ , $\text{CuCo}_2\text{S}_4$ , and $\text{NiCo}_2\text{S}_4$ electrodes in 3 M KOH; (d) cyclic voltammetry curves of the $\text{CuCo}_2\text{S}_4$ @ $\text{NiCo}_2\text{S}_4$ composite at different scan rates in 3 M KOH; (e) The specific capacity of $\text{CuCo}_2\text{S}_4$ nanoneedles arrays, $\text{NiCo}_2\text{S}_4$ nanosheet array and composite structure at various current densities, respectively; (f) The cyclic performance of $\text{CuCo}_2\text{S}_4$ @ $\text{NiCo}_2\text{S}_4$ composite structure at the current density of $8 \text{ Ag}^{-1}$ for 5000 continuous cycles. . . . .	12

<b>Fig. 2.9</b>	Morphological evolution of the 3D flower-like $\text{CuCo}_2\text{S}_4/\text{CuCo}_2\text{O}_4$ with increasing feeding amount of TAA. (a–d) Scanning electron microscopy images of the mesoporous $\text{CuCo}_2\text{S}_4/\text{CuCo}_2\text{O}_4$ -0, $\text{CuCo}_2\text{S}_4/\text{CuCo}_2\text{O}_4$ -1, $\text{CuCo}_2\text{S}_4/\text{CuCo}_2\text{O}_4$ -4 and $\text{CuCo}_2\text{S}_4/\text{CuCo}_2\text{O}_4$ , respectively. . . . .	13
<b>Fig. 2.10</b>	Electrochemical performances of the samples for supercapacitors. (a) Cyclic voltammetry curves at a scan rate of $10 \text{ mVs}^{-1}$ for all the samples. (b) Galvanostatic charge-discharge curves at a current density of $1 \text{ Ag}^{-1}$ for all the samples. (c) Specific capacity versus feeding amount of TAA at $1 \text{ Ag}^{-1}$ (d) electrochemical impedance spectroscopy spectra of the 3D flower-like $\text{CuCo}_2\text{S}_4/\text{CuCo}_2\text{O}_4$ electrodes. (e) The specific capacities of the 3D flower-like $\text{CuCo}_2\text{S}_4/\text{CuCo}_2\text{O}_4$ electrodes at different current density. (f) Cycling performance at a current density of $20 \text{ Ag}^{-1}$ . . . . .	14
<b>Fig. 2.11</b>	Schematic of electrochemical double-layer capacitor structure. . . . .	16
<b>Fig. 2.12</b>	Three typical types of pseudo-capacitive reactions. (a) Under-potential deposition: electro-deposition of Pb thin films onto Au substrate. (b) Near-surface redox reactions: protonation and de-protonation of $\text{RuO}_2$ in aprotic electrolytes. (c) Fast ion insertion-deinsertion. . . . .	17
<b>Fig. 3.1</b>	Schematics of the synthesis steps of $\text{CuCo}_2\text{S}_4\text{-MoS}_2$ nanocomposite using a hydrothermal technique. . . . .	18
<b>Fig. 3.2</b>	Schematic illustration of X-ray diffractometer instrument. . . . .	20
<b>Fig. 3.3</b>	Schematic diagram of a Field Emission Scanning Electron Microscope. . . . .	22
<b>Fig. 3.4</b>	Schematic view of imaging and diffraction modes in TEM. . . . .	24
<b>Fig. 3.5</b>	Schematic diagram of Fourier Transform Infrared spectroscope. . . . .	26
<b>Fig. 3.6</b>	(a) A three-electrode system where the potential difference is measured between WE and RE, while the current passes between WE and CE. (b) A two-electrode system, where both the potential difference and current are measured between the WE and the CE/RE. . . . .	27
<b>Fig. 3.7</b>	Typical cyclic voltammogram where $i_{pa}$ and $i_{pc}$ show the peak of anodic and cathodic current respectively for a reversible reaction. . . . .	30
<b>Fig. 3.8</b>	Effect of (a) change of current and (b) potential response on electrode materials in GCD. . . . .	31
<b>Fig. 3.9</b>	Potential response of an ideal electrochemical capacitor in GCD. . . . .	32

<b>Fig. 3.10</b>	(a) A typical Nyquist plot and (b) its equivalent circuit. . . . .	33
<b>Fig. 4.1</b>	Rietveld refined powder XRD patterns of (a) $\text{CuCo}_2\text{S}_4$ and (b) $\text{CuCo}_2\text{S}_4\text{-MoS}_2$ . . . . .	35
<b>Fig. 4.2</b>	FESEM images of (a) $\text{CuCo}_2\text{S}_4$ and (b) $\text{CuCo}_2\text{S}_4\text{-MoS}_2$ . . . . .	38
<b>Fig. 4.3</b>	(a and b) TEM images of $\text{CuCo}_2\text{S}_4\text{-MoS}_2$ (c) HRTEM image of $\text{CuCo}_2\text{S}_4\text{-MoS}_2$ with lattice fringes of $\text{MoS}_2$ indicated in bottom left inset and lattice fringes of $\text{CuCo}_2\text{S}_4$ indicated in bottom right inset and (d) SAED pattern of $\text{CuCo}_2\text{S}_4\text{-MoS}_2$ . . . . .	39
<b>Fig. 4.4</b>	EDX spectra of (a) $\text{CuCo}_2\text{S}_4$ and (b) $\text{CuCo}_2\text{S}_4\text{-MoS}_2$ . . . . .	40
<b>Fig. 4.5</b>	FTIR spectra of $\text{CuCo}_2\text{S}_4$ and $\text{CuCo}_2\text{S}_4\text{-MoS}_2$ . Inset showed the full FTIR spectra obtained for wavenumber ranging from $400\text{ cm}^{-1}$ to $4000\text{ cm}^{-1}$ . . . . .	41
<b>Fig. 4.6</b>	Electrochemical performance of $\text{MoS}_2$ , $\text{CuCo}_2\text{S}_4$ and $\text{CuCo}_2\text{S}_4\text{-MoS}_2$ electrodes in three-electrode system: (a) CV curves at a fixed scan rate of $20\text{ mVs}^{-1}$ , (b) GCD curves at a fixed current density of $0.5\text{ Ag}^{-1}$ (c) variation of $C_{\text{sp}}$ ( $\text{Fg}^{-1}$ ) with increasing current densities and (d) Nyquist plots. . . . .	43
<b>Fig. 4.7</b>	Electrochemical behaviour of $\text{MoS}_2$ measured in three-electrode system in aqueous electrolyte ( $0.5\text{ M Na}_2\text{SO}_4$ ) within the potential range of $-0.5$ to $0.5\text{ V}$ ; (a) CV curves at various scan rates and (b) GCD curves at different current densities. . . . .	44
<b>Fig. 4.8</b>	Electrochemical behavior of $\text{CuCo}_2\text{S}_4$ measured in three-electrode system in aqueous electrolyte ( $0.5\text{ M Na}_2\text{SO}_4$ ) within the potential range of $-0.5$ to $0.5\text{ V}$ ; (a) CV curves at various scan rates and (b) GCD curves at different current densities. . . . .	45
<b>Fig. 4.9</b>	Electrochemical behaviour of $\text{CuCo}_2\text{S}_4\text{-MoS}_2$ measured in three-electrode system in aqueous electrolyte ( $0.5\text{ M Na}_2\text{SO}_4$ ) within the potential range of $-0.5$ to $0.5\text{ V}$ ; (a) CV curves at various scan rates and (b) GCD curves at different current densities. . . . .	46
<b>Fig. 4.10</b>	Potential window variation of (a) $\text{CuCo}_2\text{S}_4$ and (b) $\text{CuCo}_2\text{S}_4\text{-MoS}_2$ electrodes in two-electrode system. . . . .	49
<b>Fig. 4.11</b>	Electrochemical performance of $\text{CuCo}_2\text{S}_4$ and $\text{CuCo}_2\text{S}_4\text{-MoS}_2$ electrodes in two-electrode system: (a) CV curves at a fixed scan rate of $20\text{ mVs}^{-1}$ , (b) GCD curves at a fixed current density $0.5\text{ Ag}^{-1}$ (c) variation of $C_{\text{sp}}$ ( $\text{Fg}^{-1}$ ) with increasing current densities and (d) Nyquist plots. . . . .	50

<b>Fig. 4.12</b>	Electrochemical behavior of $\text{CuCo}_2\text{S}_4$ measured in symmetric two-electrode system in aqueous electrolyte (1 M $\text{Na}_2\text{SO}_4$ ) within the potential range of 0 to 0.7 V; (a) CV curves at various scan rates and (b) GCD curves at different current densities. . .	51
<b>Fig. 4.13</b>	Electrochemical behavior of $\text{CuCo}_2\text{S}_4\text{-MoS}_2$ measured in symmetric two-electrode system in aqueous electrolyte (1 M $\text{Na}_2\text{SO}_4$ ) within the potential range of 0 to 0.7 V; (a) CV curves at various scan rates and (b) GCD curves at different current densities. . . . .	52
<b>Fig. 4.14</b>	Retention of specific capacitance of $\text{CuCo}_2\text{S}_4$ and $\text{CuCo}_2\text{S}_4\text{-MoS}_2$ electrodes at $5 \text{ Ag}^{-1}$ . . . . .	54
<b>Fig. 4.15</b>	Ragone plot of $\text{CuCo}_2\text{S}_4$ and $\text{CuCo}_2\text{S}_4\text{-MoS}_2$ . . . . .	55
<b>Fig. 4.16</b>	Schematic illustration of charge storage mechanism at the $\text{CuCo}_2\text{S}_4\text{-MoS}_2$ nanocomposite in symmetric two-electrode system. . . . .	56
<b>Fig. 4.17</b>	Electrochemical performance of $\text{CuCo}_2\text{S}_4\text{-MoS}_2//\text{AC}$ asymmetric device: (a) CV curves at a various scan rates, (b) GCD curves at various current densities , (c) variation of $C_{\text{sp}}$ ( $\text{F g}^{-1}$ ) with increasing current densities and (d) Nyquist plots. . . . .	58
<b>Fig. 4.18</b>	Retention of specific capacitance retention of $\text{CuCo}_2\text{S}_4\text{-MoS}_2//\text{AC}$ asymmetric device. . . . .	59
<b>Fig. 4.19</b>	Ragone plot of $\text{CuCo}_2\text{S}_4\text{-MoS}_2//\text{AC}$ asymmetric device. . . . .	60
<b>Fig. 4.20</b>	Snapshots of a practical demonstration of $\text{CuCo}_2\text{S}_4\text{-MoS}_2//\text{AC}$ device containing prototype supercapacitor system; (a) snapshots of the device setup and connection of the real device for charging. (b-f) photographs of the LED to monitor the discharge process at various times. . . . .	63

## List of tables

<b>Table 4.1</b>	Crystallographic parameters for all the constituents of the nanomaterials obtained after refinement. . . . .	36
<b>Table 4.2</b>	Mass and atom percentages of elements in $\text{CuCo}_2\text{S}_4$ and $\text{CuCo}_2\text{S}_4\text{-MoS}_2$ as obtained via EDX and theoretical analysis. . . . .	41
<b>Table 4.3</b>	Values of $R_s$ , $R_{ct}$ , $C_{dl}$ , $Z_W$ and $C_p$ in the three-electrode system obtained by fitting with equivalent circuit. . . . .	48
<b>Table 4.4</b>	Values of $R_s$ , $R_{ct}$ , $C_{dl}$ , $Z_W$ and $C_p$ in the symmetric two-electrode system obtained by fitting with equivalent circuit. . . . .	53
<b>Table 4.5</b>	Values of $R_s$ , $R_{ct}$ , $C_{dl}$ , $Z_W$ and $C_p$ of $\text{CuCo}_2\text{S}_4\text{-MoS}_2$ in the asymmetric two-electrode system obtained by fitting with equivalent circuit. . . . .	59
<b>Table 4.6</b>	Comparison of the asymmetric performance $\text{CuCo}_2\text{S}_4\text{-MoS}_2$ based on previous investigations. . . . .	61

## List of abbreviations

<b>AC</b>	Activated carbon
<b>BET</b>	Brunauer–Emmett–Teller
<b>CV</b>	Cyclic Voltammetry
<b>EDLC</b>	Electrochemical double layer capacitance
<b>EDX</b>	Energy-dispersive X-ray
<b>EIS</b>	Electrochemical Impedance Spectroscopy
<b>FESEM</b>	Field Emission Scanning Electron Microscopy
<b>FTIR</b>	Fourier Transform Infrared Spectroscopy
<b>GCD</b>	Galvanostatic Charge-Discharge
<b>HRTEM</b>	High-resolution Transmission Electron Microscopy
<b>RT</b>	Room Temperature
<b>SAED</b>	Selected Area Electron Diffraction
<b>TEM</b>	Transmission Electron Microscopy
<b>TMSs</b>	Transition-metal sulfides
<b>XRD</b>	X-ray diffraction

# CHAPTER 1

## INTRODUCTION

### 1.1 Background

Over the last few decades, a significant amount of scientific endeavour has been undertaken for the advancement of high-performance energy storage and conversion systems to meet the requirement for sustainable and portable power sources [1–4]. Recently, the supercapacitor has emerged as a fascinating electrochemical energy storage device for automobile and electronic applications owing to its high-power density, fast charge-discharge rate, large capacity, long lifespan, wide range of operating temperatures, high-safety performance and low cost [5–7]. However, the widespread application of supercapacitors has not been possible yet because of their low-energy density [4, 8–10] since high energy density is essential for long-duration application like battery. Several recent investigations [9, 11] reported that designing and tailoring the type, morphology and architecture of the electrode material can be beneficial for improving the energy storage capacity of supercapacitors. Nevertheless, it is still quite challenging to rationally design novel electrode materials and improve the energy density without compromising power density.

In recent times, transition-metal sulphides (TMSs) are being investigated as a promising electrode materials for supercapacitors because of their complex valence states and large crystal lattice values [5, 6]. Notably, TMSs possess higher electrical conductivity, lower electronegativity and smaller band gap compared to their oxide counterparts which result in superior electrochemical performance with favourable redox reactions [6, 12]. Especially, ternary transition metal sulphides such as  $\text{NiCo}_2\text{S}_4$  [9],  $\text{MnCo}_2\text{S}_4$  [13],  $\text{CuCo}_2\text{S}_4$  [7],  $\text{ZnCo}_2\text{S}_4$  [14],  $\text{FeCo}_2\text{S}_4$  [15] have exhibited improved electrical conductivity, enhanced redox sites and enormous oxidation states owing to the synergistic effect of hetero-metal ions in single compound. Among them,  $\text{CuCo}_2\text{S}_4$  has attracted special attention because of copper's natural abundance, low cost and ability to compensate volume expansion during electrochemical process [7]. However, the electrical conductivity, stability and specific capacitance of  $\text{CuCo}_2\text{S}_4$  electrode are still to be improved for practical applications. Also, the self-agglomeration along with the volume change at the time of charge/discharge processes are the major drawbacks of  $\text{CuCo}_2\text{S}_4$  which must be reduced to enhance its electrochemical performance [16–18].

In this regard, the incorporation of two dimensional (2D) nanomaterials might be competent strategy to circumvent the obstacle of pure  $\text{CuCo}_2\text{S}_4$  having low surface area and inefficient electrons/ions transport capability [5, 10, 12, 19]. For this, 2D layered transition metal dichalcogenide,  $\text{MoS}_2$  with high specific surface area appears to be a promising candidate owing to its high intrinsic fast ionic conductivity, large specific capacity of  $1504 \text{ Fg}^{-1}$  and ability to prevent self-agglomeration of  $\text{CuCo}_2\text{S}_4$  [20–23]. The sheet like morphology of  $\text{MoS}_2$  promotes ion insertion between its layers resulting in high charge storage capacity and large electrochemical double layer capacitance (EDLC). Additionally,  $\text{MoS}_2$  possesses notable pseudocapacitance ability since the central Mo ion has various oxidation states from +2 to +6 [23]. Moreover, owing to the diffusion of the electrolyte ions into the layers of  $\text{MoS}_2$ , it can provide a faradaic capacitance even at lower scan rates [24, 25]. As a result, it is highly likely that  $\text{CuCo}_2\text{S}_4$ - $\text{MoS}_2$  will demonstrate enhanced specific capacitance and improved rate capability owing to the synergistic interaction [26] between  $\text{CuCo}_2\text{S}_4$  and  $\text{MoS}_2$ . Moreover, the presence of S in both  $\text{CuCo}_2\text{S}_4$  and  $\text{MoS}_2$  can create a strong connection between the individual materials which can improve the electrochemical stability of the nanocomposite [23]. In addition, the void space between the layers of  $\text{MoS}_2$  might help to endure the volume expansion of  $\text{CuCo}_2\text{S}_4$  during cycling process [27]. However, the role of  $\text{MoS}_2$  as a supporting matrix for  $\text{CuCo}_2\text{S}_4$  electrode has not been reported yet.

## 1.2 Objectives of the Present Study

The main objectives of the investigation with specific aims are as follows:

- i. Preparation of  $\text{CuCo}_2\text{S}_4$  and  $\text{CuCo}_2\text{S}_4$ - $\text{MoS}_2$  nanocomposite via hydrothermal method at a suitable reaction temperature.
- ii. Determination of crystallographic structure and parameters of the as-prepared  $\text{CuCo}_2\text{S}_4$  and  $\text{CuCo}_2\text{S}_4$ - $\text{MoS}_2$  using powder X-ray diffraction technique.
- iii. Analyses of surface morphology and chemical composition of the synthesised  $\text{CuCo}_2\text{S}_4$  and  $\text{CuCo}_2\text{S}_4$ - $\text{MoS}_2$  using field emission scanning electron microscope imaging technique. Investigation of the crystallinity of the as-synthesised samples using transmission electron microscope imaging technique.
- iv. Investigation of chemical bonding of  $\text{CuCo}_2\text{S}_4$  and  $\text{CuCo}_2\text{S}_4$ - $\text{MoS}_2$  by Fourier transform infrared spectroscopy.
- v. Analysis of electrochemical properties of  $\text{CuCo}_2\text{S}_4$  and  $\text{CuCo}_2\text{S}_4$ - $\text{MoS}_2$  nanocomposite by cyclic voltammetry, galvanostatic charge-discharge, and



electrochemical impedance spectroscopy using an electrochemical workstation in three-electrode and symmetric as well as asymmetric two-electrode systems.

### 1.3 Outline of the Thesis

This thesis contains the following chapters

- i. In this **Chapter** background, motivation, and objectives of the investigation were presented.
- ii. **Chapter 2** is comprised of literature reviews from some previous relevant works done by different research groups.
- iii. **Chapter 3** described the methodology of sample preparation and brief descriptions of characterisation techniques used to determine various properties.
- iv. **Chapter 4** presented results and discussion in detail.
- v. **Chapter 5** provided a summary of the research findings with concluding remarks.

## CHAPTER 2

### LITERATURE REVIEW AND THEORETICAL ASPECTS

In this chapter, initially, the morphology, crystallinity, and electrochemical performance of  $\text{CuCo}_2\text{S}_4$  were discussed. Later on, the composites of  $\text{CuCo}_2\text{S}_4$  and their electrochemical properties were presented.

#### 2.1 The $\text{CuCo}_2\text{S}_4$ as Electrode Material

Implementation of  $\text{CuCo}_2\text{S}_4$  as an electrode material for the electrochemical capacitor is new even though significant research was carried out on copper containing ternary-metal sulphide [28, 29]. Since the electrochemical performances of  $\text{CuCo}_2\text{S}_4$  were affected by the particle size, morphology, structure, and storing charges in the surface,  $\text{CuCo}_2\text{S}_4$  materials with plenty of mesopores and small particle sizes were favoured to use as electrode material [30–34]. Different research groups had taken different approaches to improving the morphology, crystallinity, conductivity, capacity, and stability of the  $\text{CuCo}_2\text{S}_4$  [35–38].

A number of previous investigations [30, 33, 34] had concluded that the reaction medium had a considerable impact on the degree of crystallinity of  $\text{CuCo}_2\text{S}_4$ . In 2016, Tang *et al.* [30] reported the effect of crystallinity on the electrochemical performance of  $\text{CuCo}_2\text{S}_4$ . The authors observed that synthesis of  $\text{CuCo}_2\text{S}_4$  in different solvents showed the highest degree of crystallisation for  $\text{CuCo}_2\text{S}_4$ -Water followed by  $\text{CuCo}_2\text{S}_4$ -Glycol and  $\text{CuCo}_2\text{S}_4$ -Glycerol. The low viscosity of water helped the crystal growth process in water than glycerol and glycol [31]. Scanning electron microscopy imaging revealed that all the samples in different solvents had similar morphologies comprising numerous irregular nanoparticles, as shown in Fig. 2.1. However, it was reported that  $\text{CuCo}_2\text{S}_4$ -Glycerol (Fig. 2.1 (b)) had less agglomeration than those of  $\text{CuCo}_2\text{S}_4$ -Glycol (Fig. 2.1 (a)) and  $\text{CuCo}_2\text{S}_4$ -Water (Fig. 2.1 (c)). Brunauer–Emmett–Teller (BET) analysis also confirmed that  $\text{CuCo}_2\text{S}_4$ -Glycerol had the highest specific surface area and  $\text{CuCo}_2\text{S}_4$ -Water had the lowest (Fig. 2.1 (d)). Hence, it is clear that, a solvent need to be modified to synthesis  $\text{CuCo}_2\text{S}_4$  with good crystallinity and morphology.

Analysing cyclic voltammetry and galvanostatic charge-discharge, shown in Fig. 2.2 (a and b), Tang *et al.* [30] also revealed that the  $\text{CuCo}_2\text{S}_4$ -Glycol, which obtained the highest capacitance ( $5030 \text{ Fg}^{-1}$  at a current density of  $20 \text{ Ag}^{-1}$ ). In comparison, the capacitance of  $\text{CuCo}_2\text{S}_4$ -Water was much smaller ( $2602 \text{ Fg}^{-1}$  at current density

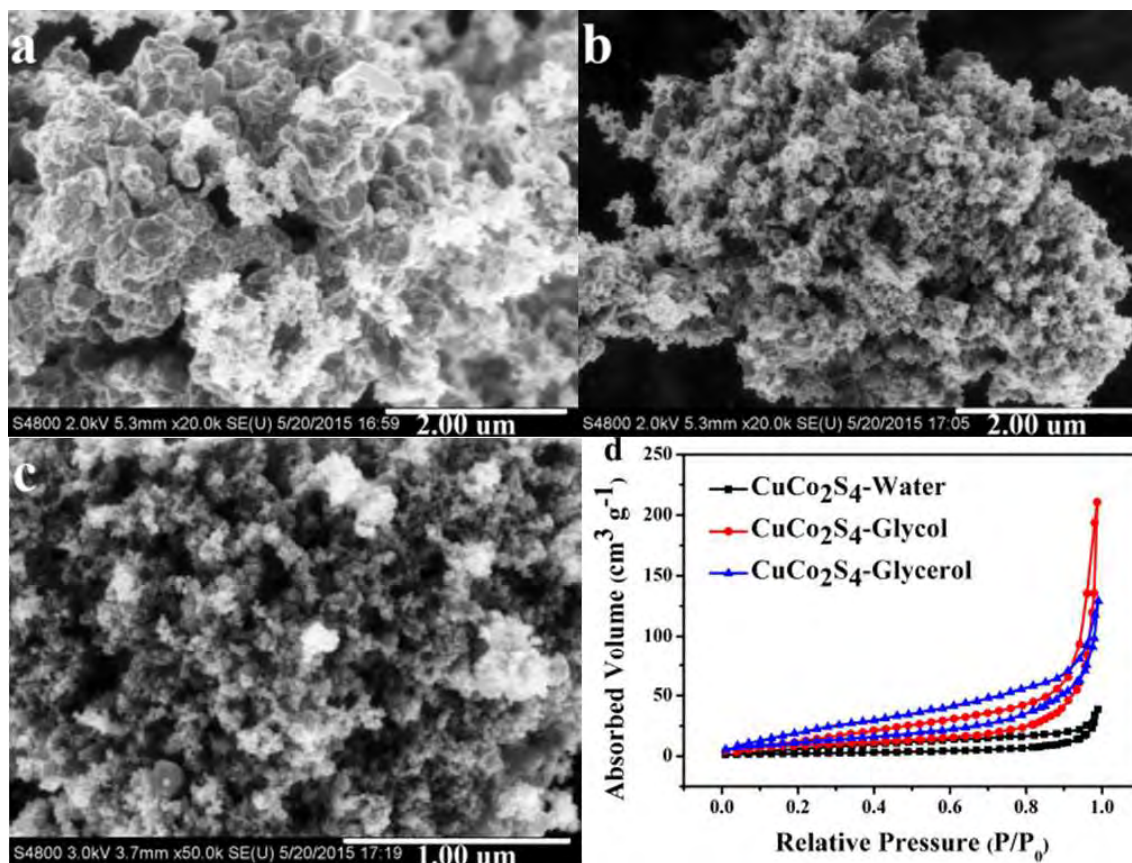


**Fig. 2.1** Scanning electron microscopy images of (a)  $\text{CuCo}_2\text{S}_4$ -Water, (b)  $\text{CuCo}_2\text{S}_4$ -Glycol and (c)  $\text{CuCo}_2\text{S}_4$ -Glycerol ; (d) Nitrogen adsorption/desorption isotherms of  $\text{CuCo}_2\text{S}_4$ -Water,  $\text{CuCo}_2\text{S}_4$ -Glycol and  $\text{CuCo}_2\text{S}_4$ -Glycerol [30].

of  $20 \text{ Ag}^{-1}$ ) owing to the serious agglomeration and small specific surface area. Electrochemical impedance spectroscopy (Fig. 2.2 (c)) also demonstrated that all the materials had low internal resistance indicating a high ion transfer and diffusion rate. However, the cyclic stability (Fig. 2.2 (d)) of  $\text{CuCo}_2\text{S}_4$ -Glycol, which had the highest specific capacitance than others, suffers from mediocre cyclic stability. The electrochemical performance was analysed in polysulphide electrolyte which is expensive, environment unfriendly. Even though it showed the potential of  $\text{CuCo}_2\text{S}_4$  as electrode material, the practical application is not feasible by this electrolyte.

Zhu *et al.* [33] reported in 2017 that morphology and particle size affect the electrochemical performance, which solvent might regulate. In that study,  $\text{CuCo}_2\text{S}_4$  was synthesized in water ( $\text{CuCo}_2\text{S}_4$ -water), a mixture (1:1) of water and ethylene glycol ( $\text{CuCo}_2\text{S}_4$ -water/EG), and a high concentration mixture (1:1) of water and ethylene glycol ( $\text{CuCo}_2\text{S}_4$ -water/EG (HC)). According to the morphological study, materials of  $\text{CuCo}_2\text{S}_4$ -water had a higher particle size than that of  $\text{CuCo}_2\text{S}_4$ -water/EG. The particle size was also more uniform for  $\text{CuCo}_2\text{S}_4$ -water/EG than that

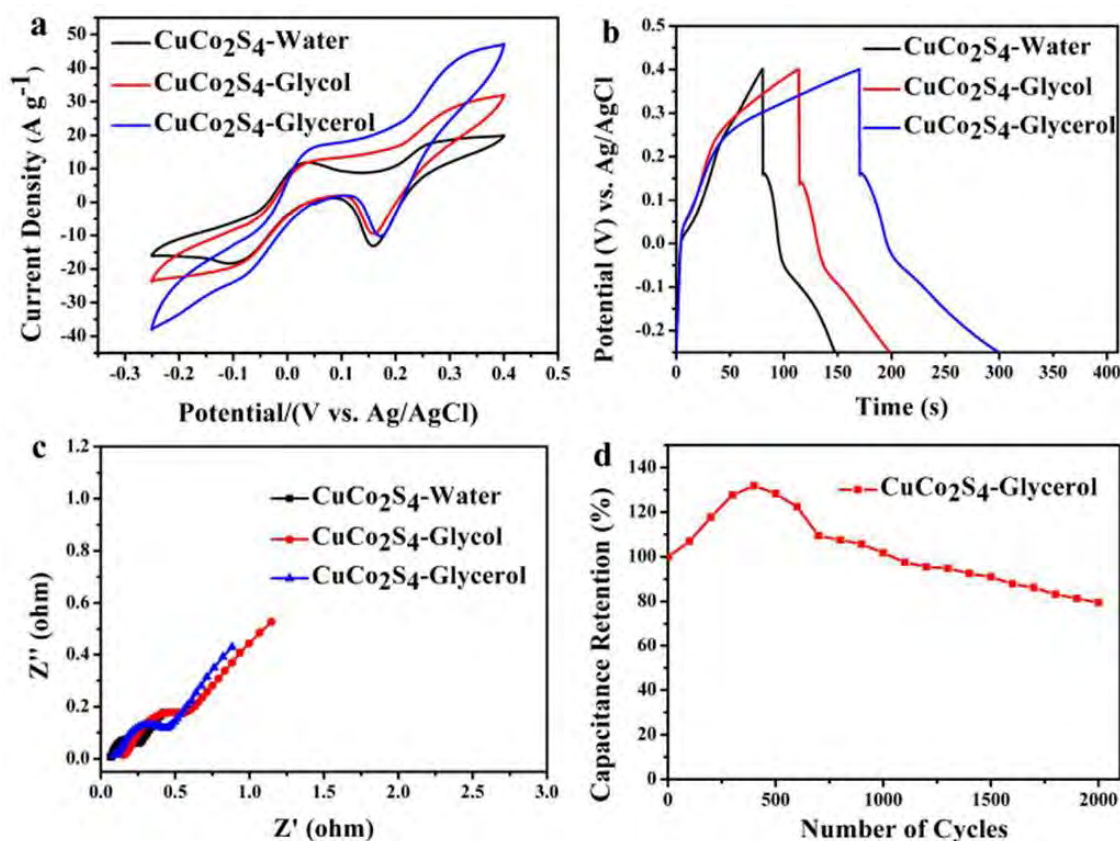


**Fig. 2.2** (a) Cyclic voltammograms at 5 mVs<sup>-1</sup>, (b) galvanostatic charge-discharge curves at 20 Ag<sup>-1</sup> and (c) electrochemical impedance spectroscopy plots of CuCo<sub>2</sub>S<sub>4</sub>-Water, CuCo<sub>2</sub>S<sub>4</sub>-Glycol and CuCo<sub>2</sub>S<sub>4</sub>-Glycerol; (d) cycling performances of CuCo<sub>2</sub>S<sub>4</sub>-Glycerol electrode at 70 Ag<sup>-1</sup> for 2000 cycles [30].

of CuCo<sub>2</sub>S<sub>4</sub>-water. It was reported that mild mixed solvent (EG/H<sub>2</sub>O) decreased the reaction rate compared to pure solvent (H<sub>2</sub>O), resulting in superior morphology and uniform particle size formation. Furthermore, the surface analysis also revealed that CuCo<sub>2</sub>S<sub>4</sub>-water/EG had the highest surface area and total pore volume than CuCo<sub>2</sub>S<sub>4</sub>-water. So, it is prominent that, to obtain a better morphology of CuCo<sub>2</sub>S<sub>4</sub>, a mixture of solvent is need to be used in synthesis process.

Zhu *et al.* [33] also reported that the electrochemical performance of CuCo<sub>2</sub>S<sub>4</sub>-water/EG was also higher than that of CuCo<sub>2</sub>S<sub>4</sub>-water. The comparison of specific capacitance and cyclic stability is shown in Fig. 2.3. The higher specific surface area of CuCo<sub>2</sub>S<sub>4</sub>-water/EG offered more electrochemical active sites for the faradaic redox reaction process, leading to the improvement of the specific capacity. Despite that, all the samples showed significantly low storage capacity than the samples reported previously in Ref. [30]. At the same time, cyclic stability also suffered due to poor morphology.

In addition, it was also reported by Zhu *et al.* [33] that the increasing concentration of the precursor during the synthesis also increased the particle size and agglomeration. As a result, the particle size of  $\text{CuCo}_2\text{S}_4$ -water/EG (HC) was larger than the other two samples. This poor morphology of  $\text{CuCo}_2\text{S}_4$ -water/EG (HC) greatly reduced the electrochemical performance. The comparison of specific capacitance and cyclic retention among  $\text{CuCo}_2\text{S}_4$ -water,  $\text{CuCo}_2\text{S}_4$ -water/EG,  $\text{CuCo}_2\text{S}_4$ -water/EG (HC) were shown in Fig. 2.3. Therefore, it can be presumed that a proper solvent ratio is required to improve the performance of  $\text{CuCo}_2\text{S}_4$ .

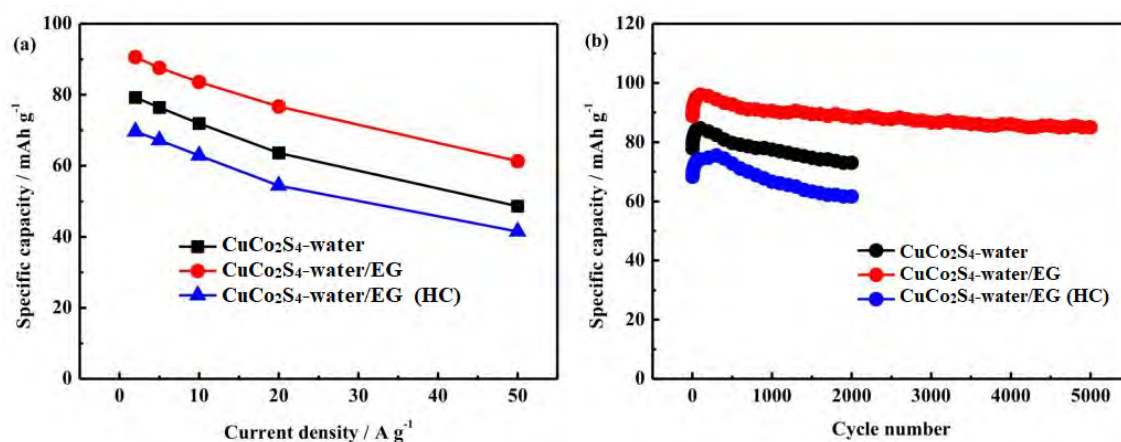


**Fig. 2.3** (a) The specific capacitance of the as-prepared three  $\text{CuCo}_2\text{S}_4$  electrodes (b) The cycling stability of the as-prepared three  $\text{CuCo}_2\text{S}_4$  electrodes at a current density of 3 A g<sup>-1</sup> [33].

In an investigation of 2019, Zequine *et al.* [34] reported that morphology greatly depends on volume ratio of solvent contents. It was found that the synthesis of  $\text{CuCo}_2\text{S}_4$  using 100 vol% water ( $\text{CuCo}_2\text{S}_4$  (Water)), 50/50 vol% water/ethanol ( $\text{CuCo}_2\text{S}_4$  (Water/Ethanol)) and 100 vol% ethanol ( $\text{CuCo}_2\text{S}_4$  (Ethanol)) resulted in different types of morphology as observed from the scanning electron microscopy images shown in Fig. 2.4. The investigation suggested that the dependence of the morphology on the solvent could be due to the difference in the polarity of the solvent. The effect of solvent polarity on the morphology of the synthesised materials was also observed in different materials [39–41]. In addition, it was reported that crystal size had also been affected by the solvent ratio and particle size of  $\text{CuCo}_2\text{S}_4$  (Water/Ethanol) had the smallest average crystal size. The effect of solvent over the charge storage capacity of the synthesised material was also reported, and  $\text{CuCo}_2\text{S}_4$  (Ethanol) showed a higher charge capacity and longer discharge capability than the other two materials. The mixed solvent showed the lowest electrochemical performance due to its poor morphology. So, a suitable solvent ratio is required to improve the morphology and hence electrochemical performance of  $\text{CuCo}_2\text{S}_4$ .

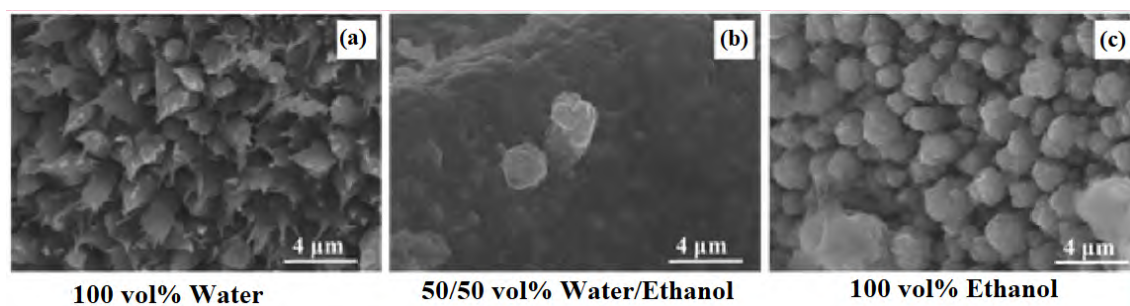


**Fig. 2.4** Scanning electron microscopy image of (a)  $\text{CuCo}_2\text{S}_4$  (Water) (b)  $\text{CuCo}_2\text{S}_4$  (Water/Ethanol) and (c)  $\text{CuCo}_2\text{S}_4$  (Ethanol) [34].

The crystallinity and morphology of  $\text{CuCo}_2\text{S}_4$  could also be affected by the reaction temperature. In 2018, Guo *et al.* [42] used a two-step hydrothermal approach to synthesis  $\text{CuCo}_2\text{S}_4$  at room temperature (CCS-RT), 100 °C (CCS-100), 150 °C (CCS-150), and 200 °C.  $\text{CuCo}_2\text{S}_4$  formed at room temperature had a typical amorphous structure, however, crystallinity of  $\text{CuCo}_2\text{S}_4$  had increased as hydrothermal temperature increased. All materials had a morphology of spherical clusters comprising multiple nanorods (Fig. 2.5 (a-f)), while sample CCS-200 has nanorods and nanoplates coexisted as it can be seen in Fig. 2.5 (g,h). When the reaction temperature was as high as 200 °C, the nanorods were self-assembled into nanoplates during the hydrothermal process. Furthermore, CCS-150 revealed just single nanorods with a noticeable porous shape due to volume expansion during the sulfidation process. According to the Arrhenius equation [43], the reaction temperature greatly influenced the reaction velocity. As a result, the reaction temperature influenced the crystallinity of  $\text{CuCo}_2\text{S}_4$ . Since the reaction temperature was not optimised, the resultant samples had poor morphology.

It was also reported by Guo *et al.* [42] that as the hydrothermal temperature rises, the specific capacitance (Fig. 2.6) rises as well, indicating that improving the crystallinity of  $\text{CuCo}_2\text{S}_4$  materials resulted in improved electrochemical performance. In general, electrode materials with a high crystallinity would have high conductivity and strong structural stability, which are two crucial characteristics of an ideal electrode material [44]. However, CCS-200 had an abnormally low specific capacitance, which could be due to self-assembly during the high-temperature hydrothermal process. Because nanorods had a larger surface area than nanoplates, microspheres made up of nanorods had more electrochemical active sites and a bigger electrode-electrolyte contact area [45,46]. Also the samples showed low cyclic stability due to poor morphology. Hence, a reaction temperature is required to be optimised to get a better morphology and electrochemical performance.

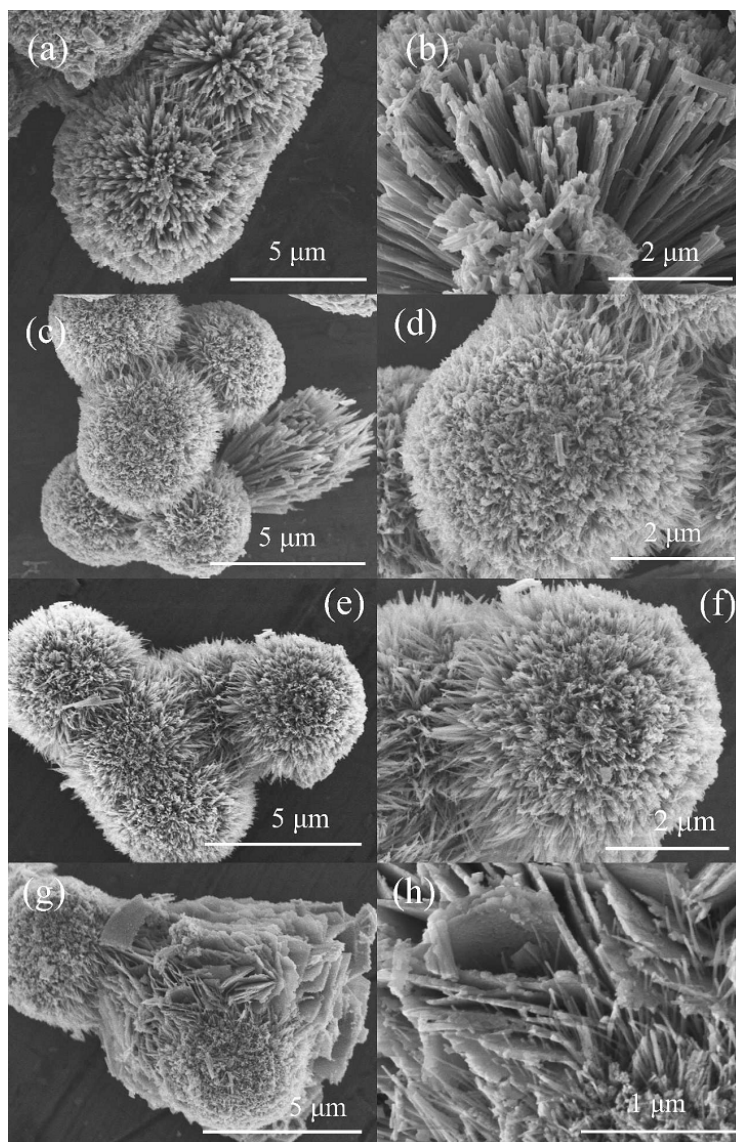


**Fig. 2.5** Scanning electron microscopy images of  $\text{CuCo}_2\text{S}_4$  materials under different magnifications, (a,b) CCS-RT, (c,d) CCS-100, (e,f) CCS-150, (g,h) CCS-200 [42].

Based on the above discussions, it was observed that without proper solvent, solvent ratio and optimising reaction temperature,  $\text{CuCo}_2\text{S}_4$  suffers from poor crystallinity and surface morphology resulting in poor electrochemical performance. It is well established [47–49] that  $\text{CuCo}_2\text{S}_4$ , synthesised in a hydrothermal method in a solvent (mixture of tert-butyl alcohol and deionized (DI) water) at the reaction temperature of 180 °C, showed better crystallinity, structural stability and morphology. In this investigation, these reaction condition was strictly followed to synthesis  $\text{CuCo}_2\text{S}_4$  and use the as-synthesized material for characterisation.

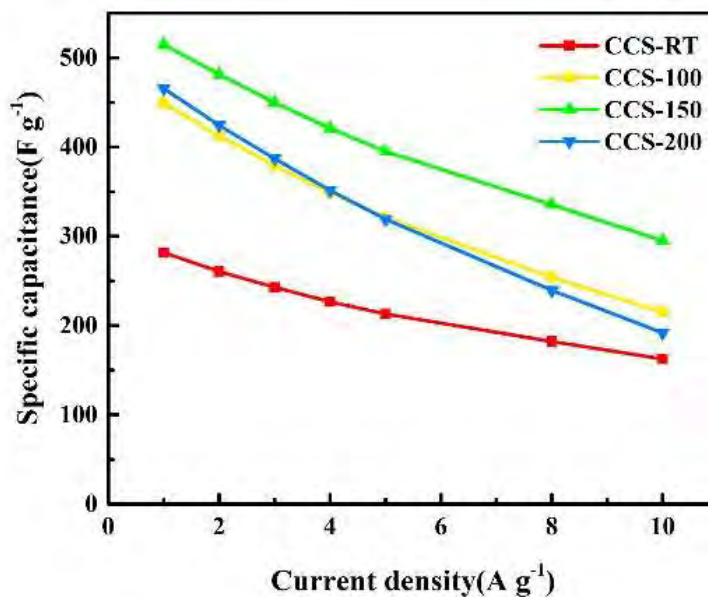


**Fig. 2.6** Temperature dependence of specific capacitance of  $\text{CuCo}_2\text{S}_4$  electrodes with increasing current density [42].

## 2.2 The Composite of $\text{CuCo}_2\text{S}_4$ Based Electrode

Despite various research to improve the electrochemical activity of  $\text{CuCo}_2\text{S}_4$ , low conductivity, accessible surface area, and permanent volume changes during charging-discharging (resulted in short cyclic stability) made it less suitable for application in energy storage devices. An effective way to improve the performance of  $\text{CuCo}_2\text{S}_4$  would be to synthesize a composite comprised of  $\text{CuCo}_2\text{S}_4$  and different types of material such as highly conductive carbon material (i.e., graphite, carbon nanotubes (CNTs), graphene, graphene quantum dots, etc.), energy storage material ( $\text{NiCo}_2\text{S}_4$ , Li-ion battery) and 2D transition metal dichalcogenides (i.e.,  $\text{MoS}_2$ ,  $\text{WS}_2$ ,  $\text{VS}_2$ ,  $\text{SnS}_2$ ).

In 2019, Tian *et al.* [50] reported that graphene could act as a skeleton for  $\text{CuCo}_2\text{S}_4$  and improve the electrochemical performance. In that investigation,  $\text{CuCo}_2\text{S}_4$ /graphene composite was successfully synthesized by anchoring  $\text{CuCo}_2\text{S}_4$  nanoparticles in graphene aerogel (GA). The graphene (Fig. 2.7 (a)) not only offered a conductive framework but also prevented  $\text{CuCo}_2\text{S}_4$  nanoparticles from aggregating, as can be seen in Fig. 2.7 (b and c). The synthesized  $\text{CuCo}_2\text{S}_4$  without GA, on the other hand, exhibited severe aggregation and was shown in the inset of Fig. 2.7 (c). Furthermore,  $\text{CuCo}_2\text{S}_4$ /GA had a greater specific surface area than  $\text{CuCo}_2\text{S}_4$  and the electrochemical activity increased as the crystallinity, shape, and specific surface area improved. According to the cyclic voltammetry and galvanostatic charge-discharge, the  $\text{CuCo}_2\text{S}_4$ /GA electrode had superior charge transfer kinetics due to



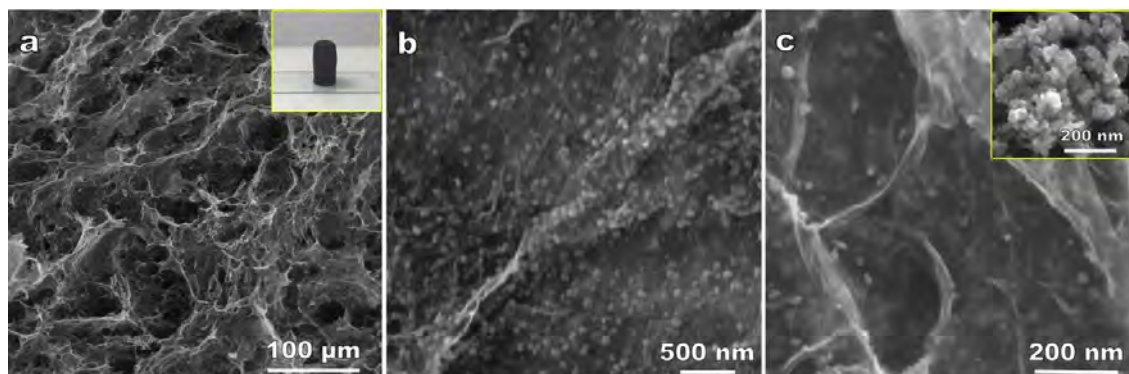


**Fig. 2.7** Scanning electron microscopy image of (a) GA, (b-c)  $\text{CuCo}_2\text{S}_4/\text{GA}$ , and in the inset of (c)  $\text{CuCo}_2\text{S}_4$  [50].

the synergistic effects of  $\text{CuCo}_2\text{S}_4$  and GA. Despite improving specific capacitance, the cyclic stability remained to be poor. So, it can be seen that a graphene like structure might help to improve the electrochemical performance of  $\text{CuCo}_2\text{S}_4$ .

Another type of composite that could improve the electrochemical activity would be the combination of  $\text{CuCo}_2\text{S}_4$  and other energy storage like electrode materials such as sulphides, oxides, transition metal hydroxide, etc. In 2019, Ma *et al.* [51] investigated  $\text{CuCo}_2\text{S}_4@\text{NiCo}_2\text{S}_4$  coreshell nanostructures on Ni foam synthesised via hydrothermal method. The resultant surface morphology was unique as a nanoneedle array was grown on Ni foam to form a microporous structure. The  $\text{CuCo}_2\text{S}_4$  nanoneedle array served as a substrate for the formation of  $\text{NiCo}_2\text{S}_4$  nanosheets, and the structure of the  $\text{CuCo}_2\text{S}_4$  nanoneedles was not changed even after the composite synthesis reaction was completed. As a result, the specific surface area and total pore volume increased, creating more active sites for redox reactions and ion transport [52]. It is evident that the synthesis process is complex and time consuming.

Tian *et al.* [51] also reported that in comparison to the  $\text{CuCo}_2\text{S}_4$  and  $\text{NiCo}_2\text{S}_4$  electrodes, the  $\text{CuCo}_2\text{S}_4@\text{NiCo}_2\text{S}_4$  composite electrode exhibited higher current density (Fig. 2.8 (a)), improved charging-discharging capability (Fig. 2.8 (b)), high ion transfer rate (Fig. 2.8 (c)), higher specific capacitance (Fig. 2.8 (d)), improved stability (Fig. 2.8 (e)), and capacity retention (Fig. 2.8 (f)). For the improvement in electrochemical performance, it had been suggested that the following factors were responsible: the growth of composite material directly on the Ni foam, the synergistic effect of  $\text{NiCo}_2\text{S}_4$  nanosheets and  $\text{CuCo}_2\text{S}_4$  nanoneedle arrays, the high electrical conductivity of the  $\text{CuCo}_2\text{S}_4$  nanoneedles arrays, and the improved diffusion path of  $\text{CuCo}_2\text{S}_4@\text{NiCo}_2\text{S}_4$  structure. As a result, the composite presented excellent electrochemical performances owing to the synergistic effect. So it can be

concluded that the electrochemical performance of a composite can be improved when the constituent are well connected with each other. However, a facile and energy efficient method is expected for the synthesis of the materials.

Xu *et al.* [53], in an investigation of 2018, controllably synthesised 3D hierarchical porous  $\text{CuCo}_2\text{S}_4/\text{CuCo}_2\text{O}_4$  heterostructures via anion exchange method and the mesoporous structure was also tuned via changing the amount of sulphide agent (TAA) during the anion exchange process. Six samples of  $\text{CuCo}_2\text{S}_4/\text{CuCo}_2\text{O}_{4-x}$  ( $x=0, 1, 2, 3, 4, 5$ ) heterostructures were prepared with increasing feeding TAA amount of 0, 0.25, 0.5, 0.75, 1 and 1.5 mmol, respectively. The morphological study revealed that during the anion exchange process, the surface of the  $\text{CuCo}_2\text{O}_4$  flowers became rough and formed a porous network consisting of the interconnected hetero- $\text{CuCo}_2\text{S}_4/\text{CuCo}_2\text{O}_4$ . Even with the different S concentrations, all the composites had a similar flower shape structure (Fig. 2.9 (a-d)).

The electrochemical performance also increased for the composites as reported by Xu *et al.* [53]. Compared with the  $\text{CuCo}_2\text{S}_4/\text{CuCo}_2\text{O}_4$  heterostructures electrodes,

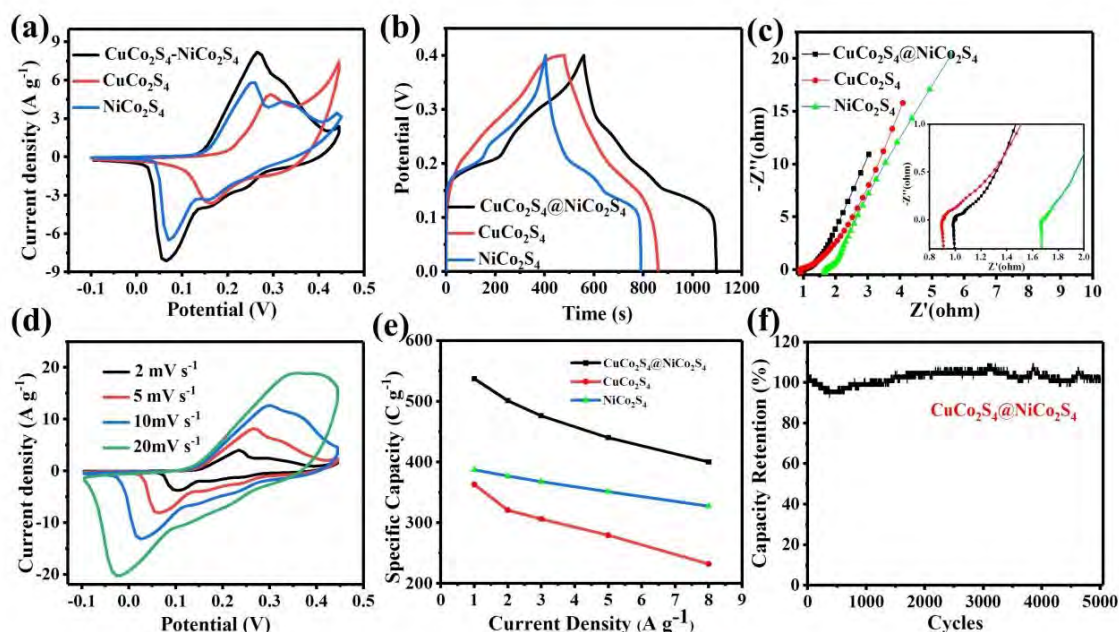


**Fig. 2.8** (a) Cyclic voltammetry curves at scan rate of  $5 \text{ mVs}^{-1}$ ; (b) Galvanostatic charge-discharge curves at a current density of  $1.0 \text{ Ag}^{-1}$ ; (c) Nyquist plots of  $\text{CuCo}_2\text{S}_4@\text{NiCo}_2\text{S}_4$ ,  $\text{CuCo}_2\text{S}_4$ , and  $\text{NiCo}_2\text{S}_4$  electrodes in 3 M KOH; (d) Cyclic voltammetry curves of the  $\text{CuCo}_2\text{S}_4@\text{NiCo}_2\text{S}_4$  composite at different scan rates in 3 M KOH; (e) The specific capacity of  $\text{CuCo}_2\text{S}_4$  nanoneedles arrays,  $\text{NiCo}_2\text{S}_4$  nanosheet array and composite structure at various current densities, respectively; (f) The cyclic performance of  $\text{CuCo}_2\text{S}_4@\text{NiCo}_2\text{S}_4$  composite structure at the current density of  $8 \text{ Ag}^{-1}$  for 5000 continuous cycles [51].

pure  $\text{CuCo}_2\text{O}_4$  based electrode showed a lower specific capacity, and with the increasing S concentration, the specific capacities increased accordingly. The superior electrochemical performances of  $\text{CuCo}_2\text{S}_4/\text{CuCo}_2\text{O}_4$  heterostructures were attributed to the large surface area and increased conductivity, which endowed a rich contact interface of electrode/electrolyte (Fig. 2.10 (a-c)). However, the specific capacitance also decreased after a certain concentration of S. It was inferred that the internal structure collapsed at a high concentration of S. The inner pore volume and surface area decreased, leading to inferior electrochemical performance. Similar activity was also observed in charging-discharging (Fig. 2.10 (d)), ion transfer (Fig. 2.10(e)), and cyclic stability (Fig. 2.10 (f)). This could be due to the lack of strong interconnection between  $\text{CuCo}_2\text{S}_4$  and  $\text{CuCo}_2\text{O}_4$ . As a result it is necessary to create a strong connection between the materials during the synthesis of this composite.

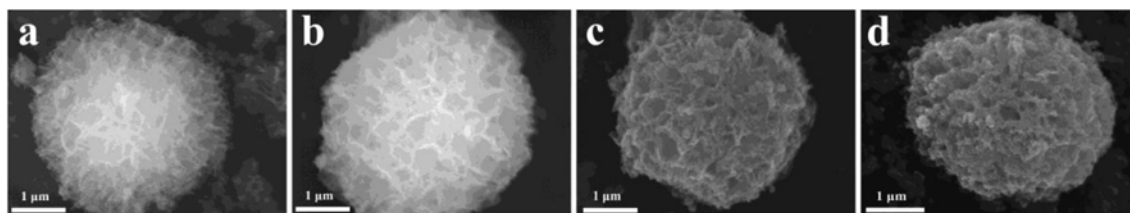


**Fig. 2.9** Morphological evolution of the 3D flower-like  $\text{CuCo}_2\text{S}_4/\text{CuCo}_2\text{O}_4$  with increasing feeding amount of TAA. (a–d) Scanning electron microscopy images of the mesoporous  $\text{CuCo}_2\text{S}_4/\text{CuCo}_2\text{O}_4$ -0,  $\text{CuCo}_2\text{S}_4/\text{CuCo}_2\text{O}_4$ -1,  $\text{CuCo}_2\text{S}_4/\text{CuCo}_2\text{O}_4$ -4 and  $\text{CuCo}_2\text{S}_4/\text{CuCo}_2\text{O}_4$ , respectively [53].

Based on the above discussion, it could be concluded that electrochemical performance of  $\text{CuCo}_2\text{S}_4$  can be significantly improve by incorporating with other materials. To enhance the electrochemical performance of  $\text{CuCo}_2\text{S}_4$  electrode, incorporating two dimensional (2D) nanomaterials having high specific area as a supporting matrix appears to be an effective design strategy [5, 10, 12, 19]. To date, 2D transition metal dichalcogenides such as  $\text{MoS}_2$  [21],  $\text{SnS}_2$  [54],  $\text{WS}_2$  [55],  $\text{VS}_2$  [56] have been reported as promising redox-active materials for storing charges via double layer ion-adsorption [57]. In particular, 2D layered  $\text{MoS}_2$  has demonstrated promising electrochemical performance because of its highly versatile electronic structure, availability of various possible oxidation states, large in-plane electronic conductivity, and high surface area [20–22]. Since  $\text{MoS}_2$  contained many advantages in electrochemical studies like large surface area, which favoured the double-layer capacitance, and the Mo edges were active for redox reactions, which provided additional capacitance through pseudocapacitive reaction. Therefore, in this investigation  $\text{MoS}_2$  was incorporated with  $\text{CuCo}_2\text{S}_4$  to explore the structural, morphological and electrochemical properties.

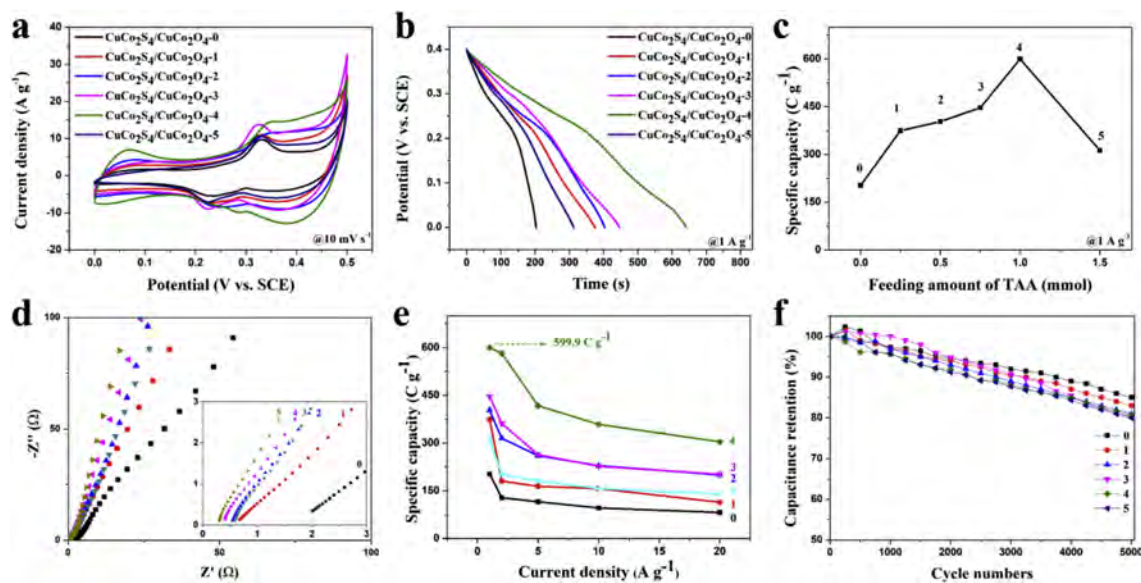


**Fig. 2.10** Electrochemical performances of the samples for supercapacitors. (a) Cyclic voltammograms at a scan rate of 10 mV s<sup>-1</sup> for all the samples. (b) Galvanostatic charge-discharge curves at a current density of 1 A g<sup>-1</sup> for all the samples. (c) Specific capacity versus feeding amount of TAA at 1 A g<sup>-1</sup>. (d) electrochemical impedance spectroscopy spectra of the 3D flower-like CuCo<sub>2</sub>S<sub>4</sub>/CuCo<sub>2</sub>O<sub>4</sub> electrodes. (e) The specific capacities of the 3D flower-like CuCo<sub>2</sub>S<sub>4</sub>/CuCo<sub>2</sub>O<sub>4</sub> electrodes at different current density. (f) Cycling performance at a current density of 20 A g<sup>-1</sup> [53].

## 2.3 Fundamental of Electrochemistry in Energy Storage

Electrochemical energy storage system basically stores electric energy in chemical form. This storage technique is highly efficient because both electrical and chemical energy share electron as the same carrier. This common point allows to limit the losses due to the conversion from one form to another. A typical electrochemical energy storage system is consisted of an anode, a cathode, a separator, and an electrolyte. During charging-discharging, an external voltage is applied across the electrodes and electrochemical reactions occur at the electrodes generating electrons that flow through an external circuit. Typical electrochemical energy storage systems include batteries and supercapacitors, both of which store electricity in electrochemical processes.

### 2.3.1 Supercapacitor

Supercapacitors are energy storage devices with high energy density, power density, and cycle life. It is also known as electrochemical capacitors or ultracapacitors. Supercapacitors can charge and discharge quickly, resulting in a high-power delivery in a short period of time, owing to the use of materials with a large surface area and high porosity and superior conductive substances. Because of the short charge-

discharge time, which results in high power density, they are increasingly used in portable gadgets, automobiles, buses, trains, cranes, and elevators [58–60].

### 2.3.2 Mechanism of supercapacitor

Like a dielectric capacitor, the charge does not accumulate on two conductors separated by a dielectric in an electrical double layer capacitor. Instead, the charge builds in the electric double layer at the interface between the surface of a conductor and an electrolyte solution. When charged, in the electrolytes, the negative ions diffuse to the positive electrode and the positive ions diffuse to the negative electrodes. Because the double layer capacitor does not involve chemical reactions, supercapacitors have a prolonged charge and discharge life cycle. Apart from the capacitance contribution from charge separation in the double layer, capacitance associated with reactions on the electrode's surface is also significant. During these processes, electrons are transferred across the double layer, resulting in oxidation state changes. Thus, the capacitance from the faradaic process is referred to as pseudo-capacitance. The next paragraphs go through the essential difference among double-layer capacitor, pseudo-capacitor and hybrid capacitor in detail.

#### 2.3.2.1 Electrochemical double-layer capacitor

In the case of EDLC, charges are stored as ions adsorbed at electrode/electrolyte interfaces via electro-static interactions as can be seen in Fig. 2.11. If the electrode is negatively charged (i.e., charged with electrons), the electrostatic attraction between the negative charged electrons near the electrode surface and the cation in the electrolyte attracts them. A layer, called inner Helmholtz layer (IHL), is formed when the first anchoring cations align with each other and create a compact and ordered layer. The second layer, termed the outer Helmholtz layer (OHL), is made up of counter ions (in this case, anions) that are drawn to the ions in the IHL. Anions pack more loosely and disordered in the OHL than cations do in the IHL. Because of the dielectric nature of the solvent and solvation sheaths surrounding the counter ions, the electrostatic attraction force imposed by the counter ions is diminished. The IHL and the OHL together are termed “electrical double layer”. Electrons are stored at the electrode-electrolyte contact in EDLs. Increasing the ion-accessible surface area of an electrode can generally increase the magnitude of electrical double layer capacitance.

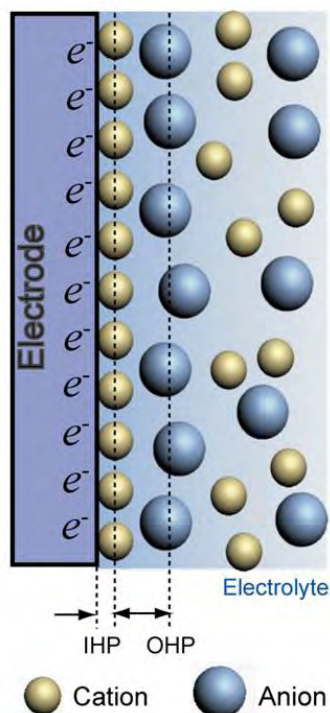


**Fig. 2.11** Schematic of electrochemical double-layer capacitor structure.

### 2.3.2.2 Pseudo-capacitor

The basis of pseudo-capacitor is faradaic reaction, and it differs from the classical electrostatic capacitance seen in the double layer. The pseudo-capacitive reactions are usually considered to be divided into three groups: [61] under-potential deposition, near-surface redox reaction and fast ion insertion and extrusion that trigger no phase transitions. Electrodeposition of a species at a potential lower than its predicted reduction potential is known as under-potential deposition (Fig. 2.12 (a)). The deposition of lead (Pb) thin films onto gold (Au) substrates is a good example [61]. The most prevalent type of pseudo-capacitive reaction is the near-surface redox reaction ((Fig. 2.12 (b)). On the surface of some pseudo-capacitive materials, redox chemical reactions store electrons by changing the valence state of the active site(s). In this situation, electrons are trapped in the near-surface region of the electrode as lower valence states of pseudo-capacitive sites. The protonation and deprotonation of ruthenium dioxide ( $\text{RuO}_2$ ) is a good example. A form of pseudo-capacitive process known as fast ion insertion-disinsertion was demonstrated in Fig. 2.12(c). It is similar to how lithium-ion batteries use ion intercalation and deintercalation operations. The distinction between a battery-type reaction and a capacitive reaction is whether the process produces a phase transition(s). The phase of related electrode materials should not be altered by pseudo-capacitive processes. Guest ions must be hosted in layered structures in electrode materials that exhibit this activity.

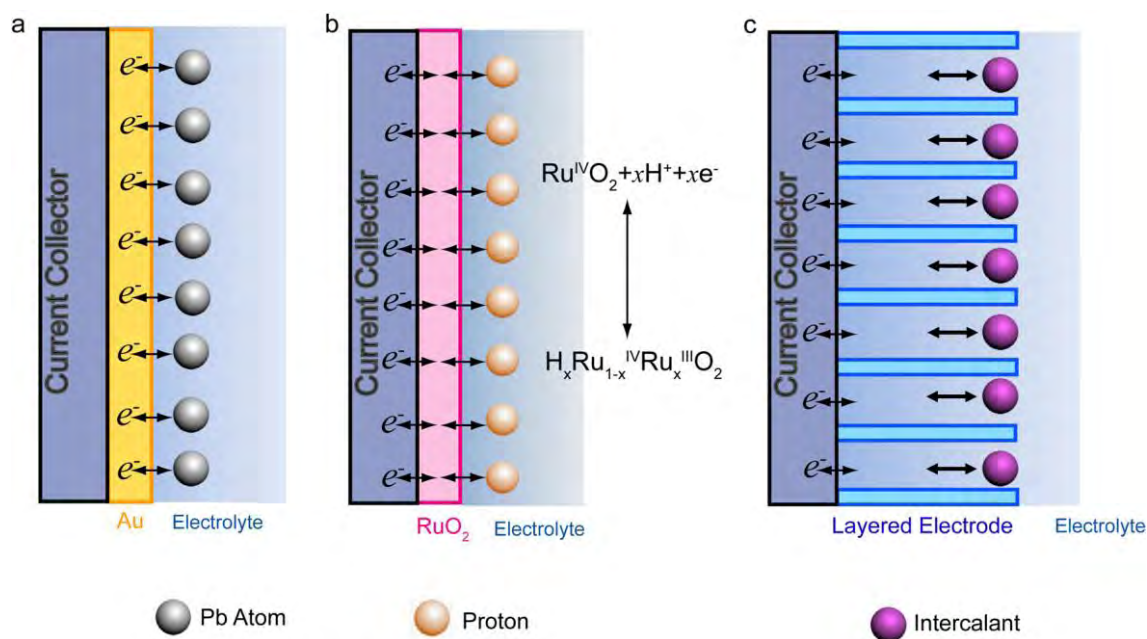


**Fig. 2.12** Three typical types of pseudo-capacitive reactions. (a) Under-potential deposition: electro-deposition of Pb thin films onto Au substrate. (b) Near-surface redox reactions: protonation and de-protonation of RuO<sub>2</sub> in aprotic electrolytes. (c) Fast ion insertion-deinsertion.

### 2.3.2.3 Hybrid capacitor

The hybrid capacitor, which is a combination of EDLC and pseudocapacitor, provides better performance than the individual. Energy is stored in EDLC using intrinsic shell area and atomic charge partition length [62]. In a pseudocapacitor, energy storage is achieved through quick reproducible redox reactions between active electrode material and an electrolyte solution [63]. The energy storage mechanism of hybrid capacitors is made up of the combination of these two storage techniques. Half of the hybrid capacitor functions as an EDLC, while the other half functions as a pseudocapacitor. In comparison to the standard EDLC and pseudocapacitor, hybrid capacitors have higher energy and power densities. This promotes their application in energy efficient systems over other energy storage technologies [64].

## CHAPTER 3

### MATERIALS AND METHODS

In this chapter, the preparation of  $\text{CuCo}_2\text{S}_4\text{-MoS}_2$  nanocomposite using a facile hydrothermal technique is presented. After that, various techniques, which were used to investigate the structural and morphological properties of  $\text{CuCo}_2\text{S}_4\text{-MoS}_2$  are described. Finally, to illustrate the electrochemical performance of  $\text{CuCo}_2\text{S}_4\text{-MoS}_2$ , different methods and setups that were used for this investigation are discussed.

#### 3.1 Sample Preparation

The synthesis route for the  $\text{CuCo}_2\text{S}_4\text{-MoS}_2$  nanocomposite is presented in Fig. 3.1.

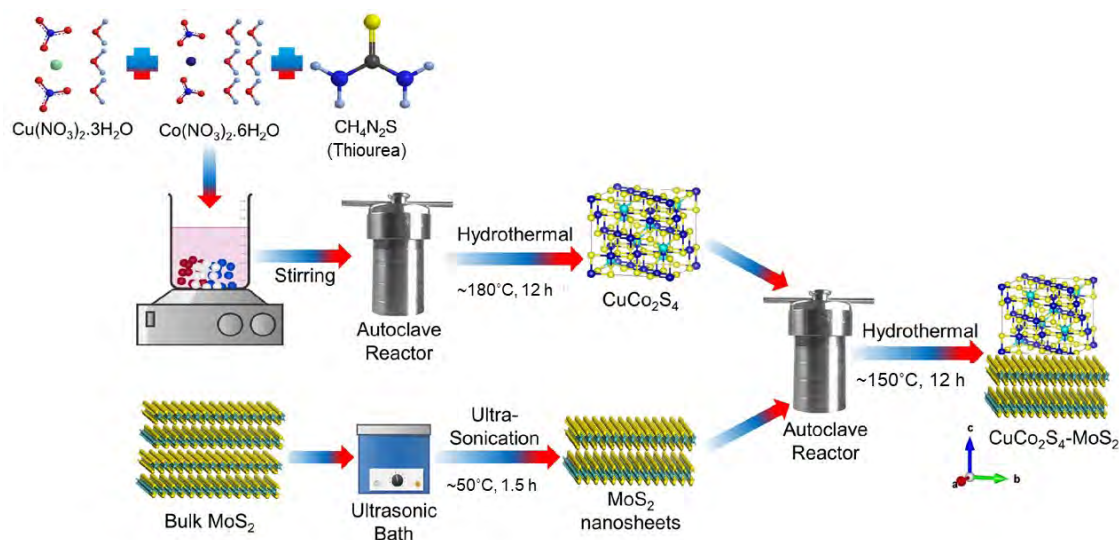


**Fig. 3.1** Schematics of the synthesis steps of  $\text{CuCo}_2\text{S}_4\text{-MoS}_2$  nanocomposite using a hydrothermal technique.

##### 3.1.1 Synthesis of nanostructured $\text{CuCo}_2\text{S}_4$

Nanostructured  $\text{CuCo}_2\text{S}_4$  was synthesised by adopting a hydrothermal technique [65]. Initially, 1 mmol of  $\text{Cu}(\text{NO}_3)_2 \cdot 3\text{H}_2\text{O}$ , 2 mmol of  $\text{Co}(\text{NO}_3)_2 \cdot 6\text{H}_2\text{O}$ , and 9 mmol of  $\text{CH}_4\text{N}_2\text{S}$  were dissolved in 50 mL 1:1 (v/v) solution of tert-butyl alcohol and deionized (DI) water. The resultant mixture was then magnetically stirred for 1 hour to get a homogeneous solution. Afterward,  $\text{NH}_4\text{OH}$  was added drop wise into the solution to obtain a pH of 10 and was stirred for another 1 hour. Further, the



solution was moved to a teflon-lined stainless-steel autoclave. It was heated at a temperature of 180 °C for 12 hours and then was naturally cooled down to room temperature (RT). The resultant product was washed with ethanol and DI water for several times to remove any residual solvent. Finally, nanostructured  $\text{CuCo}_2\text{S}_4$  was obtained by drying the product at 100 °C in vacuum.

### 3.1.2 Synthesis of $\text{CuCo}_2\text{S}_4$ - $\text{MoS}_2$ nanocomposite

To synthesise the  $\text{CuCo}_2\text{S}_4$ - $\text{MoS}_2$  nanocomposite, at first, raw  $\text{MoS}_2$  powder was cleaned via ultrasonication for 15 minutes. Then, a facile hydrothermal technique was adopted to incorporate the ultrasonicated  $\text{MoS}_2$  with previously synthesised nanostructured  $\text{CuCo}_2\text{S}_4$  [66]. Initially, 200 mg of  $\text{CuCo}_2\text{S}_4$  and 20 mg of  $\text{MoS}_2$  (10% w/w) were dissolved in 50 mL DI water and stirred for 3 hours. Afterward, the solution was inserted in the autoclave which was heated at 150 °C for 12 hours and then, naturally cooled down to RT [66]. Next, centrifugation was performed (Hettich Universal 320), followed by rinsing with DI water and ethanol. Finally, the purified solution was dried at 100 °C for 12 hours in vacuum to obtain the desired  $\text{CuCo}_2\text{S}_4$ - $\text{MoS}_2$  nanocomposite.

## 3.2 Structural Characterisation Techniques

In the following subsections, the techniques that were adopted to determine the structural properties of  $\text{CuCo}_2\text{S}_4$ - $\text{MoS}_2$  nanocomposite are described.

### 3.2.1 X-ray diffraction

The structural properties of  $\text{CuCo}_2\text{S}_4$  and  $\text{CuCo}_2\text{S}_4$ - $\text{MoS}_2$  were first investigated via the X-ray diffraction (XRD) analysis. XRD is an analytical technique that may be used to determine the phase of a crystalline material as well as unit cell dimensions [67]. The constructive interference of monochromatic X-rays with a crystalline substance is the basis of XRD. A cathode-ray tube produces the X-rays, filtered to produce monochromatic radiation, collimated to concentrate the beam, and aimed onto the sample. As X-rays are waves of electromagnetic energy, and crystals are regular arrays of atoms, X-rays are scattered by atoms, largely through their electrons. When an X-ray collides with an electron, secondary spherical waves emerge from the electron. This phenomenon is known as elastic scattering, and the electron is known as the scatterer. The scatterers in a regular array produce a regular array of spherical waves. Although destructive interference cancels out these waves in most directions, Bragg's law determines the selected direction in which constructive interference generate.

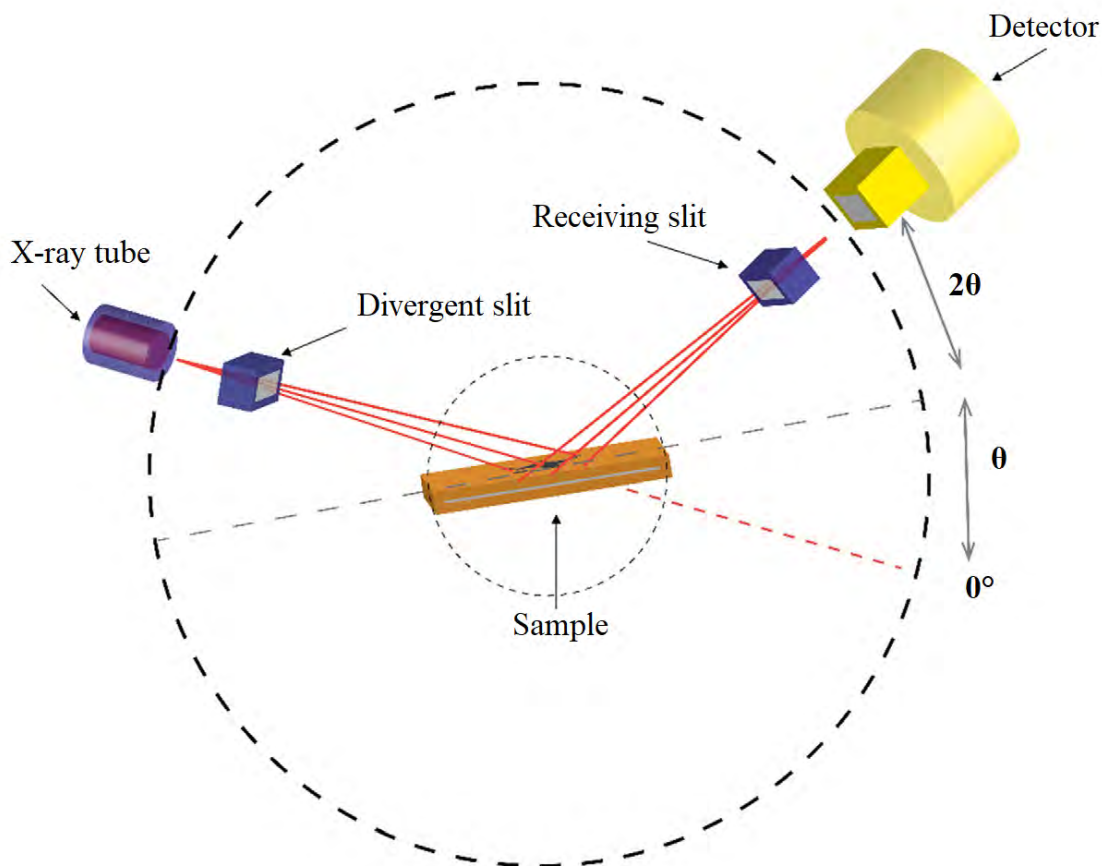


**Fig. 3.2** Schematic illustration of X-ray diffractometer instrument.

In a crystalline material, this rule relates the wavelength of electromagnetic radiation to the diffraction angle and lattice spacing. Each scatterer re-radiates a portion of its intensity as a spherical wave because of the incoming beam (seen in Fig. 3.2, originating from the upper left). These spherical waves will only produce constructive interference in directions where path-length difference  $2d\sin\theta$  equals an integer,  $n$ , multiple of the wavelength if scatterers are arranged symmetrically with a separation,  $d$ . In that situation, a reflection appears in the diffraction pattern because an angle of  $2\theta$  deflects a portion of the incoming beam. The detected, processed, and counted diffracted X-rays are next analysed. Due to the random orientation of the powdered material, scanning the sample through a range of  $2\theta$  angles should yield all potential lattice diffraction directions. Because each crystal has its own set of  $d$ -spacings, converting the diffraction peaks to  $d$ -spacings enables XRD to material identification. The crystal structures of the as-prepared  $\text{CuCo}_2\text{S}_4$  and  $\text{CuCo}_2\text{S}_4\text{-MoS}_2$  were investigated by obtaining their powder XRD patterns using a diffractometer (Rigaku SmartLab) with a Cu X-ray source (wavelength,  $\lambda$ :  $\text{K}\alpha_1 = 1.54059 \text{ \AA}$  and  $\text{K}\alpha_2 = 1.54180 \text{ \AA}$ ).

### 3.2.2 Rietveld refinement

To find out crystalline structure, phase, and unit cell parameter, experimentally acquired XRD data of  $\text{CuCo}_2\text{S}_4$  and  $\text{CuCo}_2\text{S}_4\text{-MoS}_2$  were extensively analysed via Rietveld refinement method. Hugo Rietveld [68, 69] invented this technique for characterising crystalline materials. Powder sample's diffraction with neutrons and X-rays produces a pattern with reflections (intensity peaks) at certain locations. Many elements of the material's structure can be deduced from the height, width, and position of the peaks. In Rietveld refinement, model parameters represent distinct profile elements and can be split into three groups. First, the set of characteristics that govern crystal symmetry (space group), unit cell parameters, atomic locations, site occupancy, and displacements. The background parameters are the second set of parameters. Background sources include inelastic or incoherent scattering from the sample and its environment, electronic noise, and other undesired sources. Because the background scattering changes slowly with scattering angle, the Bragg peaks can generally be distinguished from the background. The third set of parameters describes the forms of Bragg peaks.

The Rietveld refinement is guided numerically using agreement indices, or R values [70]. The quantity minimized in the refinement is the residual  $S_y$

$$S_y = \sum_i W_i [y_i(\text{obs}) - y_i(\text{cal})]^2 \quad (3.1)$$

Where  $y_i(\text{obs})$  is the observed intensity at step  $i$ ,  $y_i(\text{cal})$  is the calculated intensity and  $w_i$  is the weight. This quantity is included in the weighted-profile  $R$  value,  $R_{wp}$ , which is defined as,

$$R_{wp} = \left\{ \frac{w_i [y_i(\text{obs}) - y_i(\text{cal})]^2}{w_i [y_i(\text{obs})]^2} \right\}^{\frac{1}{2}} \quad (3.2)$$

Ideally,  $R_{wp}$  should approach the statistically expected  $R$  value,  $R_{exp}$ ,

$$R_{exp} = \left[ \frac{N - P}{\sum_i^N w_i y_i(\text{obs})^2} \right]^{\frac{1}{2}} \quad (3.3)$$

Where  $N$  is the number of observations and  $P$  is the number of parameters. The goodness of fit is,

$$\chi^2 = \left( \frac{R_{wp}}{R_{exp}} \right)^2 \quad (3.4)$$

In this investigation, the crystallographic parameters and phase of  $\text{CuCo}_2\text{S}_4$  and  $\text{CuCo}_2\text{S}_4\text{-MoS}_2$  were analysed quantitatively by Rietveld refinement of powder XRD

patterns using the X'Pert High- Score Plus software package.

### 3.3 Morphological and Elemental Composition Analyses Techniques

The techniques that were used to study surface morphology, crystallinity, elemental and chemical composition of  $\text{CuCo}_2\text{S}_4$  and  $\text{CuCo}_2\text{S}_4\text{-MoS}_2$  are discussed in the following subsections.

#### 3.3.1 Field Emission Scanning Electron Microscopy

As discussed in chapter 2, surface morphology plays an important role in regulating electrochemical performance. To investigate the surface morphology of  $\text{CuCo}_2\text{S}_4$  and  $\text{CuCo}_2\text{S}_4\text{-MoS}_2$  Field Emission Scanning Electron Microscopy (FESEM) technique was used. FESEM analysis uses a focused electron beam to obtain complex, high magnification images of a sample's surface topography. FESEM images have a broad depth of field due to the narrow electron beam, giving them a three-dimensional appearance essential for studying sample surface structure [71]. The signals produced by a FESEM come from the electron beam's interaction with atoms at varying depths within the sample. The schematic of the FESEM is shown in Fig. 3.3.

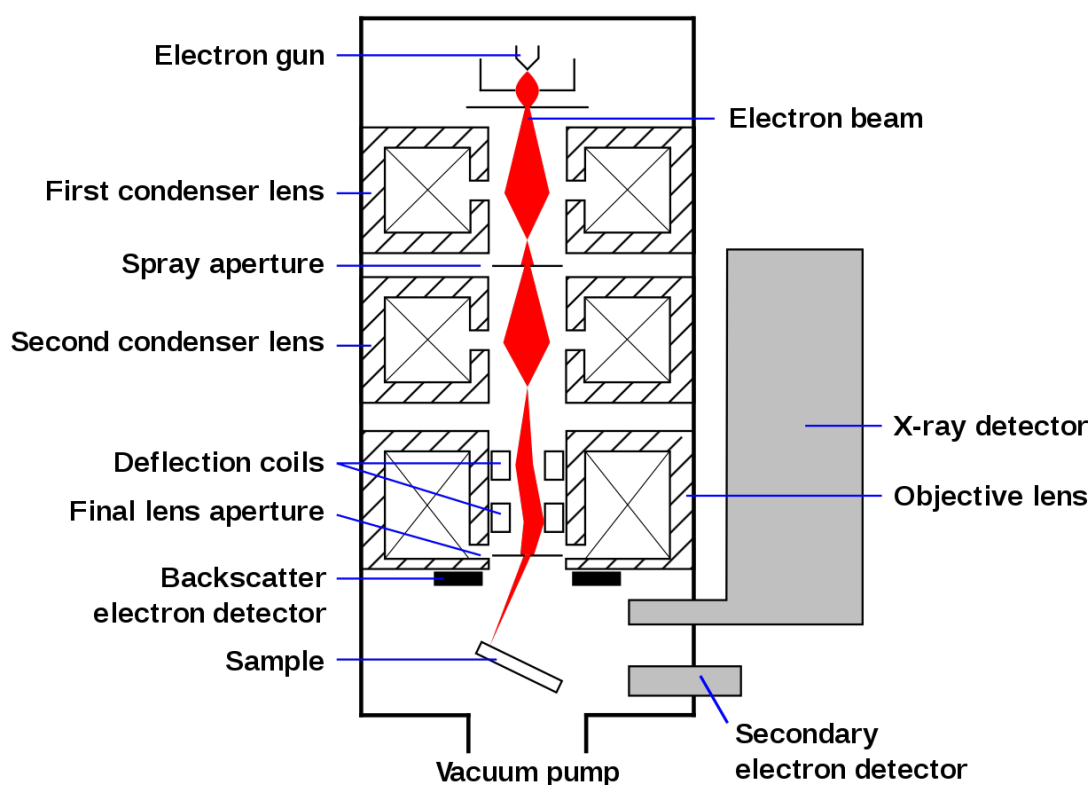


**Fig. 3.3** Schematic diagram of a Field Emission Scanning Electron Microscope.

An electron beam thermionically emits from an electron gun in a FESEM. One or two condenser lenses focus the electron beam to a point. The beam passes via scanning coils or deflector plates in the electron column, often in the last lens, deflecting the beam in the  $x$  and  $y$  axes. The interaction volume is a teardrop-shaped volume of the specimen that extends into the surface. The interaction volume depends on the electron's landing energy, the specimen's atomic number, and the density of the sample. The energy exchange between the electron beam and the sample results in high-energy electron reflection, secondary electron emission, and electromagnetic radiation emission, all of which can be detected by specialised detectors. Secondary electrons have low energies that limit their mean free route in solids. As a result, secondary electrons can only escape from the surface of a sample. The secondary electron signal is extremely localised at the initial electron impact point, allowing for 1 nm resolution imaging of the sample surface. A beam of electrons, called Back-Scattered Electrons (BSE), is reflected from a material using elastic scattering. Because BSEs have larger energy than secondary electrons, they come from deeper regions inside the object, reducing imaging resolution. Because the intensity of the BSE signal is directly associated with the specimen's atomic number ( $Z$ ), BSE is frequently utilised in analytical FESEM and X-ray spectra. BSE images can reveal the distribution but not the identity of components in a sample. When an electron beam removes an inner shell electron from a sample, a higher-energy electron fills the shell and releases energy. Energy-dispersive X-ray (EDX) spectroscopy can measure the energy or wavelength of these specific X-rays to identify and map the number of elements in the sample. The generated image is a distribution map of the strength of the signal emitted from the scanned area of the specimen. Various electronic amplifiers increase the signals, which appear as brightness differences on a computer monitor. Hence, XRD and EDX pattern is obtained. In this investigation, surface morphology and elemental composition of  $\text{CuCo}_2\text{S}_4$  and  $\text{CuCo}_2\text{S}_4\text{-MoS}_2$  were investigated using a field emission scanning electron microscope (JEOL, JSM-7600F, Japan). At first the powder sample was taken in a copper tape which is actually consists of three layers, the lower one is a copper layer, the middle one is a carbon tape and the upper one is the copper tape where the sample was adhered. Then the sample was coated with platinum by ion sputtering method in auto fine coater for about 40 seconds. A 10 nm layer of platinum is coated upon the sample. Then the copper tape is mounted on a holder in the specimen chamber and inserted in the FESEM.

### 3.3.2 Transmission Electron Microscopy

To further investigate the morphology, crystallinity of  $\text{CuCo}_2\text{S}_4$  and  $\text{CuCo}_2\text{S}_4\text{-MoS}_2$ , Transmission Electron Microscopy (TEM) analysis was carried out. In TEM, a beam of electrons is passed through a material, and their interaction produces an image. Because electrons have a shorter de Broglie wavelength, TEM can produce an image at a far higher resolution than light microscopes. This allows the device to capture extremely fine detail, even down to a single atom column. The two primary operating modes of a TEM, imaging and diffraction modes, are shown in Fig. 3.4. The specimen is illuminated by an electron beam shaped by condenser lenses and condenser aperture in both cases. After interaction with the sample, the specimen has two sorts of electrons: unscattered and scattered. The objective aperture is in the back focal plane (where diffraction spots are formed). The transmitted electrons pass through the objective aperture while all others are blocked, resulting in a bright-field image, and a dark field image is created when a diffracted beam signal is allowed. Intermediate and projector lenses magnify and project the selected signal

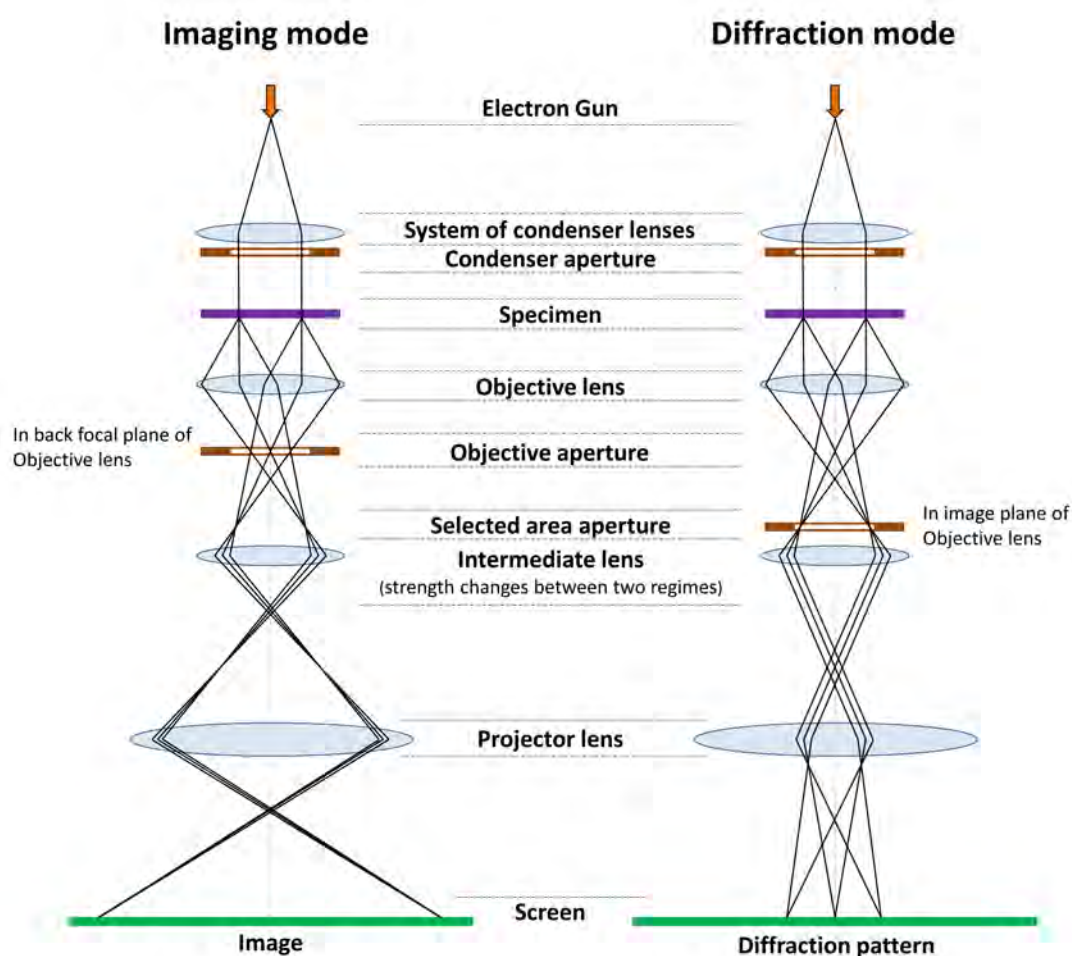


Fig. 3.4 Schematic view of imaging and diffraction modes in TEM.

on a screen, and a sample image is obtained. In diffraction mode, an aperture can be utilised to narrow down the specimen region from which the signal will be presented. It is projected on a screen by altering the current to the intermediate lens. It can be used to determine crystal orientation. High-resolution Transmission Electron Microscopy (HRTEM) is a technique that uses specialised transmission electron microscopes to image sample's atomic structure. Images develop when a field emission source interacts with a uniformly sized specimen [72]. In a Selected Area Electron Diffraction (SAED), a diffraction pattern can be created by placing the magnetic lenses' rear focal plane on the imaging equipment rather than the imaging plane. A single crystal picture is a pattern of dots, while a polycrystalline or amorphous solid material image is a series of rings. In the case of single crystals, the diffraction pattern is determined by the specimen's orientation and structure. Since the resolution of a TEM is better than that of a FESEM, in this investigation, TEM (Talos F200X, Thermo fisher scientific, USA) imaging was carried out to investigate the crystals as well as to check the crystallinity of  $\text{CuCo}_2\text{S}_4$  and  $\text{CuCo}_2\text{S}_4\text{-MoS}_2$  by analysing SAED pattern and HRTEM imaging.

### 3.3.3 Fourier Transform Infrared Spectroscopy

In this investigation, Fourier Transform Infrared Spectroscopy (FTIR) (Shimadzu, IRSpirit-T) analysis was carried out to find out the chemical structure of  $\text{CuCo}_2\text{S}_4$  and  $\text{CuCo}_2\text{S}_4\text{-MoS}_2$ . Using Fourier transformation, the method of collecting and converting data from an interference pattern (due to the presence of chemical bonds in a material) to a spectrum is referred to as FTIR [73]. FTIR is the most effective method for identifying compounds. It can be used to analyse solids, liquids, and gases and quantify some components of an unknown mixture. It is a useful method for recognising different chemical bonds in a molecule by a molecular fingerprint in the form of an infrared absorption spectrum. The chemical bond determines the wavelength of light it absorbs. Also, depending on the elements and the type of bond, molecular bonds vibrate at different frequencies.

The FTIR spectrometry technique was created to address the limitations of dispersive instruments. The slow scanning process approach for detecting all infrared frequencies concurrently rather than individually was the main challenge of those instruments. Fig. 3.5 shows a schematic diagram of an FTIR. Light is directed to a beam splitter as shown in Fig. 3.5. In an ideal situation, half of the light is reflected towards the fixed mirror, and half is transmitted towards the moving mirror. Light is reflected in the beam splitter from the two mirrors, and a portion of the original light enters the sample compartment and is concentrated on the sample. The light is

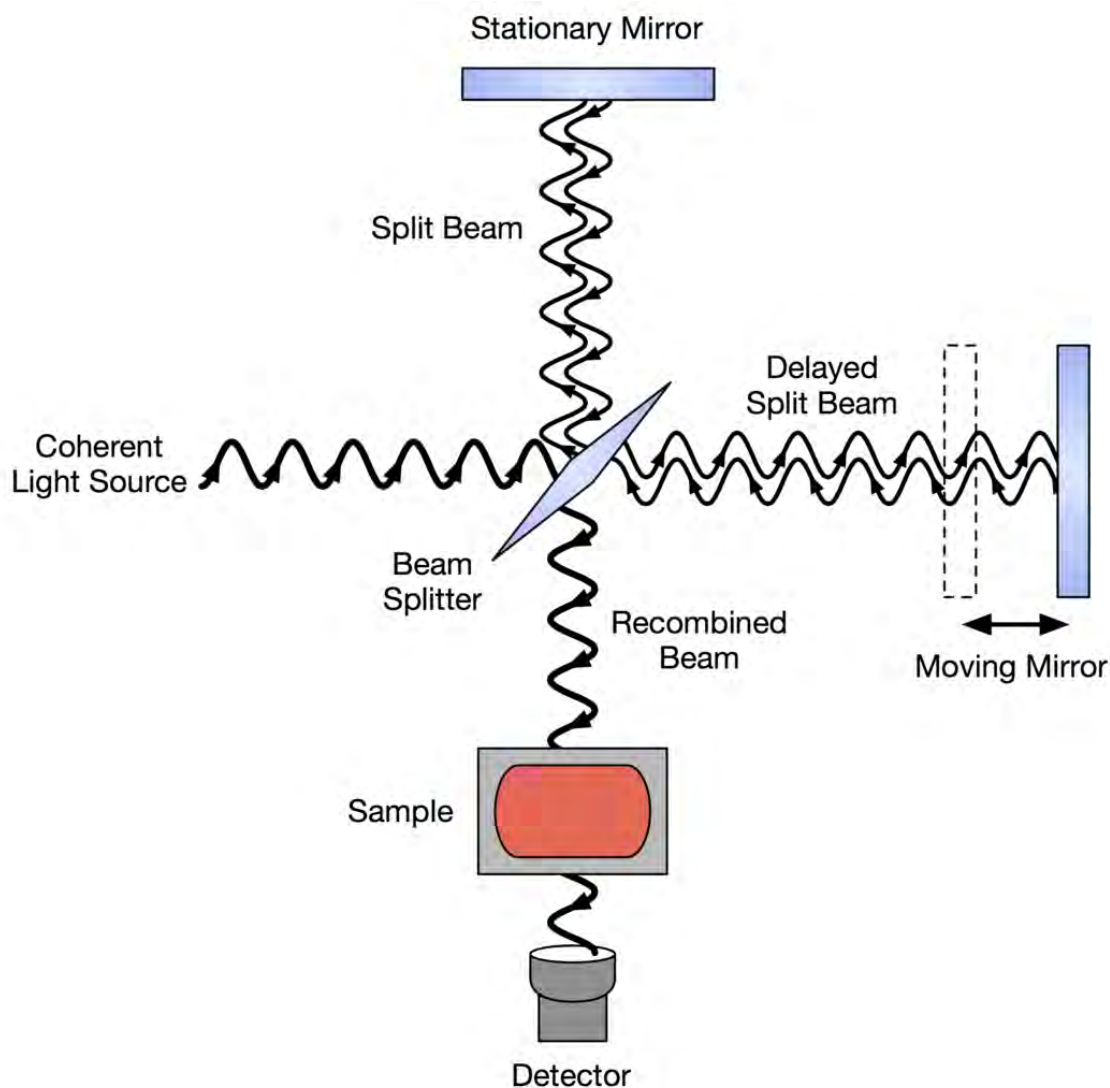


**Fig. 3.5** Schematic diagram of Fourier Transform Infrared spectroscope.

refocused on the detector after exiting the sample chamber. The interference pattern produced by the difference in optical path length between the two mirrors is known as an interferogram. An interferogram may be created by adjusting the mirror position and recording the signal from the detector for various values of the mirror position. The shape of the interferogram when no sample is present is determined by characteristics such as source intensity and splitter efficiency. A Fourier transform algorithm is used to convert the interferogram (light absorption for each mirror position) into the desired result (light absorption for each wavelength). The Fourier transform converts one domain (in this case, the mirror's displacement in cm) into its inverse domain (wavenumbers in  $\text{cm}^{-1}$ ) and provide the data.



### 3.4 Electrochemical Characterisation Techniques

The techniques used to analyse the electrochemical performance of  $\text{CuCo}_2\text{S}_4$  and  $\text{CuCo}_2\text{S}_4\text{-MoS}_2$  were discussed in the following paragraphs.

#### 3.4.1 Electrochemical cell setup

A device that creates electrical energy from chemical processes or uses electrical energy to generate chemical reactions is known as an electrochemical cell. Electrochemical cells that generate an electric current are called voltaic or galvanic cells, whereas those that initiate chemical processes by electrolysis are known as electrolytic cells. An electrode is a (semi-)conductive solid that contacts with an electrolyte solution. The most used electrode types are working electrodes (WE), reference electrodes (RE), and counter electrodes (CE). The WE is the electrode under investigation, whereas the CE, or auxiliary electrode, completes the current path in the cell. A working-counter electrode pair is required in an electrochemical system with a non-zero current. The RE is the electrode that serves as an experimental reference point, as its name suggests. It serves as a point of reference for potential measurements. As a result, RE should maintain a constant potential during the assessment, ideally on an absolute scale.

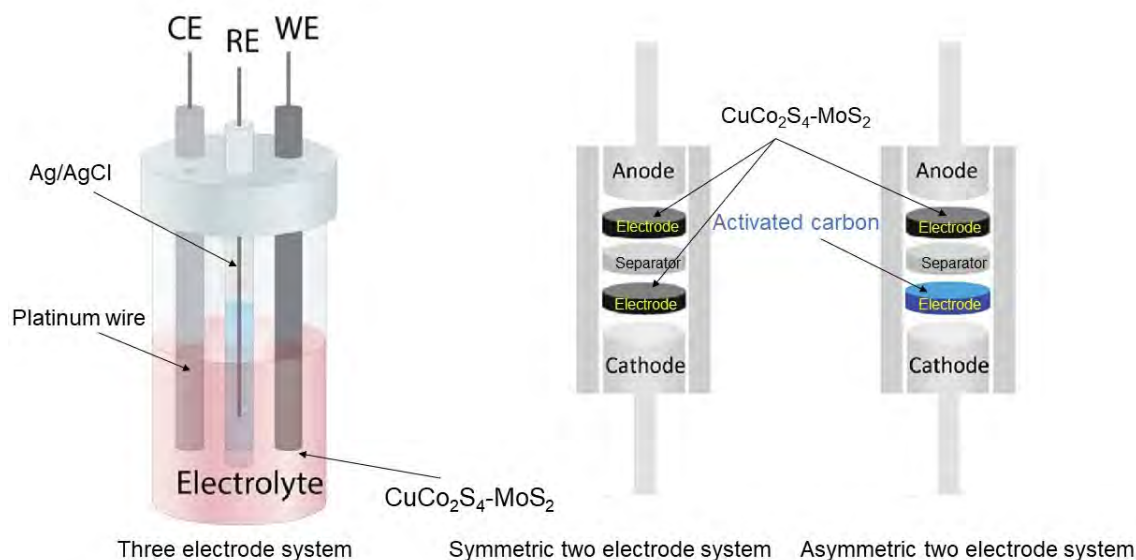


**Fig. 3.6** (a) A three-electrode system where the potential difference is measured between WE and RE, while the current passes between WE and CE. (b) A two-electrode symmetric system, where both the electrode contain the same material, and (c) a two-electrode asymmetric system, where one electrode contain the material to be investigated and another contain different material such activated carbon.

### 3.4.1.1 Three-electrode system

Fig. 3.6 (a) shows three-electrode cell designs for quiescent solution electrochemical cell. WE, RE, and CE make up the three-electrode system, which is essential in an electrochemical cell. In the three-electrode system, each of these electrodes has a distinct function. An electrode with a fixed electrode potential is referred to as a reference electrode. The RE can be used as a half cell in an electrochemical cell. When the RE is used as a half cell, it can determine the electrode potential of the other half cell. A CE is an electrode that prevents current from passing through the reference cell. It ensures that the current is the same as the WE's current. The WE is the electrode that transports electrons from and to the given substances. Three-electrode setups have an advantage over two-electrode setups in experimentation: they only measure half of the cell. The WE's potential changes are monitored apart from any changes that may occur at the CE in half cell. This isolation allows researchers to investigate electrochemical performance extensively by studying specific reaction with assurance and accuracy. Hence, the electrochemical performance of  $\text{CuCo}_2\text{S}_4$  and  $\text{CuCo}_2\text{S}_4\text{-MoS}_2$  is characterised using a three-electrode setup.

### 3.4.1.2 Two-electrode system

The most basic cell configuration is two-electrode, although the data and analysis are frequently significantly complicated. The current-carrying electrodes in a two-electrode configuration can also be utilised to monitor potential. The physical setup for the two-electrode mode anode and cathode electrodes. A diagram of a two-electrode cell arrangement is shown in Fig. 3.6 (b-c). The two-electrode configuration measures the entire cell; the potential leads to the measurement of the total voltage lowered by the current over the entire electrochemical cell comprising of anode, electrolyte, and cathode. In a few general circumstances, two-electrode setups are employed. One is in electrochemical energy devices, where measuring the whole-cell voltage is important (e.g., batteries, fuel cells, supercapacitors). The other is where the potential is unlikely to drift throughout the experiment. As a result, a two-electrode system is utilised to investigate the potential applications of an electrode. Asymmetric and symmetric two-electrode setups are the two forms of two-electrode setups. A symmetric electrode system is one in which two identical electrodes can be used as both the anode and cathode electrodes, as the name suggests [74]. On the other hand, an asymmetric electrode system typically uses a carbon-based material as the cathode (negative electrode) and material as anode (positive electrode). Both symmetric and asymmetric setups were used to investigate the possible application of the  $\text{CuCo}_2\text{S}_4\text{-MoS}_2$  as electrode for energy storage.

### 3.4.2 Preparation of electrodes

The electrochemical performance of the prepared materials was evaluated in three-electrode and symmetric as well as asymmetric two-electrode systems. In the three-electrode system, a platinum wire and an Ag/AgCl (saturated KCl) electrode were employed as the counter and reference electrodes, respectively and 0.5 M Na<sub>2</sub>SO<sub>4</sub> aqueous solution was used as the electrolyte. A homogeneous slurry of electrode materials was prepared by mixing 20 mg of active material (95% w/w), 1 mg of polyvinylidene fluoride (PVDF; 5% w/w) as binder and 200  $\mu$ L of N-methyl-2-pyrrolidone (NMP) solvent through sonication for 1 hour. The slurry was then uniformly cast onto a graphite rod with an exposed surface area of  $\sim 0.28$  cm<sup>2</sup> maintaining a mass loading of around  $\sim 2$ -3 mgcm<sup>-2</sup>. Afterward, the modified graphite rod was dried at 80 °C for 4 hours and used as the working electrode of the three-electrode cell.

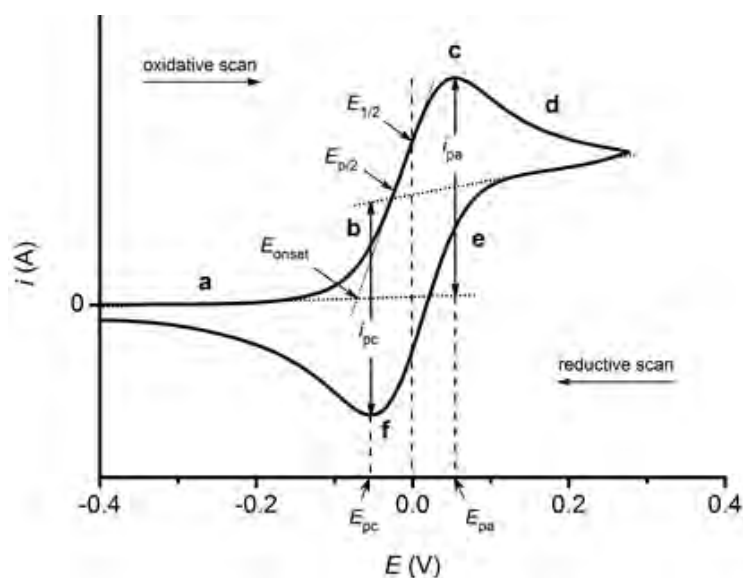
Further, a symmetric and an asymmetric two-electrode supercapacitors was fabricated via sandwich method using the prepared CuCo<sub>2</sub>S<sub>4</sub> or CuCo<sub>2</sub>S<sub>4</sub>-MoS<sub>2</sub>. To prepare the symmetric cell, the slurry of the active materials was cast on two disk shaped graphite plates having a surface area of  $\sim 0.4$  cm<sup>2</sup>. Notably, the mass loading on both electrodes were equally adjusted to  $\sim 2$ -3 mgcm<sup>-2</sup>. The modified graphite plates were employed as the anode and cathode of the symmetric supercapacitor. Then, a circular Whatman 40 filter paper soaked for 1 hour with 1 M Na<sub>2</sub>SO<sub>4</sub> aqueous electrolyte solution was sandwiched between the electrodes and placed in a customised chamber of stainless steel and sealed via screwing.

For the asymmetric two-electrode supercapacitor, initially, activated carbon (AC) was prepared from banana leaves by adopting a simple pyrolysis technique as reported by a previous investigation [75]. Briefly, washed and dried banana leaves were pulverized in a blender and then mixed with an activating agent (K<sub>2</sub>CO<sub>3</sub>) at a ratio of 1:2. The resulting mixture was pyrolyzed at 750 °C under N<sub>2</sub> atmosphere and then, the desired AC nanosheets were obtained from the carbonized samples by removing impurities. Afterward, the prepared AC and CuCo<sub>2</sub>S<sub>4</sub>-MoS<sub>2</sub> were loaded on two graphite plates with a mass ratio of 1:2. The AC and CuCo<sub>2</sub>S<sub>4</sub>-MoS<sub>2</sub> electrodes were employed as the negative and positive power source electrodes, respectively. Finally, a Whatman paper soaked with 1-butyl-3-methyl-imidazolium-chloride ([BMIM][Cl]) electrolyte was sandwiched between the two electrodes as a separator and assembled the desired asymmetric two-cell supercapacitor. To investigate the electrochemical properties of the as-synthesized nanomaterials, cyclic voltammetry, galvanostatic charge-discharge and electrochemical impedance

spectroscopy were conducted at RT using an electrochemical workstation (CHI 660E).

### 3.4.3 Cyclic Voltammetry

The reactions occurred in  $\text{CuCo}_2\text{S}_4$  and  $\text{CuCo}_2\text{S}_4\text{-MoS}_2$  during the electrochemical process were investigated by Cyclic Voltammetry (CV). CV is a strong and widely used electro-analytical technique that uses the current response of a material as a function of potential to explore a material's reduction and oxidation processes. These methods are now commonly used to assess the performance of various electrical energy storage devices, such as supercapacitors [76–78]. The voltage of the working electrode is scanned for a specified potential (known as scan window) by executing forward and reverse scans. This process produces a ‘cyclic’ sweep of potentials that can be repeated, and a cyclic voltammogram, a plot of current vs. potential, is created. The initial current response is capacitive. It arises from forming an electrical double layer (EDL) at the electrode surface, which involves a diffusion-controlled process as the voltage increases.



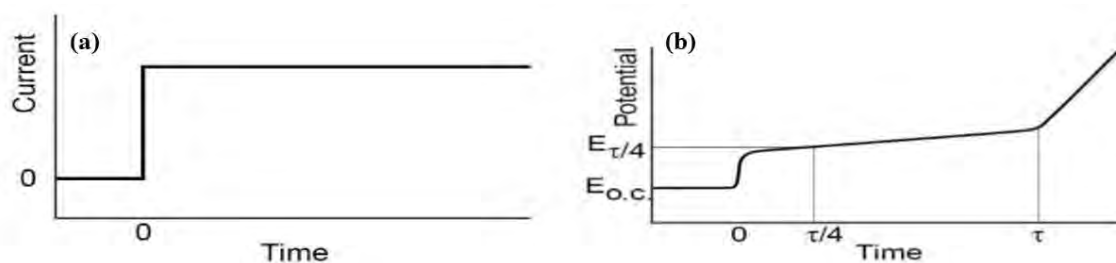
**Fig. 3.7** Typical cyclic voltammogram where  $i_{pa}$  and  $i_{pc}$  show the peak of anodic and cathodic current respectively for a reversible reaction.

Fig. 3.7 shows a scan from -0.4 V to higher positive and oxidative potentials. Initially, the potential is not enough to oxidise the electrolyte (Fig. 3.7 point a). As the electrolyte is oxidised, the current exponentially increases (b). Depletion of the electrolyte increases the diffuse double layer, and the current reaches its maximum at point c. (anodic peak current,  $i_{pa}$  for oxidation at the anodic peak potential,  $E_{pa}$ ). More positive potentials create more current, which is compensated

by increasing electrolyte distance from the electrode surface. Because electrolyte mass transport gets limited, the current decreases (d) as the potentials increase more positively until a steady state is attained. Positive potentials (oxidative scan) continue to oxidise the electrolyte until the applied potential reaches the point (e) where oxidised electrolyte can be reduced at the electrode surface. The reduction process is like oxidation, but with the scan, direction reversed and a cathodic peak ( $i_{pc}$ ) at the cathodic peak potential ( $E_{pc}$  (f)). For reversible processes, the anodic and cathodic peak currents should have identical amplitude but the opposite sign (if the cathodic peak is measured relative to the baseline after the anodic peak). The nature of the electrolyte, concentration, scan rates, and experimental circumstances all influence the amplitude of the current response and the form of the voltammograms. The CV may appear slightly distorted in shape depending on the potential window and materials of interest, indicating the presence of the faradic process, and charge storage in that potential window region by the faradic process is known as Pseudocapacitance. The charge storage and release procedures are capacitive when a CV has a rectangular form.

#### 3.4.4 Galvanostatic Charge-Discharge

Galvanostatic Charge-Discharge (GCD) analysis was carried out to get electrochemical properties (capacitance, stability etc) of  $\text{CuCo}_2\text{S}_4$  and  $\text{CuCo}_2\text{S}_4\text{-MoS}_2$ . GCD, also known as chronopotentiometry, is a reliable method for evaluating the electrochemical capacitance of materials under controlled current circumstances. It may be used to provide information on a variety of factors [79], including capacitance, resistivity, and cyclability. In this technique, a current pulse (represented as current density) is given to the working electrode. The resulting potential is measured as a function of time compared to a reference electrode, as shown in Fig. 3.8.



**Fig. 3.8** Effect of (a) change of current and (b) potential response on electrode materials in GCD.

When current is applied, the measured potential changes abruptly due to IR (internal resistance) loss. After that, it changes gradually due to the development of over-potential across the electrodes as the reactant concentration is exhausted at

the electrode surface, resulting in a voltage increment. The potential response of an ideal capacitive material in GCD shows discharge/ charge time is shown in Fig. 3.9.

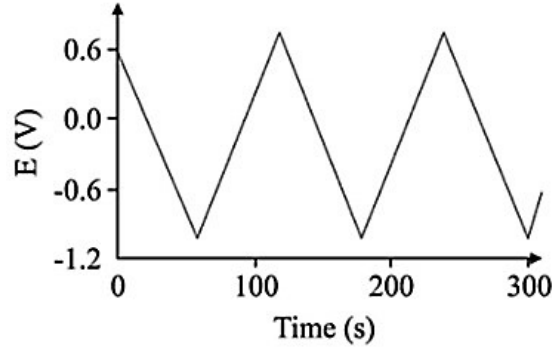


**Fig. 3.9** Potential response of an ideal electrochemical capacitor in GCD.

For the three-electrode system, the specific capacitance ( $C_{sp}$ ) values of the electrode materials were calculated from the experimentally obtained GCD curves using the following equation [80]:

$$C_{sp} (F/g) = \frac{I\Delta t}{m\Delta V} \quad (3.5)$$

For the two-electrode system, the specific capacitance values of the electrode materials were calculated from the following equation [75]:

$$C_{sp} (F/g) = \frac{2I\Delta t}{m\Delta V} \quad (3.6)$$

For the symmetric two-electrode system, the specific capacitance values of the electrode materials were calculated from the following equation [81]:

$$C_{sp} (F/g) = \frac{I\Delta t}{m\Delta V} \quad (3.7)$$

Here,  $I$  is defined as the applied current (A),  $\Delta t$  is the discharge time,  $\Delta V$  is the operating potential window and  $m$  is the total loaded mass of the active material.

### 3.4.5 Electrochemical Impedance Spectroscopy

Electrochemical Impedance Spectroscopy (EIS) is utilised to determine the double-layer capacitance and characterise electrode processes and complex interfaces at various A.C. frequencies. EIS is a method for establishing a direct link between a real system and an idealised equivalent circuit consisting of discrete electrical components (Resistance, capacitor, and inductor) in series and parallel configurations. Electrochemical capacitors are systems that use either blocking/polarizable electrodes (in the case of EDLC, planar geometries, or high surface area porous

electrodes) or electroactive electrode materials (in the case of redox capacitors) [79].

Impedance data is usually represented in one of two ways. One is a Nyquist plot, which shows how  $Z_{img}$  varies with  $Z_{real}$ , and the other is a Bode plot, which shows how phase angle varies with frequency. Electrochemical processes contain several types of resistance arising from solution, charge transfer, electrical double layer (capacitor), diffusion, etc. Their equivalent circuit, known as the Randles circuit, can be derived from an EIS analysis. A Randles circuit is an equivalent electrical circuit made up of an active electrolyte resistance  $R_S$  in series with a parallel combination of double-layer capacitance  $C_{dl}$  and a faradaic reaction impedance. EIS provides the ability to diagnose as well as apply electrochemical processes. It is feasible to determine the type of electroactive material using EIS. Fig. 3.10 shows a typical Nyquist plot and its equivalent circuit.

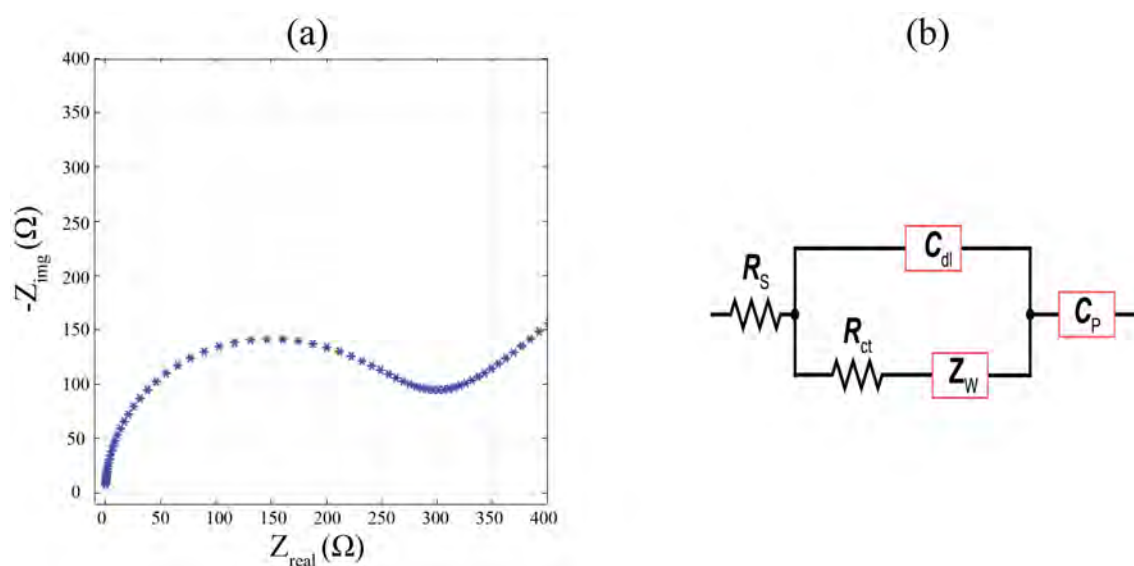


**Fig. 3.10** (a) A typical Nyquist plot and (b) its equivalent circuit.

### 3.4.6 Determination of energy density and power density

The amount of energy contained in the mass of a system or material is proportional to its energy density. The presence of a high energy density does not indicate how rapidly that energy can be consumed. Power density measures power output per unit volume and is defined as the quantity of power (time rate of energy transfer) per unit volume. It expresses the speed at which its energy can be released. A high energy density does not always imply a high power density, and it is possible to have a high energy density and a low power density. The energy density as a function of power density is presented in Ragone plot. Ragone plot is used for comparing energy density of various energy storing devices [82].

The energy density ( $E$ ) and power density ( $P$ ) values of the synthesised materials were calculated from the known highest value of capacitance obtained from GCD curves in a symmetric two-electrode system using the following equations [83–85]:

$$E(Wh/kg) = \frac{C_{sp} \times (\Delta V)^2 \times 1000}{8 \times 3600} \quad (3.8)$$

$$P(W/kg) = \frac{E \times 3600}{\Delta t} \quad (3.9)$$

And the energy density ( $E$ ) and power density ( $P$ ) values of the synthesised materials were calculated from the known highest value of capacitance obtained either from CV or GCD curves in an asymmetric two electrode system using the following equations:

$$E(Wh/kg) = \frac{C_{sp} \times (\Delta V)^2 \times 1000}{2 \times 3600} \quad (3.10)$$

$$P(W/kg) = \frac{E \times 3600}{\Delta t} \quad (3.11)$$

Where  $E$  is the energy density of the electrode,  $P$  is the average power density,  $C_{sp}$  is the specific capacitance of the active material,  $\Delta V$  is the operating voltage range or potential window and  $\Delta t$  is the discharge time in GCD curve.



## CHAPTER 4

### RESULTS AND DISCUSSION

The structural, morphological and electrochemical properties of as-synthesized  $\text{CuCo}_2\text{S}_4$  and  $\text{CuCo}_2\text{S}_4\text{-MoS}_2$  nanocomposite were investigated using different experimental techniques. The outcomes of the investigations are presented below.

#### 4.1 Structural, Morphological and Elemental Characterisations

##### 4.1.1 Crystal structure

The crystallographic structure of the prepared nanomaterials was investigated by analysing their Rietveld refined powder XRD spectra [86]. For the refinement, the background was calibrated using the X'Pert HighScore Plus software package with the granularity of 44 and a bending factor of 0 [87]. In Fig. 4.1 (a), the diffraction peaks exhibited by  $\text{CuCo}_2\text{S}_4$  could be indexed at (220), (311), (100),

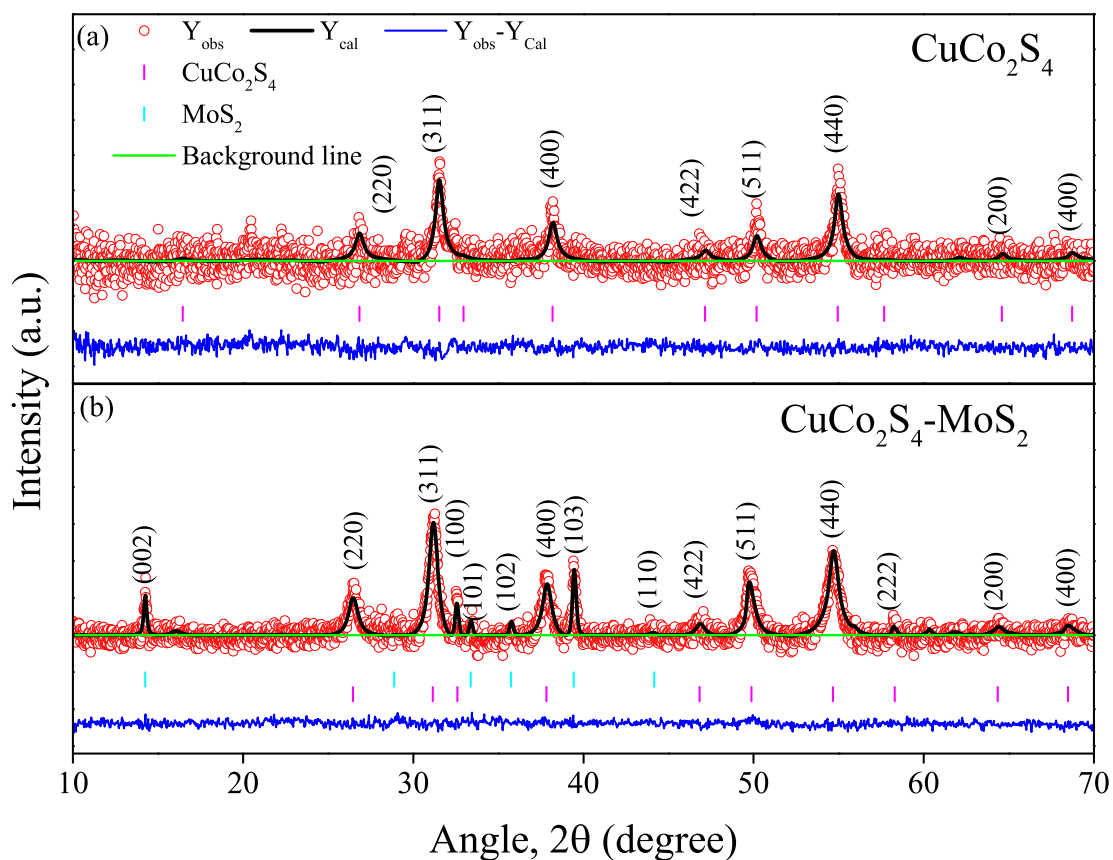


**Fig. 4.1** Rietveld refined powder XRD patterns of (a)  $\text{CuCo}_2\text{S}_4$  and (b)  $\text{CuCo}_2\text{S}_4\text{-MoS}_2$ .

(400), (422), (511), (440), (222), (200) and (400) planes (JCPDS card no 42-1450) which conformed to the cubic phase of spinal  $\text{CuCo}_2\text{S}_4$  based on  $F d-3 m$  space group [7, 88–90]. Notably, no impurity or secondary phases were detected in the XRD spectrum which confirmed the high phase-purity of synthesised  $\text{CuCo}_2\text{S}_4$ .

Fig. 4.1 (b) displayed the Rietveld refined powder XRD spectrum of the prepared  $\text{CuCo}_2\text{S}_4\text{-MoS}_2$  nanocomposite. The coexistence of two phases corresponding to  $\text{CuCo}_2\text{S}_4$  and  $\text{MoS}_2$  in the crystal lattice was confirmed by the Bragg positions which implied the successful formation of the nanocomposite. The diffraction peaks of  $\text{MoS}_2$  nanosheets were associated with single-phase 2H hexagonal structure (space group  $P63/mmc$ , JCPDS card no. 37-1492) [66, 91]. It was intriguing to note that the intensity and sharpness of the XRD peaks of  $\text{CuCo}_2\text{S}_4\text{-MoS}_2$  nanocomposite were significantly higher as compared to the peaks associated with  $\text{CuCo}_2\text{S}_4$  which indicated an enhancement in the degree of crystallisation due to the incorporation of  $\text{MoS}_2$  [92].

Further, it was quantitatively determined the crystallinity of the prepared samples from their Rietveld refined XRD patterns using the following equation [87]:

$$\text{Crystallinity}(\%) = 100 \times \sum \frac{I_{\text{net}}}{\sum (I_{\text{tot}} - I_{\text{const. bgr}})} \quad (4.1)$$

where,  $I_{\text{net}}$ ,  $I_{\text{tot}}$  and  $I_{\text{const.bgr}}$  represented the crystal intensity, total intensity and background intensity, respectively. Using this equation, the crystallinity of  $\text{CuCo}_2\text{S}_4$  and  $\text{CuCo}_2\text{S}_4\text{-MoS}_2$  were calculated to be 40% and 88%, respectively.

**Table 4.1** Crystallographic parameters for all the constituents of the nanomaterials obtained after refinement.

Sample	Constituent	Crystallographic Phase	Space group	$a$ (Å)	$b$ (Å)	$c$ (Å)	$V$ (Å <sup>3</sup> )	R factors
$\text{CuCo}_2\text{S}_4$	$\text{CuCo}_2\text{S}_4$	Cubic	$F d-3 m$	9.431	9.431	9.431	846.054	$R_{wp} = 4.23$ $R_p = 3.41$ $R_{exp} = 3.78$ $\chi^2 = 1.12$
$\text{CuCo}_2\text{S}_4\text{-MoS}_2$	$\text{CuCo}_2\text{S}_4$	Cubic	$F d-3 m$	9.501	9.501	9.501	851.971	$R_{wp} = 2.86$ $R_p = 2.25$ $R_{exp} = 2.55$ $\chi^2 = 1.12$
	$\text{MoS}_2$	Hexagonal	$P63/mmc$	3.160	3.160	12.290	106.281	$R_{wp} = 2.67$ $R_p = 2.13$ $R_{exp} = 2.54$ $\chi^2 = 1.05$

Moreover, using Bragg's law [93], we had calculated the interlayer spacing, “ $d$ ” of MoS<sub>2</sub> before and after the incorporation of CuCo<sub>2</sub>S<sub>4</sub>. Notably, the “ $d$ ” values of ultrasonicated MoS<sub>2</sub> and the MoS<sub>2</sub> in the nanocomposite (CuCo<sub>2</sub>S<sub>4</sub>-MoS<sub>2</sub>) were found to be 0.6174 and 0.6211 nm, respectively. Such enhancement in the interlayer spacing of MoS<sub>2</sub> suggested that during the formation of CuCo<sub>2</sub>S<sub>4</sub>-MoS<sub>2</sub> nanocomposite, the nanostructured CuCo<sub>2</sub>S<sub>4</sub> had intercalated between the layers of MoS<sub>2</sub>.

In Table 4.1 the constituent phases, space group, unit cell volume and reliability ( $R$ ) factors of Rietveld refinement for the prepared nanomaterials were presented. Here, the computed lattice parameters of CuCo<sub>2</sub>S<sub>4</sub> and MoS<sub>2</sub> were in agreement with previously reported value [7, 91]. The structural parameters corresponding to CuCo<sub>2</sub>S<sub>4</sub> remained reasonably unchanged in the CuCo<sub>2</sub>S<sub>4</sub>-MoS<sub>2</sub> nanocomposite demonstrating insignificant deformation in the crystal structure of individual CuCo<sub>2</sub>S<sub>4</sub> phase during the synthesis of the nanocomposite [66].

#### 4.1.2 Surface morphology

The surface morphology of the prepared CuCo<sub>2</sub>S<sub>4</sub> and CuCo<sub>2</sub>S<sub>4</sub>-MoS<sub>2</sub> was investigated by observing the FESEM images as demonstrated in Fig. 4.2 (a) and (b), respectively. As shown in Fig. 4.2 (a), the surface of the synthesised nanostructured CuCo<sub>2</sub>S<sub>4</sub> was slightly agglomerated and not fairly homogeneous. In contrast, Fig. 4.2 (b) demonstrated that the surface morphology of CuCo<sub>2</sub>S<sub>4</sub>-MoS<sub>2</sub> nanocomposite was satisfactorily homogeneous with less agglomeration as compared to CuCo<sub>2</sub>S<sub>4</sub>. Fig. 4.2 (b) also revealed the in-situ formation of the nanosheet of MoS<sub>2</sub> during the hydrothermal synthesis of CuCo<sub>2</sub>S<sub>4</sub>-MoS<sub>2</sub> nanocomposite.

The detailed structure of CuCo<sub>2</sub>S<sub>4</sub>-MoS<sub>2</sub> was further studied by TEM. Fig. 4.3 (a) showed that CuCo<sub>2</sub>S<sub>4</sub> nanoparticles were distributed along with MoS<sub>2</sub> nanosheets. In Fig. 4.3 (b), the dark and pale part indicated the presence of CuCo<sub>2</sub>S<sub>4</sub> and MoS<sub>2</sub>, as ultra-thin and partially transparent edge of CuCo<sub>2</sub>S<sub>4</sub>-MoS<sub>2</sub> which was an indication of the nanosheet structure of MoS<sub>2</sub>. Fig. 4.3 (c) presented the HRTEM image of CuCo<sub>2</sub>S<sub>4</sub>-MoS<sub>2</sub> nanocomposite. The magnified HRTEM image showed the lattice spacing were 0.286 nm and 0.621 nm, which were corresponding to (311) plane of cubic CuCo<sub>2</sub>S<sub>4</sub> and the (002) plane of hexagonal MoS<sub>2</sub>, respectively. This result confirmed the formation of heterojunction between CuCo<sub>2</sub>S<sub>4</sub> and MoS<sub>2</sub> through the hydrothermal process and showed the intimate contact between CuCo<sub>2</sub>S<sub>4</sub> and MoS<sub>2</sub>. Few bright concentric diffraction rings observed in the SAED pattern (Fig. 4.3 (d)) revealing the polycrystalline feature of the nanocomposite due to the coexistence of

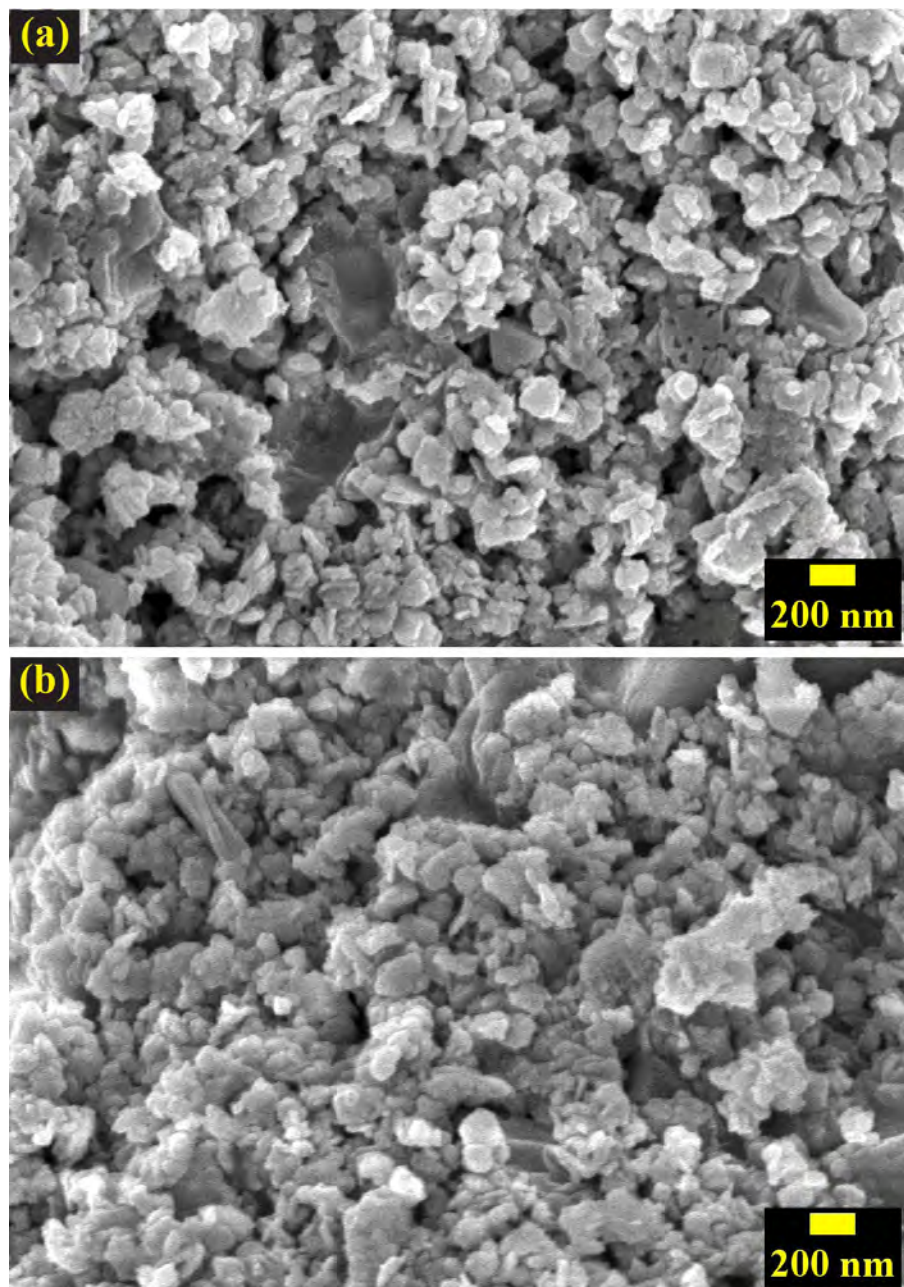


**Fig. 4.2** FESEM images of (a)  $\text{CuCo}_2\text{S}_4$  and (b)  $\text{CuCo}_2\text{S}_4\text{-MoS}_2$ .

$\text{CuCo}_2\text{S}_4$  and  $\text{MoS}_2$ . In Fig. 4.3 (d), the diffraction rings could be assigned to the  $\text{CuCo}_2\text{S}_4$  (220), (311), (511) and (440) and  $\text{MoS}_2$  (103) and (105) crystal faces from inside to outside, further, demonstrated the successful formation of  $\text{CuCo}_2\text{S}_4\text{-MoS}_2$ . Also, the crystal faces were in well agreement with the XRD pattern, supporting also the cubic and hexagonal structure of  $\text{CuCo}_2\text{S}_4$  and  $\text{MoS}_2$ , respectively. The heterojunction formed between  $\text{CuCo}_2\text{S}_4$  and  $\text{MoS}_2$  might help to increase the electroactive sites significantly and greatly enhanced the electrolyte penetration to improve the desired electrochemical performance [94,95].

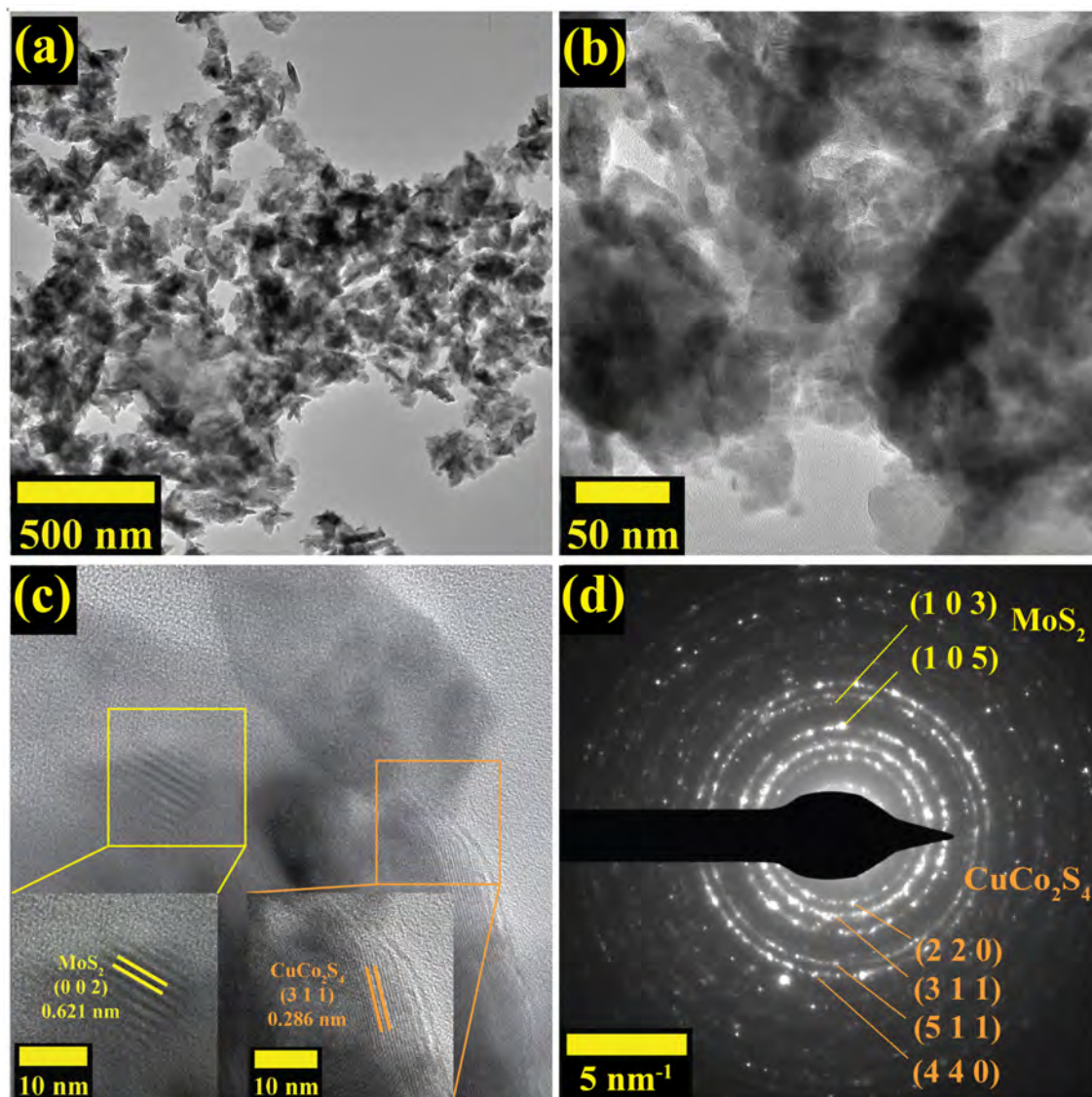


**Fig. 4.3** (a and b) TEM images of  $\text{CuCo}_2\text{S}_4\text{-MoS}_2$  (c) HRTEM image of  $\text{CuCo}_2\text{S}_4\text{-MoS}_2$  with lattice fringes of  $\text{MoS}_2$  indicated in bottom left inset and lattice fringes of  $\text{CuCo}_2\text{S}_4$  indicated in bottom right inset and (d) SAED pattern of  $\text{CuCo}_2\text{S}_4\text{-MoS}_2$ .

### 4.1.3 Chemical composition

The elemental composition of the prepared materials was analysed by EDX. Fig. 4.4 (a) and (b) demonstrated the EDX spectra of  $\text{CuCo}_2\text{S}_4$  and  $\text{CuCo}_2\text{S}_4\text{-MoS}_2$ , respectively. The formation of  $\text{CuCo}_2\text{S}_4$  was confirmed by comparing the experimentally obtained mass and atom percentages of the desired elements, i.e. Cu, Co and S with the theoretical values (Table 4.2) [96], Their excellent agreement evinced the phase-purity of  $\text{CuCo}_2\text{S}_4$ . In addition to the peaks of Cu and Co atoms, the EDX spectrum of  $\text{CuCo}_2\text{S}_4\text{-MoS}_2$  only included peaks of Mo at around 2.4 keV. The absence of S peak was due to near similar characteristics energy of Mo and S. Since the energy resolution of the instrument was higher than the energy difference of Mo and S, only one experimental Gaussian peak of Mo was generated [97].

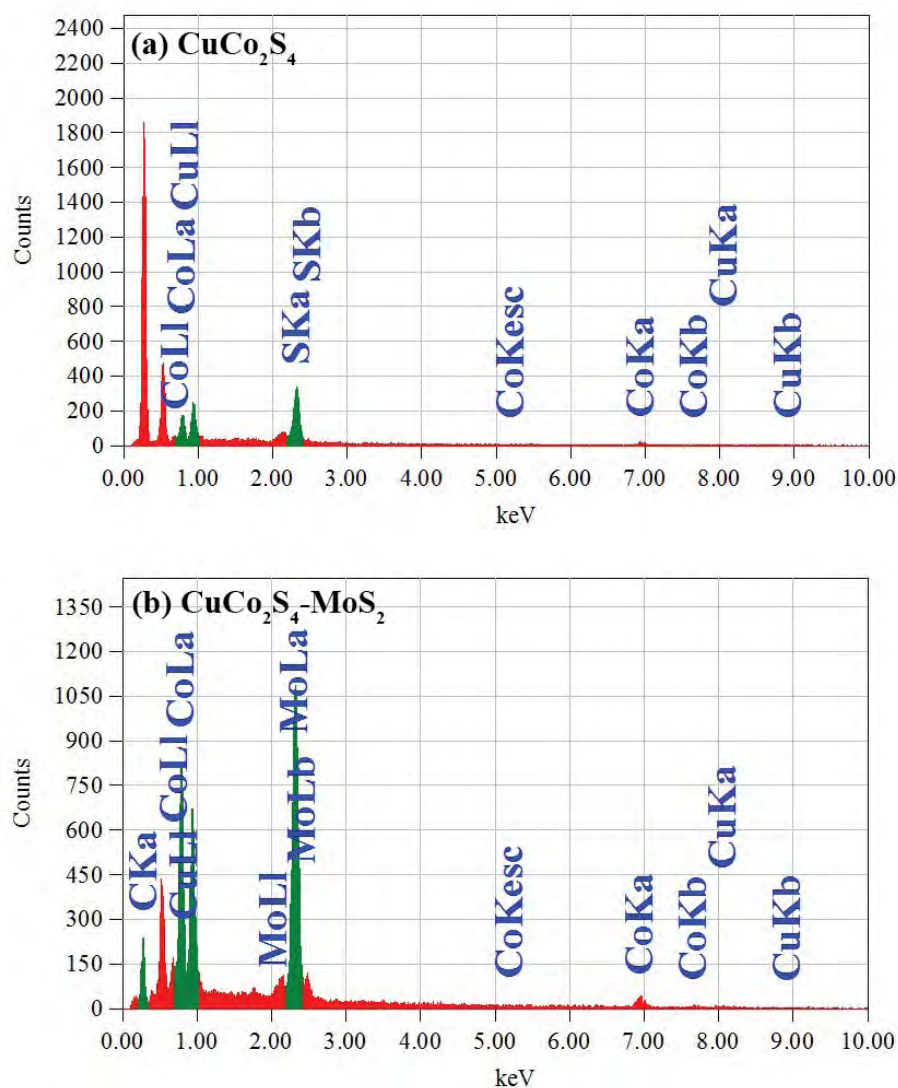


**Fig. 4.4** EDX spectra of (a)  $\text{CuCo}_2\text{S}_4$  and (b)  $\text{CuCo}_2\text{S}_4\text{-MoS}_2$ .

**Table 4.2** Mass and atom percentages of elements in  $\text{CuCo}_2\text{S}_4$  and  $\text{CuCo}_2\text{S}_4\text{-MoS}_2$  as obtained via EDX and theoretical analysis.

Element	Mass (%) (Theoretical)	Mass (%) (Experimental)	Atom (%) (Theoretical)	Atom (%) (Experimental)
Cu	20.52	22.92	13.53	16.65
Co	38.06	42.09	25.10	32.97
S	41.42	35.00	61.38	50.38
Total	100	100	100	100

FTIR spectroscopy was conducted for further analysis of the synthesized materials. The FTIR spectra of  $\text{CuCo}_2\text{S}_4$  and  $\text{CuCo}_2\text{S}_4\text{-MoS}_2$  obtained over the range of 400 to 1350  $\text{cm}^{-1}$  were compared in Fig. 4.5. For a further insight, the full spectra was also provided in the inset. As observed in the figure, the peaks around 650  $\text{cm}^{-1}$  and 1120  $\text{cm}^{-1}$  in the FTIR spectrum of  $\text{CuCo}_2\text{S}_4$ , could be assigned to the vibration of Cu-S and Co-S, respectively [98]. After the incorporation of  $\text{MoS}_2$  with  $\text{CuCo}_2\text{S}_4$ , an additional vibrational band had arisen at around 420  $\text{cm}^{-1}$  which could be attributed to the  $\gamma_{\text{as}}$  Mo-S vibration [99]. Moreover, a distinct peak was also

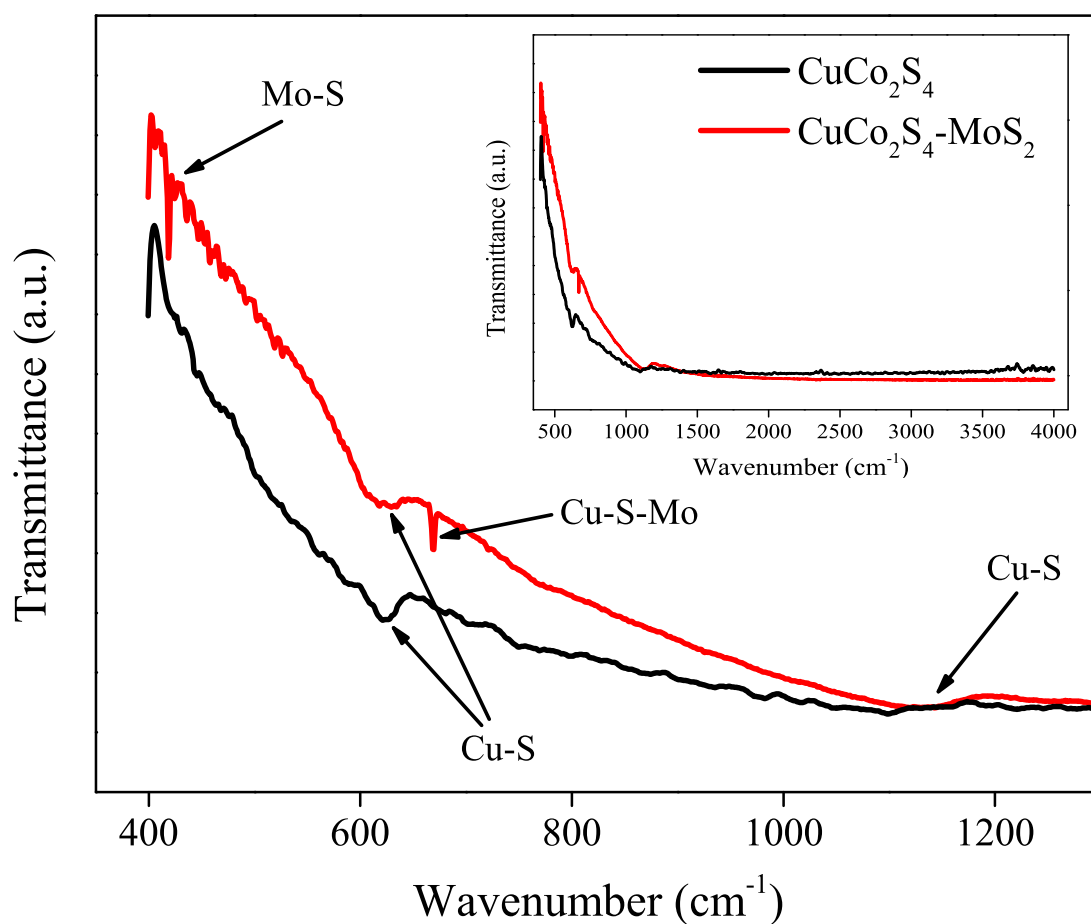


**Fig. 4.5** FTIR spectra of  $\text{CuCo}_2\text{S}_4$  and  $\text{CuCo}_2\text{S}_4\text{-MoS}_2$ . Inset showed the full FTIR spectra obtained for wavenumber ranging from 400  $\text{cm}^{-1}$  to 4000  $\text{cm}^{-1}$ .

observed at around  $670\text{ cm}^{-1}$  for the possible vibration of Cu-S-Mo bond provided further evidence for the formation of  $\text{CuCo}_2\text{S}_4\text{-MoS}_2$  nanocomposite.

## 4.2 Electrochemical Performance

### 4.2.1 Electrochemical performance in three-electrode system

The electrochemical performance of the prepared nanomaterials and bulk  $\text{MoS}_2$  were evaluated by CV, GCD and EIS analyses in a three-electrode system using  $0.5\text{ M Na}_2\text{SO}_4$  aqueous solution as electrolyte. The obtained data was compared under identical experimental conditions. In Fig. 4.6 (a), the comparison of the CV curves of  $\text{MoS}_2$ ,  $\text{CuCo}_2\text{S}_4$  and  $\text{CuCo}_2\text{S}_4\text{-MoS}_2$  were demonstrated at a fixed scan rate of  $20\text{ mVs}^{-1}$  in the same potential window of  $-0.5$  to  $0.5\text{ V}$ . Clearly, the integrated CV area of  $\text{CuCo}_2\text{S}_4\text{-MoS}_2$  electrode was significantly larger than that of both  $\text{MoS}_2$  and  $\text{CuCo}_2\text{S}_4$  electrodes which was an indication of the higher charge storage capacity on the surface of  $\text{CuCo}_2\text{S}_4\text{-MoS}_2$  electrode. Moreover, the enhanced current response and absence of redox peaks in the CV curve of  $\text{CuCo}_2\text{S}_4\text{-MoS}_2$  electrode suggested that the electrical conductivity and stability of  $\text{CuCo}_2\text{S}_4$  were considerably improved due to the incorporation of dilute amount of  $\text{MoS}_2$ .

For providing deeper insight, the CV curves of the  $\text{MoS}_2$ ,  $\text{CuCo}_2\text{S}_4$  and  $\text{CuCo}_2\text{S}_4\text{-MoS}_2$  electrodes obtained at various scan rates of  $5$ ,  $10$ ,  $20$ ,  $50$  and  $100\text{ mVs}^{-1}$  were presented in Fig. 4.7 (a), 4.8 (a) and 4.9 (a), respectively. Notably, it was demonstrated in Fig. 4.8 (a) that a pair of redox peaks became prominent in the CV curves of  $\text{CuCo}_2\text{S}_4$  electrode at higher scan rates. It might be attributed to the occurrence of Faradaic redox reactions of  $\text{Co}^{4+}/\text{Co}^{3+}$  and  $\text{Cu}^{2+}/\text{Cu}^+$  pairs at the electrode/electrolyte interface during the electrochemical process [42, 92]. Interestingly, as seen in Fig. 4.9 (a), unlike  $\text{CuCo}_2\text{S}_4$ , the CV curves of  $\text{CuCo}_2\text{S}_4\text{-MoS}_2$  electrode were maintained the quasi-rectangle shape even at higher scan rates indicating the stabilisation of the  $\text{Co}^{4+}/\text{Co}^{3+}$  and  $\text{Cu}^{2+}/\text{Cu}^+$  redox couples. The ability to retain the quasi-rectangle shape with increasing scan rate indicates excellent electrochemical reversibility and fast ion transportation rate of the  $\text{CuCo}_2\text{S}_4\text{-MoS}_2$  electrode [100].

In Fig. 4.6 (b), the comparative GCD profiles of  $\text{MoS}_2$ ,  $\text{CuCo}_2\text{S}_4$  and  $\text{CuCo}_2\text{S}_4\text{-MoS}_2$  electrodes were illustrated at the same applied current density of  $0.5\text{ Ag}^{-1}$ . Conspicuously, the GCD curve of the  $\text{CuCo}_2\text{S}_4\text{-MoS}_2$  exhibited longer discharge time in comparison with the  $\text{MoS}_2$  and  $\text{CuCo}_2\text{S}_4$  electrodes. The GCD curves of  $\text{MoS}_2$ ,  $\text{CuCo}_2\text{S}_4$  and  $\text{CuCo}_2\text{S}_4\text{-MoS}_2$  electrodes at different current densities ranging from  $0.5$  to  $5\text{ Ag}^{-1}$  were presented in Fig. 4.7 (b), 4.8 (b) and 4.6 (b), respectively. Clearly,



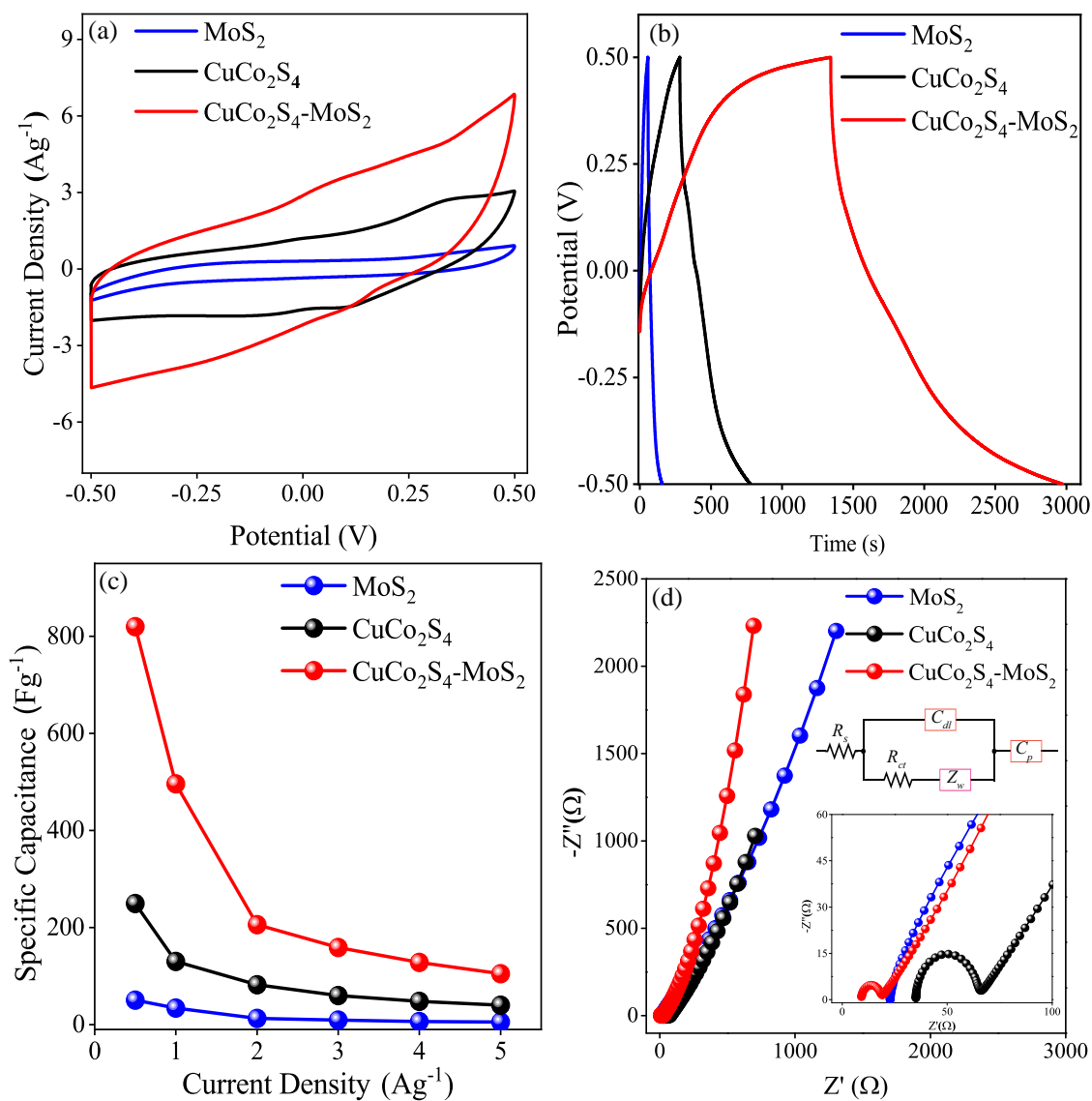


**Fig. 4.6** Electrochemical performance of MoS<sub>2</sub>, CuCo<sub>2</sub>S<sub>4</sub> and CuCo<sub>2</sub>S<sub>4</sub>-MoS<sub>4</sub> electrodes in three-electrode system: (a) CV curves at a fixed scan rate of 20 mVs<sup>-1</sup>, (b) GCD curves at a fixed current density of 0.5 Ag<sup>-1</sup> (c) variation of  $C_{sp}$  (Fg<sup>-1</sup>) with increasing current densities and (d) Nyquist plots.

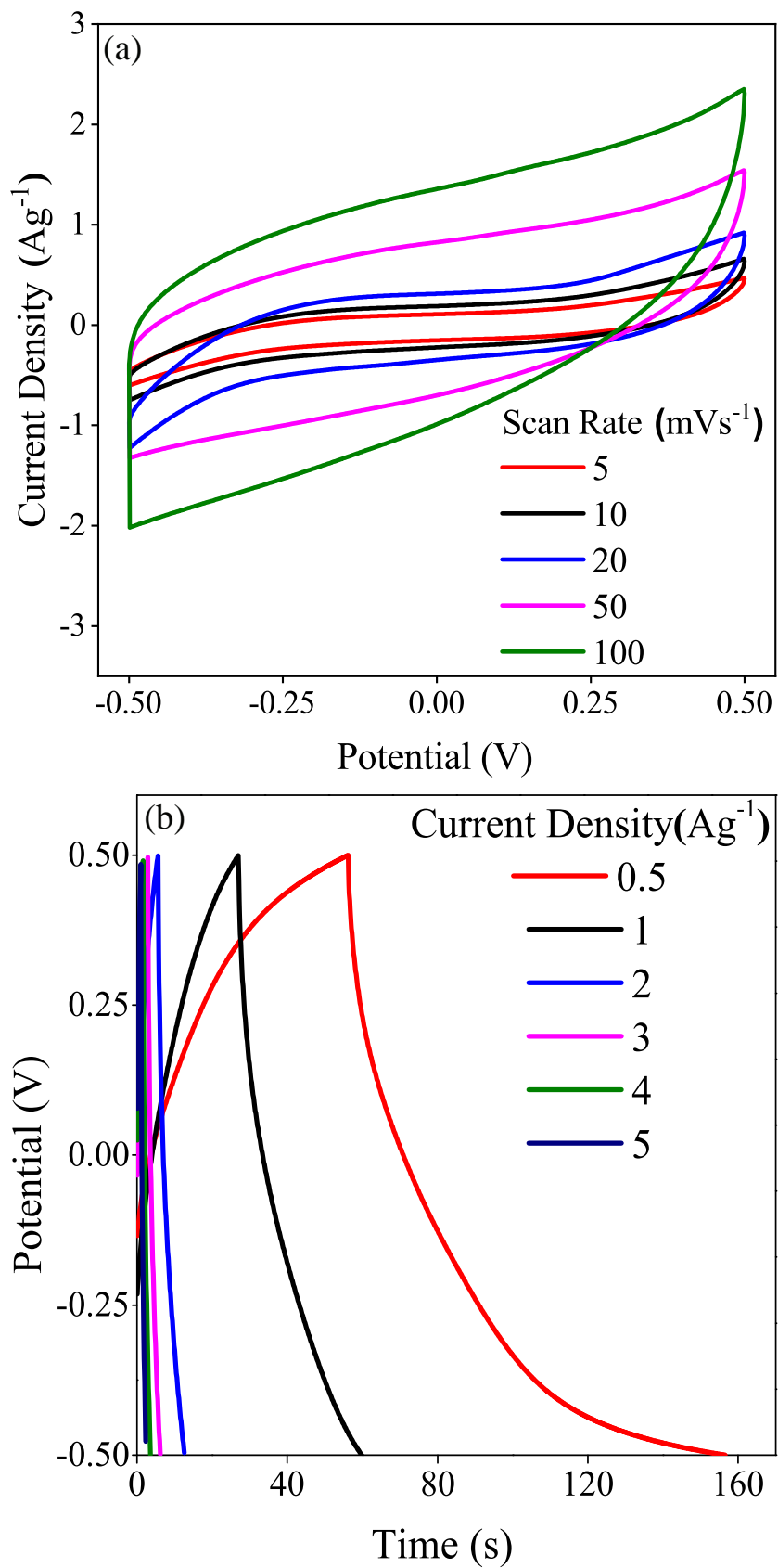


**Fig. 4.7** Electrochemical behaviour of MoS<sub>2</sub> measured in three-electrode system in aqueous electrolyte (0.5 M Na<sub>2</sub>SO<sub>4</sub>) within the potential range of -0.5 to 0.5 V; (a) CV curves at various scan rates and (b) GCD curves at different current densities.

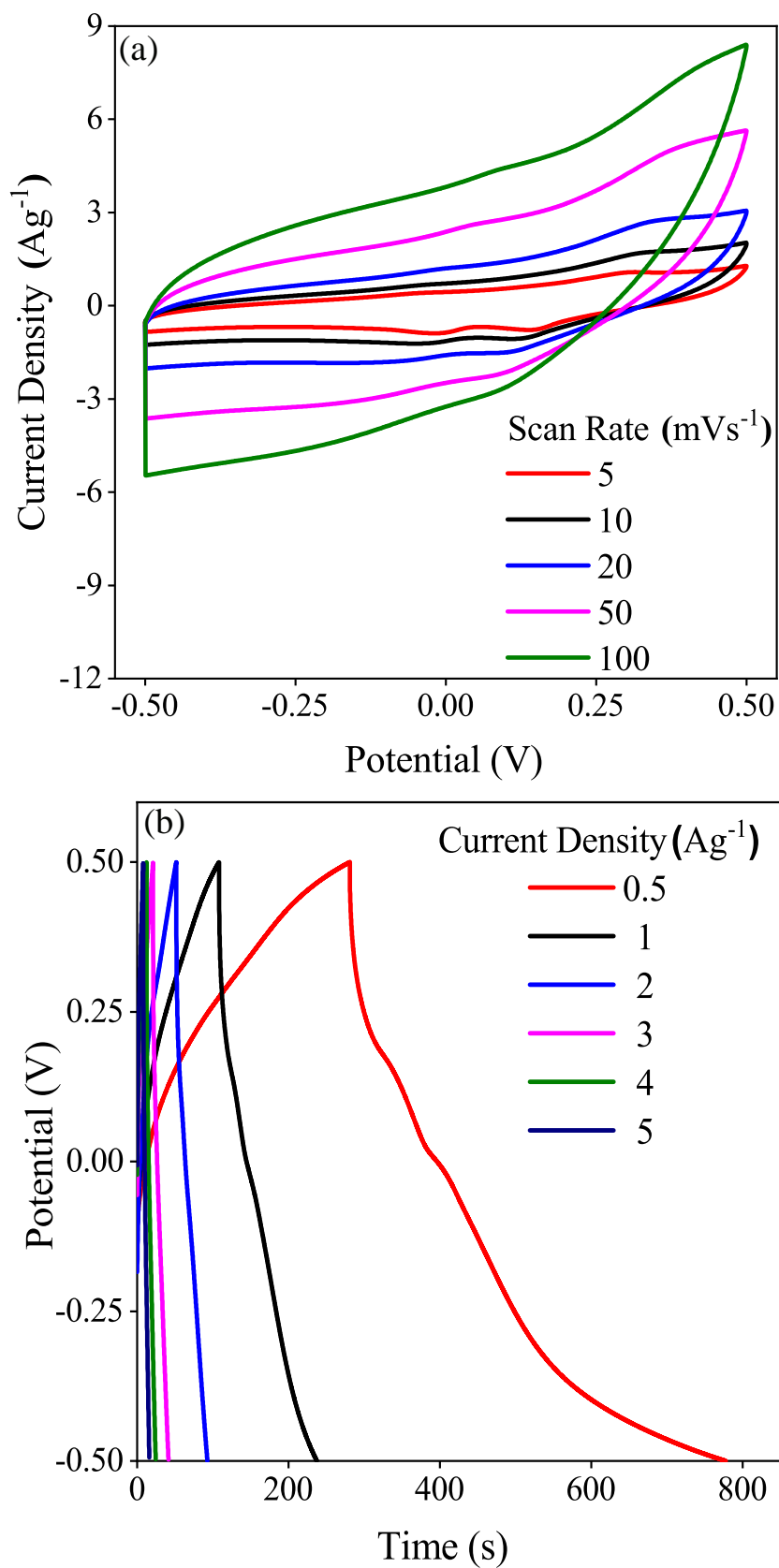


**Fig. 4.8** Electrochemical behavior of  $\text{CuCo}_2\text{S}_4$  measured in three-electrode system in aqueous electrolyte (0.5 M  $\text{Na}_2\text{SO}_4$ ) within the potential range of -0.5 to 0.5 V; (a) CV curves at various scan rates and (b) GCD curves at different current densities.

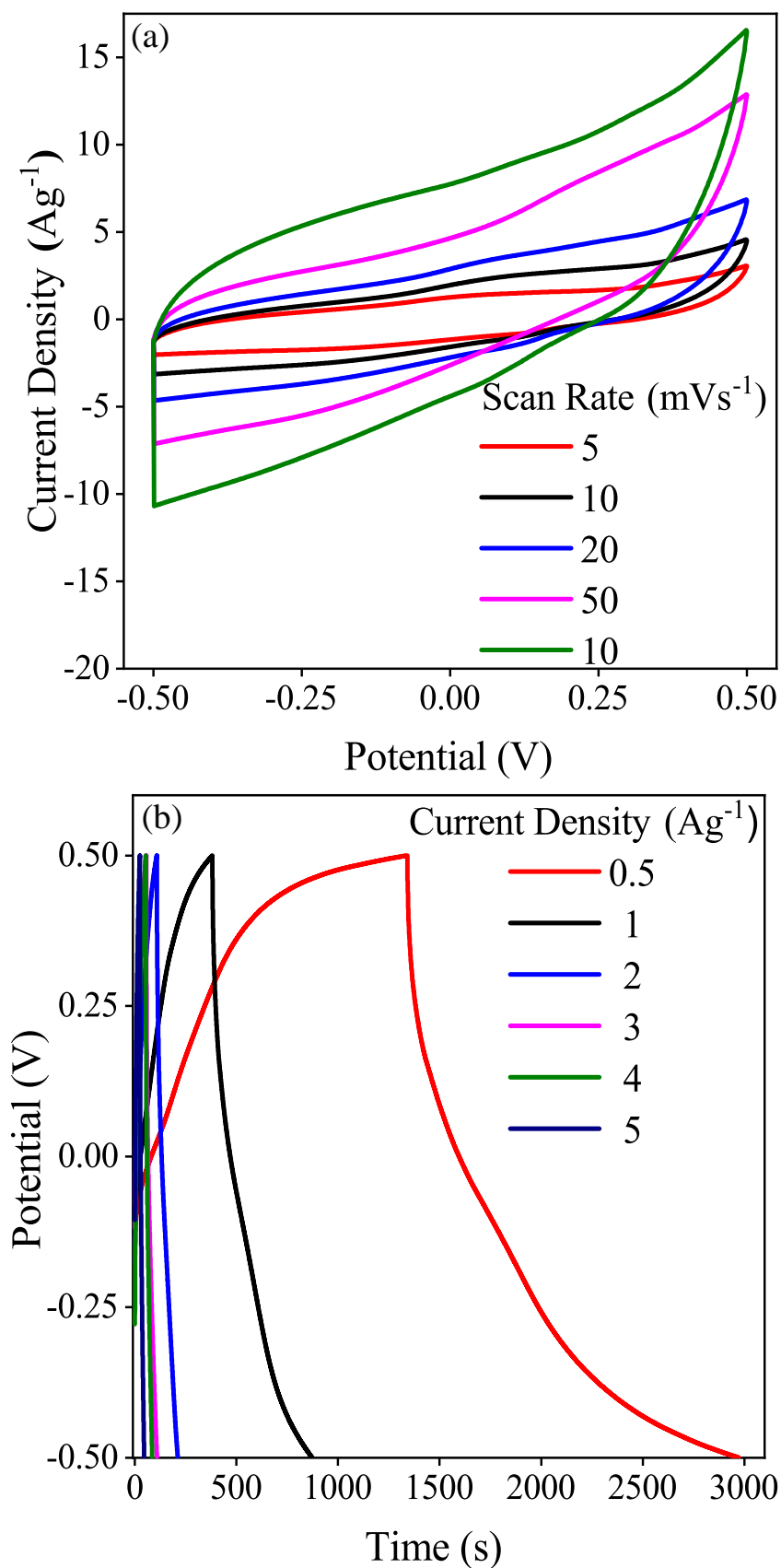


**Fig. 4.9** Electrochemical behaviour of CuCo<sub>2</sub>S<sub>4</sub>-MoS<sub>2</sub> measured in three-electrode system in aqueous electrolyte (0.5 M Na<sub>2</sub>SO<sub>4</sub>) within the potential range of -0.5 to 0.5 V; (a) CV curves at various scan rates and (b) GCD curves at different current densities.

at all the current densities, the discharge time of the  $\text{CuCo}_2\text{S}_4\text{-MoS}_2$  electrode was remarkably higher than the other two electrode materials.

Further, specific capacitance ( $C_{\text{sp}}$ ) was calculated at different current densities from the GCD curves using Eqn. 3.5 and plotted the results in Fig. 4.6 (c). It was observed that the maximum  $C_{\text{sp}}$  value ( $820 \text{ Fg}^{-1}$ ) of  $\text{CuCo}_2\text{S}_4\text{-MoS}_2$  electrode was much larger than that of both  $\text{MoS}_2$  ( $50 \text{ Fg}^{-1}$ ) and  $\text{CuCo}_2\text{S}_4$  electrodes ( $249 \text{ Fg}^{-1}$ ) at the same current density ( $0.5 \text{ Ag}^{-1}$ ). Even at high current densities, the  $\text{CuCo}_2\text{S}_4\text{-MoS}_2$  electrode retained larger  $C_{\text{sp}}$  as compared to the other two electrode materials.

The charge transfer kinetics of the prepared nanomaterials were investigated by conducting EIS analysis. In Fig. 4.6 (d), the Nyquist plots of  $\text{MoS}_2$ ,  $\text{CuCo}_2\text{S}_4$  and  $\text{CuCo}_2\text{S}_4\text{-MoS}_2$  electrodes were illustrated which were obtained over the frequency range of 100 kHz to 0.01 Hz with the alternating voltage amplitude of 10 mV at the open-circuit potential (OCP). The lower inset of Fig. 4.6 (d) demonstrated an enlarged view of the high frequency region of the Nyquist plots. In Table 4.3, different charge transfer kinetic parameters of the electrodes were presented as obtained by fitting the EIS data to the equivalent electrical circuit [101] model shown in the upper inset of Fig. 4.6 (d). Briefly, the real axis intercept of the curve at high frequency region represented the internal resistance ( $R_s$ ) of the electrochemical systems and the diameter of the semicircle provided the interfacial charge transfer resistance ( $R_{\text{ct}}$ ) between the electrode and electrolyte [100].

In the Table 4.3, it was evident that the  $R_s$  value ( $9.083 \Omega$ ) of the  $\text{CuCo}_2\text{S}_4\text{-MoS}_2$  electrode was significantly smaller than that of both  $\text{MoS}_2$  ( $22.8 \Omega$ ) and  $\text{CuCo}_2\text{S}_4$  ( $35.09 \Omega$ ), verifying its lower internal resistance. The  $R_{\text{ct}}$  value of  $\text{CuCo}_2\text{S}_4$  had also significantly reduced to  $9.154 \Omega$  from  $29.2 \Omega$  due to the incorporation of  $\text{MoS}_2$  which revealed the enhanced surface conductivity of the  $\text{CuCo}_2\text{S}_4\text{-MoS}_2$  nanocomposite. Notably, the inclined straight line at the low frequency region of the Nyquist plots corresponded to the mass transfer resistance (Warburg impedance,  $Z_W$ ) controlled by a diffusion process [38]. In Fig. 4.6 (d), the higher slope of the  $\text{CuCo}_2\text{S}_4\text{-MoS}_2$  line as compared to  $\text{CuCo}_2\text{S}_4$  yielded lower  $Z_W$ , indicated faster diffusion capability of ions on its surface. All of the outcomes of EIS analysis clearly evinced the enhanced ion transfer capability and conductivity of  $\text{CuCo}_2\text{S}_4\text{-MoS}_2$  electrode which were also supported by the CV and GCD analyses.

**Table 4.3** Values of  $R_s$ ,  $R_{ct}$ ,  $C_{dl}$ ,  $Z_W$  and  $C_p$  in the three-electrode system obtained by fitting with equivalent circuit.

Sample	$R_s$ ( $\Omega$ )	$R_{ct}$ ( $\Omega$ )	$C_{dl}$ ( $\mu F$ )	$Z_W$ ( $\Omega$ )	$C_p$ (F)
MoS <sub>2</sub>	22.8	0.001	113.8	0.00216	0.01774
CuCo <sub>2</sub> S <sub>4</sub>	35.09	29.2	0.1593	0.0044	0.0499
CuCo <sub>2</sub> S <sub>4</sub> -MoS <sub>2</sub>	9.08	9.154	0.0854	0.00264	0.00407

#### 4.2.2 Electrochemical performance in symmetric two-electrode system

A symmetric two-electrode cells with CuCo<sub>2</sub>S<sub>4</sub> and CuCo<sub>2</sub>S<sub>4</sub>-MoS<sub>2</sub> were assembled as active electrode materials to further assess their performance for practical device applications (details related to the assembling of electrodes were explained in section 3.4.2 of chapter 3). Since MoS<sub>2</sub> showed very low specific capacitance and energy density in three electrode system than CuCo<sub>2</sub>S<sub>4</sub> and CuCo<sub>2</sub>S<sub>4</sub>-MoS<sub>2</sub>, only the later two materials were investigated. Initially, to identify the stable working potential of the assembled cells, had recorded their CV curves within different voltage windows at a fixed scan rate of 20 mVs<sup>-1</sup> in 1 M Na<sub>2</sub>SO<sub>4</sub> aqueous electrolyte. As demonstrated in Fig. 4.10 (a), distinct redox humps were prominent in the CV curves of CuCo<sub>2</sub>S<sub>4</sub>, indicated the occurrence of Faradaic redox reactions of cobalt and copper species in the electrolyte solution during the voltammetric scan [7]. Although, oxidation peaks were observed in CuCo<sub>2</sub>S<sub>4</sub> for all the potentials ranging from 0 to 1.0 V, the reduction peak could only be observed for potentials over 0.7 V. Interestingly, no redox peaks emerged in the CV curves of CuCo<sub>2</sub>S<sub>4</sub>-MoS<sub>2</sub> based two-electrode system for all potentials ranging between 0 to 1.0 V (Fig. 4.10 (b)). The CV curve of CuCo<sub>2</sub>S<sub>4</sub>-MoS<sub>2</sub> maintained its stable quasi-rectangular shape over the potential range of 0 to 0.7 V. Therefore, a voltage window of 0 to 0.7 V was selected for the CV measurements of both of the symmetric two-electrode cells.

For a comparative analysis, the profiles of CuCo<sub>2</sub>S<sub>4</sub> and CuCo<sub>2</sub>S<sub>4</sub>-MoS<sub>2</sub> based symmetric two-electrode cells were provided in Fig. 4.11 (a) and (b), respectively; CV at the scan rate of 20 mVs<sup>-1</sup> and GCD at the current density of 0.5 Ag<sup>-1</sup>. Clearly, the larger integrated CV area and longer discharge time of CuCo<sub>2</sub>S<sub>4</sub>-MoS<sub>2</sub> confirmed its superior charge storage potential and higher capacitance in comparison with CuCo<sub>2</sub>S<sub>4</sub> which complied with the outcomes of three-electrode system. The CV curves of CuCo<sub>2</sub>S<sub>4</sub> and CuCo<sub>2</sub>S<sub>4</sub>-MoS<sub>2</sub> electrodes, obtained at different scan rates in the symmetric two-electrode systems, were displayed in Fig. 4.12 (a) and 4.13 (a), respectively. As demonstrated by Fig 4.13(a), the shape of the CV curves of CuCo<sub>2</sub>S<sub>4</sub>-MoS<sub>2</sub> electrode were retained at high scan rates which could be a clear indication of the excellent reversibility, high rate capability and low internal resistance of the two-electrode device [7, 100].

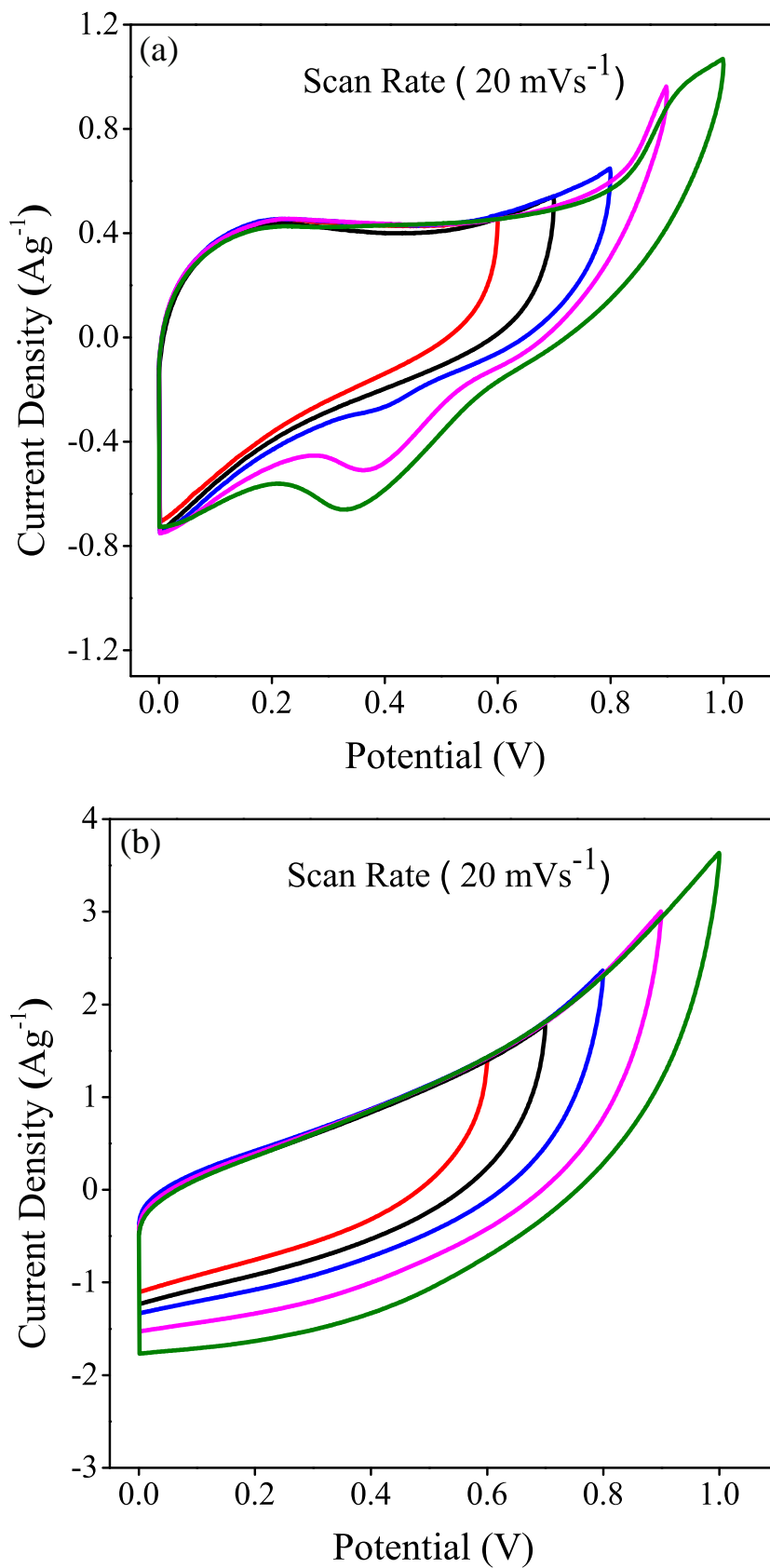


**Fig. 4.10** Potential window variation of (a)  $\text{CuCo}_2\text{S}_4$  and (b)  $\text{CuCo}_2\text{S}_4\text{-MoS}_2$  electrodes in two-electrode system.

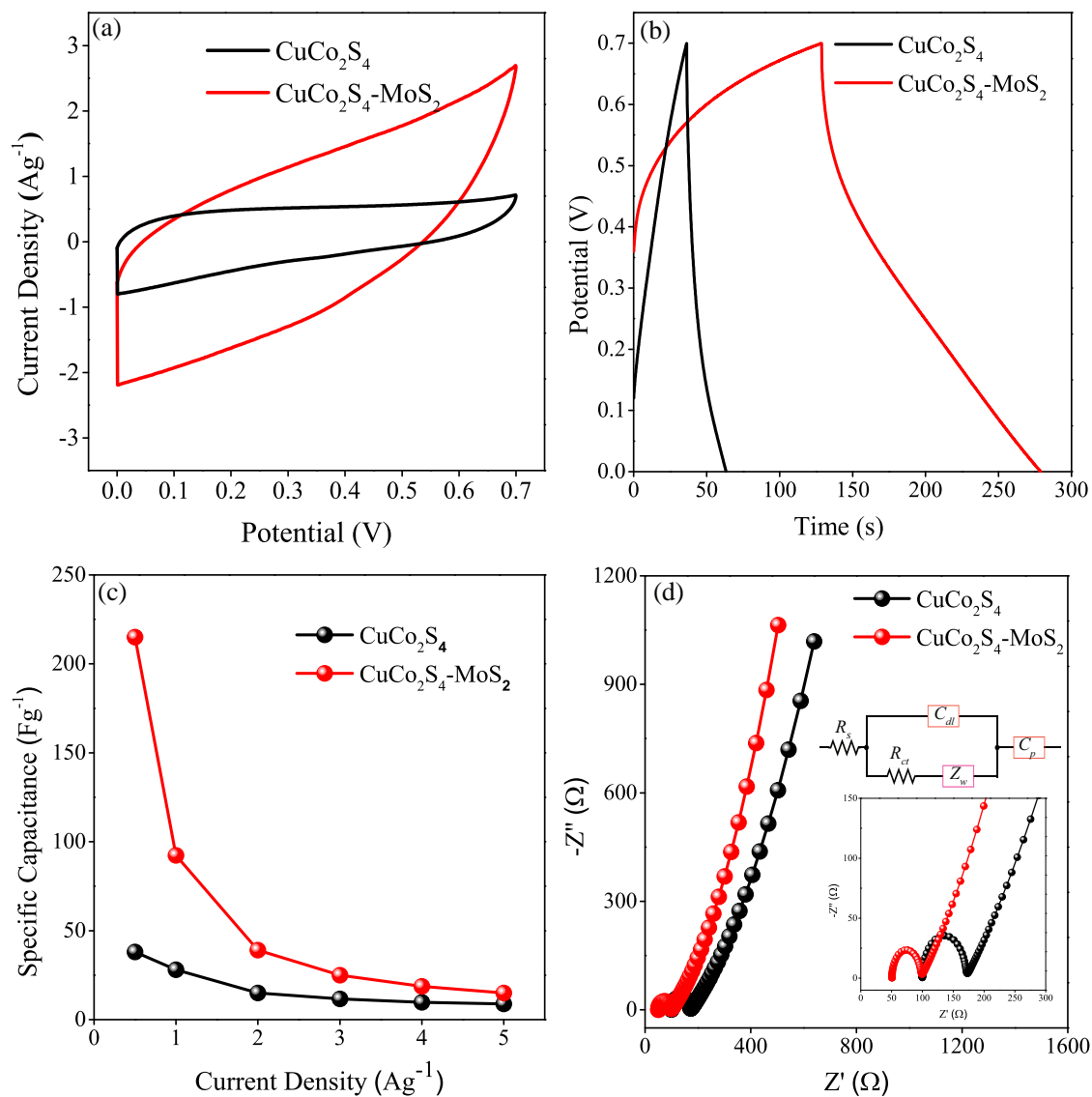


**Fig. 4.11** Electrochemical performance of  $\text{CuCo}_2\text{S}_4$  and  $\text{CuCo}_2\text{S}_4\text{-MoS}_2$  electrodes in two-electrode system: (a) CV curves at a fixed scan rate of  $20 \text{ mVs}^{-1}$ , (b) GCD curves at a fixed current density  $0.5 \text{ Ag}^{-1}$  (c) variation of  $C_{sp}$  ( $\text{Fg}^{-1}$ ) with increasing current densities and (d) Nyquist plots.



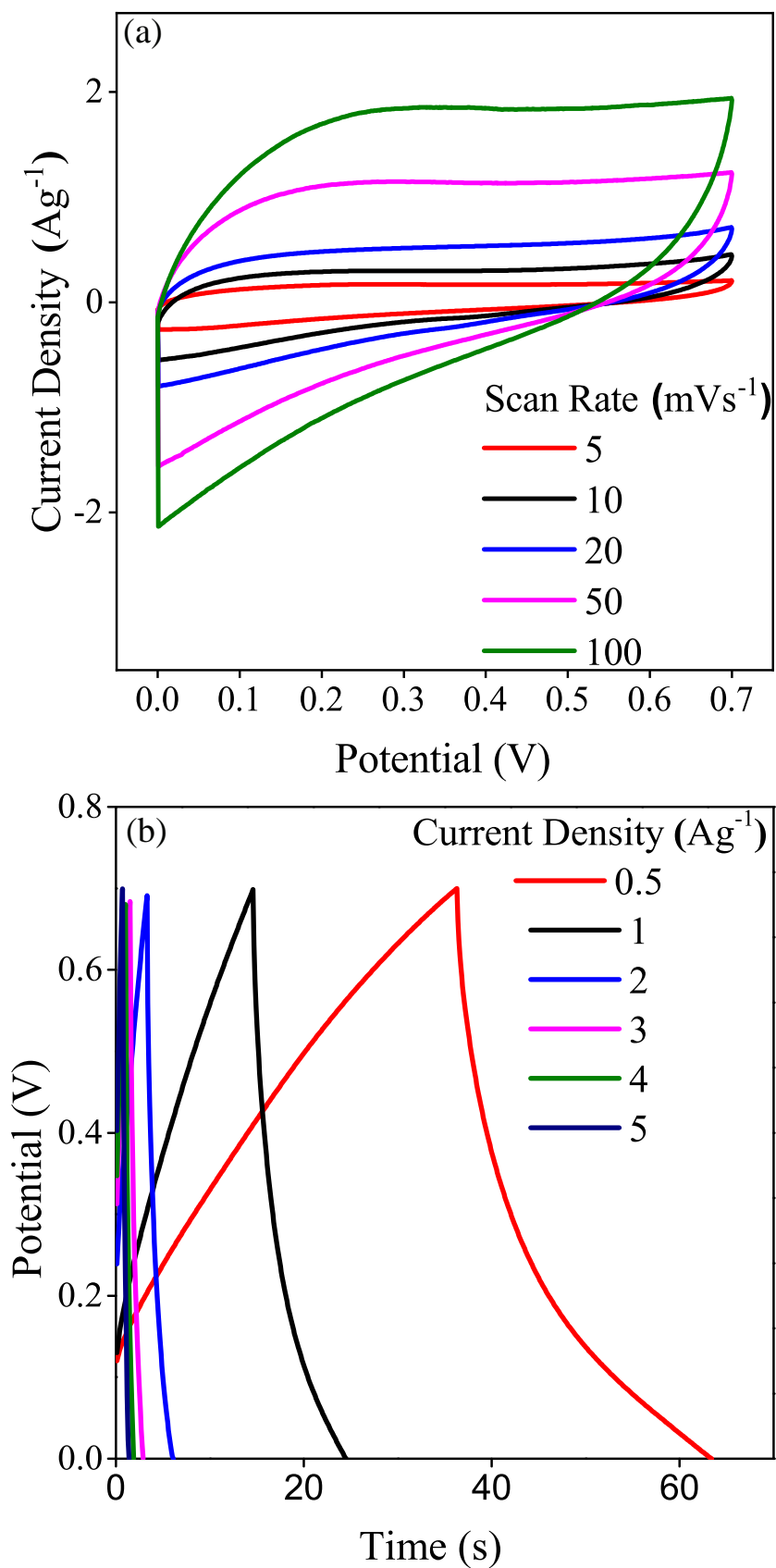


**Fig. 4.12** Electrochemical behavior of  $\text{CuCo}_2\text{S}_4$  measured in symmetric two-electrode system in aqueous electrolyte (1 M  $\text{Na}_2\text{SO}_4$ ) within the potential range of 0 to 0.7 V; (a) CV curves at various scan rates and (b) GCD curves at different current densities.

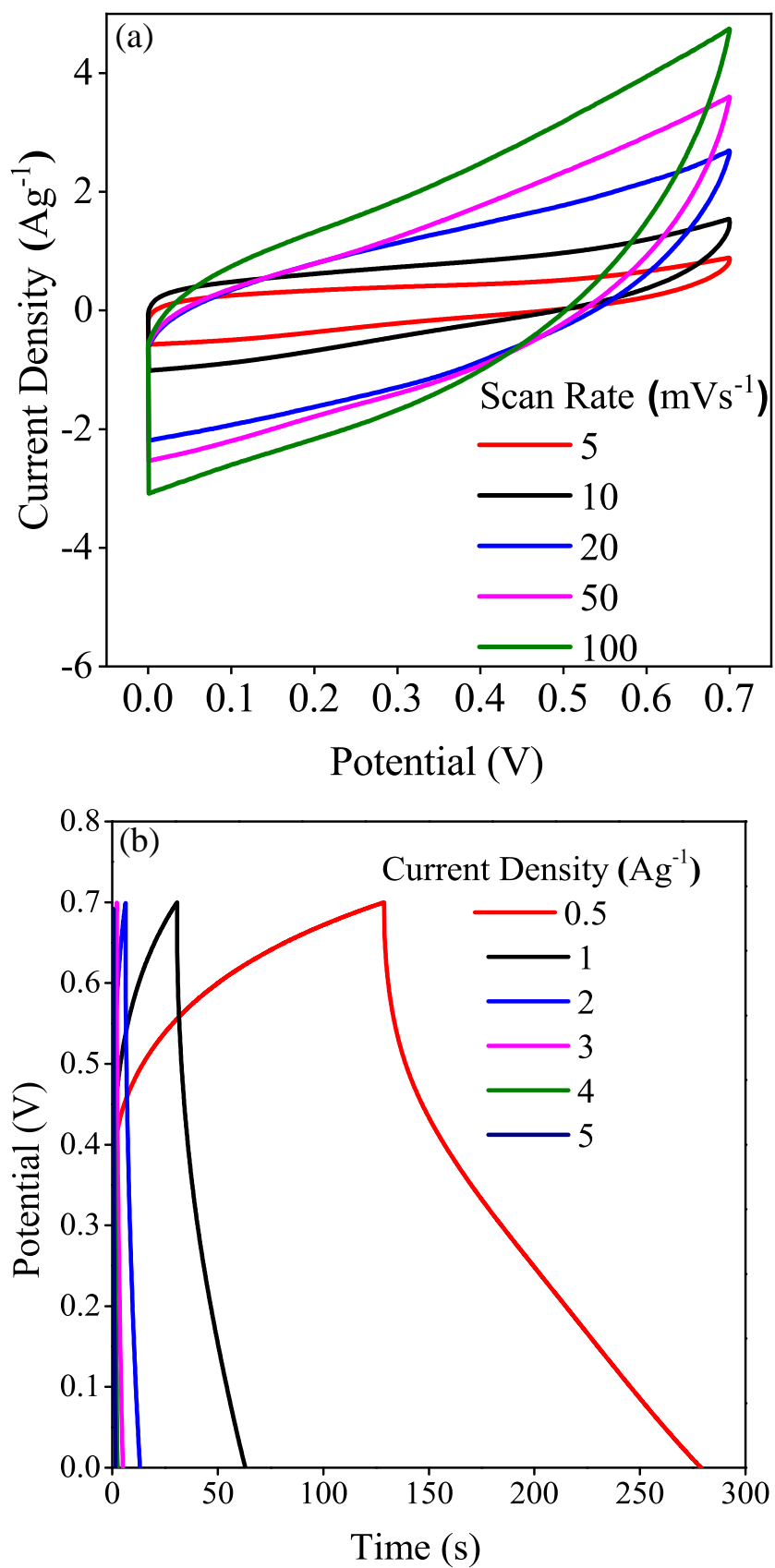


**Fig. 4.13** Electrochemical behavior of  $\text{CuCo}_2\text{S}_4\text{-MoS}_2$  measured in symmetric two-electrode system in aqueous electrolyte (1 M  $\text{Na}_2\text{SO}_4$ ) within the potential range of 0 to 0.7 V; (a) CV curves at various scan rates and (b) GCD curves at different current densities.

In order to substantiate these results, GCD analyses of  $\text{CuCo}_2\text{S}_4$  and  $\text{CuCo}_2\text{S}_4\text{-MoS}_2$  electrodes were performed in the symmetric two-electrode cells at different current densities [Fig. 4.12 (b) and 4.13 (b), respectively] and their  $C_{\text{sp}}$  values were calculated from the GCD curves. As demonstrated in Fig. 4.11 (c), a maximum  $C_{\text{sp}}$  of  $215 \text{ Fg}^{-1}$  was achieved for  $\text{CuCo}_2\text{S}_4\text{-MoS}_2$  at the current density of  $0.5 \text{ Ag}^{-1}$  which was almost five times larger than the  $C_{\text{sp}}$  ( $38 \text{ Fg}^{-1}$ ) of  $\text{CuCo}_2\text{S}_4$  at same current density.

In Fig. 4.11 (d), the Nyquist plots of the synthesized samples were displayed which were obtained by conducting EIS in the symmetric two-electrode systems over a frequency band of 100 kHz to 0.01 Hz with an amplitude of 10 mV. The calculated charge transfer kinetic parameters were tabulated in Table 4.4. Notably, the small  $R_s$  and  $R_{\text{ct}}$  values of  $\text{CuCo}_2\text{S}_4\text{-MoS}_2$  confirmed its low internal and charge transfer resistance as was also evident from the three-electrode analysis.

**Table 4.4** Values of  $R_s$ ,  $R_{\text{ct}}$ ,  $C_{\text{dl}}$ ,  $Z_W$  and  $C_p$  in the symmetric two-electrode system obtained by fitting with equivalent circuit.

Sample	$R_s$ ( $\Omega$ )	$R_{\text{ct}}$ ( $\Omega$ )	$C_{\text{dl}}$ ( $\mu\text{F}$ )	$Z_W$ ( $\Omega$ )	$C_p$ (F)
$\text{CuCo}_2\text{S}_4$	99.82	70.55	0.1379	0.005009	0.02898
$\text{CuCo}_2\text{S}_4\text{-MoS}_2$	50.61	46.67	0.2473	0.006939	0.02422

Long term cyclic performance of the fabricated symmetric supercapacitors were investigated by repeating GCD test 1000 times at the current density of  $5 \text{ Ag}^{-1}$  over the potential range of 0.0 to 0.7 V and the results were demonstrated in Fig. 4.14. As it was observed, the cell fabricated with neat  $\text{CuCo}_2\text{S}_4$  electrode exhibited only 79% capacitance retention after 1000 cycles. Such a notable loss in capacitance suggested a deterioration in the chemical structure of  $\text{CuCo}_2\text{S}_4$  and/or dissolution of constituent ions during the electrochemical process. However, the  $\text{CuCo}_2\text{S}_4\text{-MoS}_2$  electrode could retain 100% of its specific capacitance after 1000 cycles indicating its excellent long-term cyclic stability.

Notably, the operational efficiency of energy storage devices significantly always depended on their energy density  $E$  and power density  $P$  [7]. The relationship between the  $E$  and  $P$  of the assembled symmetric supercapacitors was also assessed. The results had been demonstrated through Ragone plot in Fig. 4.15 and compared with other energy storage systems. The symmetric supercapacitor with  $\text{CuCo}_2\text{S}_4\text{-MoS}_2$  electrode delivered a  $E$  of  $3.65 \text{ Whkg}^{-1}$  at the  $P$  of  $87 \text{ Wkg}^{-1}$ , whereas the  $\text{CuCo}_2\text{S}_4$  electrode exhibited a very low  $E$  value of  $0.65 \text{ Whkg}^{-1}$  at the same power

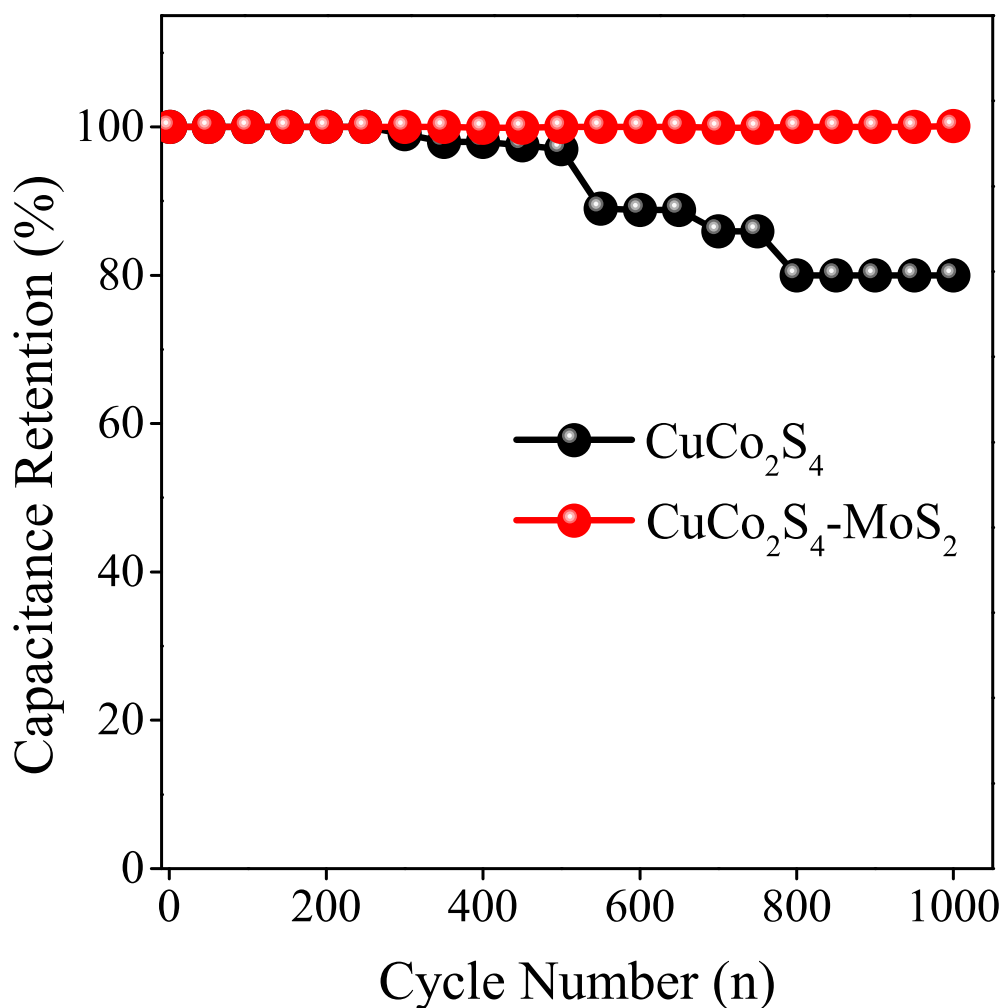


**Fig. 4.14** Retention of specific capacitance of CuCo<sub>2</sub>S<sub>4</sub> and CuCo<sub>2</sub>S<sub>4</sub>-MoS<sub>2</sub> electrodes at 5 Ag<sup>-1</sup>.

density. Such superior device efficiency of CuCo<sub>2</sub>S<sub>4</sub>-MoS<sub>2</sub> electrode strongly justified the supercapacitive behavior of the material.

To justify the enhanced supercapacitive performance of CuCo<sub>2</sub>S<sub>4</sub>-MoS<sub>2</sub>, the charge storage mechanism had been explained by a schematic diagram in Fig. 4.16. As depicted in the schematic, the charge storage mechanism at the CuCo<sub>2</sub>S<sub>4</sub>-MoS<sub>2</sub> electrode involved the intercalation of electrolyte ions during the charging process. Based on the outcomes obtained experimentally, the superior electrochemical performance of CuCo<sub>2</sub>S<sub>4</sub>-MoS<sub>2</sub> nanocomposite in comparison with CuCo<sub>2</sub>S<sub>4</sub> could be attributed to its enhanced ion adsorption capability. As evident from the XRD analysis, the interlayer spacing of MoS<sub>2</sub> existing in the nanocomposite was reasonably higher than raw bulk MoS<sub>2</sub> which indicated the intercalation of CuCo<sub>2</sub>S<sub>4</sub> between the layers of MoS<sub>2</sub>. It could be anticipated that the enlarged distance between the layers of MoS<sub>2</sub> had provided adequate space for the ion transportation

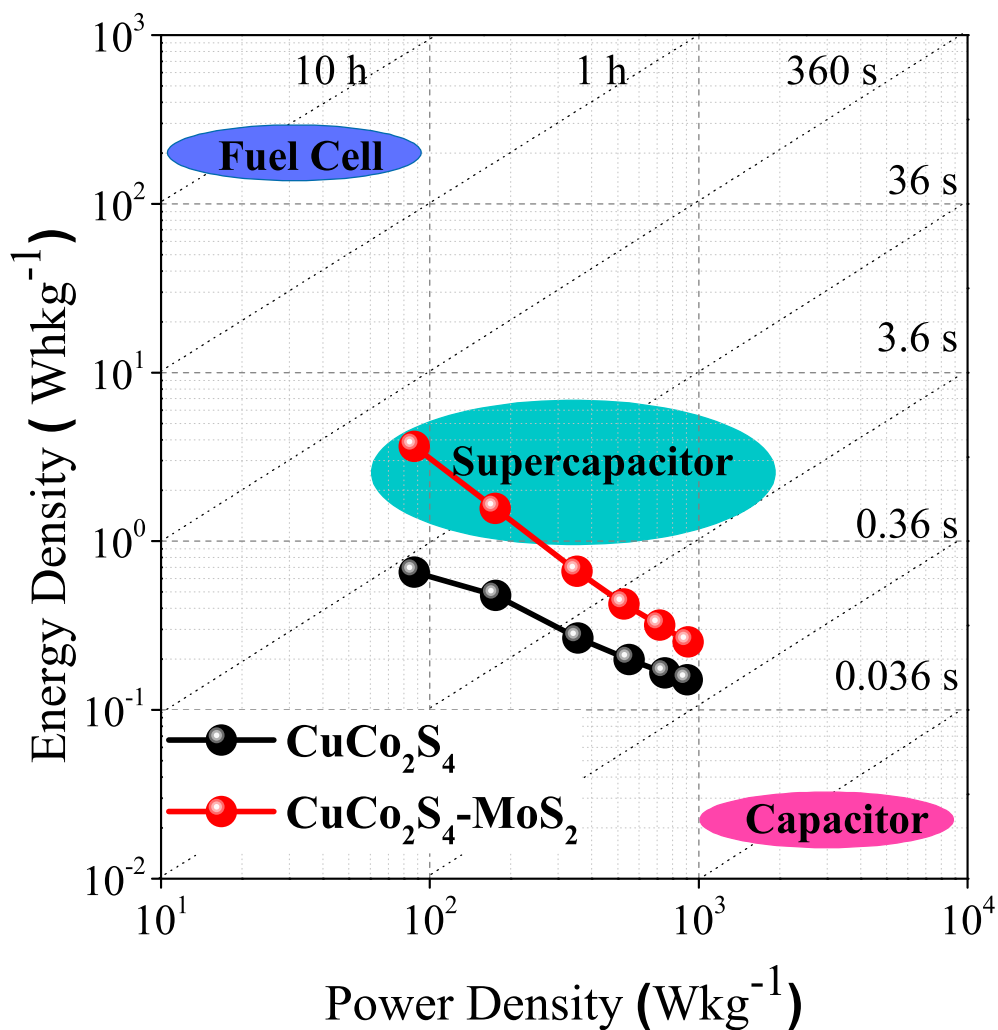
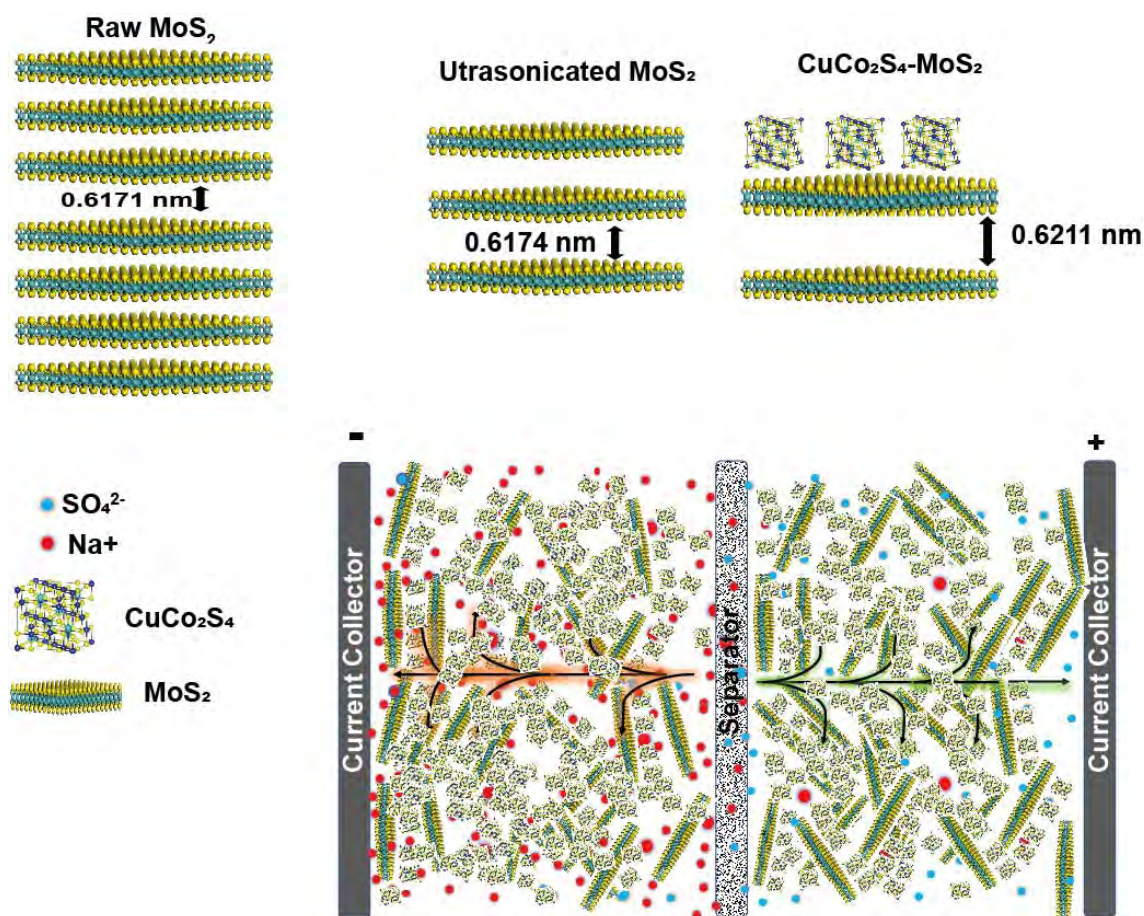


Fig. 4.15 Ragone plot of  $\text{CuCo}_2\text{S}_4$  and  $\text{CuCo}_2\text{S}_4\text{-MoS}_2$ .

inside the active material which enhanced the charge storage capacity resulting in high specific capacitance [102, 103]. The FESEM imaging confirmed the presence of few layer  $\text{MoS}_2$  sheets of nanoscopic thickness in the synthesised nanocomposite. Such few-layered structure of  $\text{MoS}_2$  nanosheets had opened numerous additional transport channels or pathways for the ions. The XRD analysis also confirmed that the degree of crystallinity of the  $\text{CuCo}_2\text{S}_4\text{-MoS}_2$  nanocomposite was significantly enhanced due to the interaction of  $\text{MoS}_2$  [42]. A number of previous investigations [92, 104] had demonstrated that the crystallinity of the electrode material played a vital role in the electrochemical performance of supercapacitors. Hence, it was speculated that the improved crystallinity of  $\text{CuCo}_2\text{S}_4\text{-MoS}_2$  nanocomposite had significantly increased its electrochemical stability resulting in longer cycle life.



**Fig. 4.16** Schematic illustration of charge storage mechanism at the CuCo<sub>2</sub>S<sub>4</sub>-MoS<sub>2</sub> nanocomposite in symmetric two-electrode system.

### 4.2.3 Electrochemical performance of the asymmetric CuCo<sub>2</sub>S<sub>4</sub>-MoS<sub>2</sub>//AC device

The large-scale industrial applications of symmetric two-electrode cells, limited by their low-energy density [105, 106]. Typically, asymmetric devices demonstrated significantly higher charge storage capacity as compared to symmetric devices. This was because of the fact that with different electrode materials, the working voltage window of asymmetric devices could be extended beyond the thermodynamic decomposition potential of water (1.2 V) [7, 107, 108]. Therefore, to develop a more efficient supercapacitor with high energy density, an asymmetric CuCo<sub>2</sub>S<sub>4</sub>-MoS<sub>2</sub>//AC supercapacitor was assembled using [BMIM][Cl] electrolyte soaked Whatman paper as the separator. In this assessment, only CuCo<sub>2</sub>S<sub>4</sub>-MoS<sub>2</sub> was investigated due to higher specific capacitance and energy density than CuCo<sub>2</sub>S<sub>4</sub>. The charges stored on negative and the positive electrodes were balanced to achieve the optimal performance based on the charge balanced theory ( $q^+ = q^-$ ). The charge on each electrode depends on its mass loading ( $m$ ), potential window ( $\Delta V$ ), and specific capacitance ( $C$ ) as represented by [109, 110]:

$$q = C \times m \times \Delta V \quad (4.2)$$

$$\frac{m^+}{m^-} = \frac{C^- \times \Delta E^-}{C^+ \times \Delta E^+} \quad (4.3)$$

According to this equation, the mass ratio between CuCo<sub>2</sub>S<sub>4</sub>-MoS<sub>2</sub> and AC was calculated to be 1:2. Hence, the total mass loading was 2 mg cm<sup>-2</sup>.

In Fig. 4.17 (a), the CV curves of the device obtained at different scan rates were presented. It could be observed that the stable working potential window of the fabricated asymmetric cell had been extended to 1.6 V which was higher than that of commercial aqueous electrolyte AC supercapacitors.

In Fig. 4.17 (b), the GCD curves of the CuCo<sub>2</sub>S<sub>4</sub>-MoS<sub>2</sub>//AC device were illustrated at various current densities in the range of 0.5 to 5 Ag<sup>-1</sup>. From the GCD profiles, the  $C_{sp}$  was calculated and the result presented in Fig. 4.17 (c) as a function of current density. Notably, the maximum  $C_{sp}$  of 107 Fg<sup>-1</sup> was achieved at the current density of 0.5 Ag<sup>-1</sup>. The cyclic stability of the CuCo<sub>2</sub>S<sub>4</sub>-MoS<sub>2</sub>//AC supercapacitor was also evaluated by repeating the GCD test 1000 times at a stable current density of 5 Ag<sup>-1</sup>. As shown in Fig. 4.17 (d), the Nyquist plot of the CuCo<sub>2</sub>S<sub>4</sub>-MoS<sub>2</sub>//AC which was obtained by conducting EIS in the symmetric two-electrode systems over a frequency band of 100 kHz to 0.01 Hz with an amplitude of 10 mV. The calculated charge transfer kinetic parameters are tabulated in Table 4.5. Notably, the small

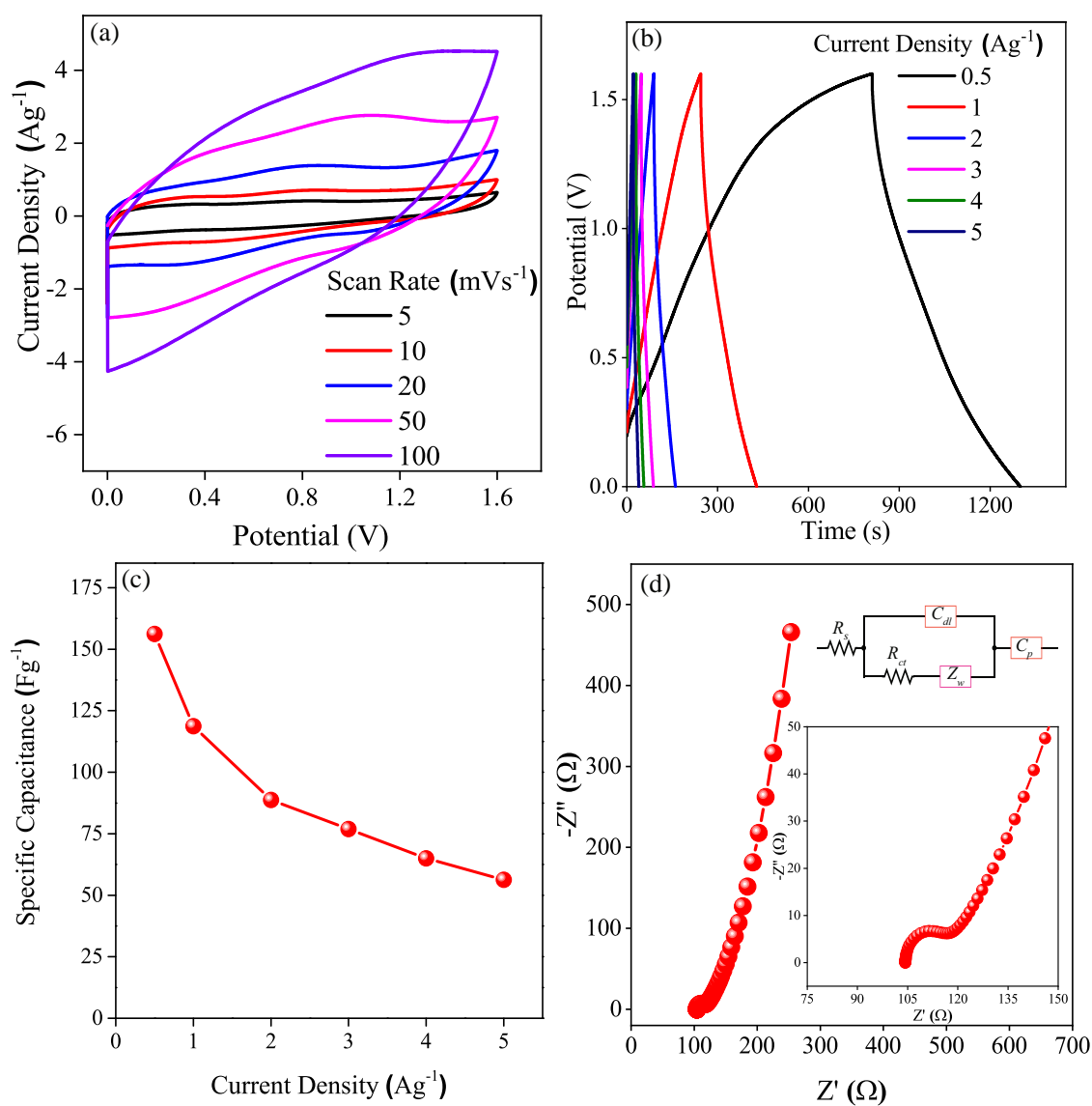


**Fig. 4.17** Electrochemical performance of  $\text{CuCo}_2\text{S}_4\text{-MoS}_2//\text{AC}$  asymmetric device: (a) CV curves at a various scan rates, (b) GCD curves at various current densities, (c) variation of  $C_{sp}$  ( $\text{F g}^{-1}$ ) with increasing current densities and (d) Nyquist plots.



$R_s$  and  $R_{ct}$  values of  $\text{CuCo}_2\text{S}_4\text{-MoS}_2$  confirm its low internal and charge transfer resistance as was also evident from our three-electrode and symmetric two-electrode analyses.

**Table 4.5** Values of  $R_s$ ,  $R_{ct}$ ,  $C_{dl}$ ,  $Z_W$  and  $C_p$  of  $\text{CuCo}_2\text{S}_4\text{-MoS}_2$  in the asymmetric two-electrode system obtained by fitting with equivalent circuit.

$R_s$ ( $\Omega$ )	$R_{ct}$ ( $\Omega$ )	$C_{dl}$ ( $\mu\text{F}$ )	$Z_W$ ( $\Omega$ )	$C_p$ (F)
104.3	11.3	0.1514	0.02038	0.04858

The cyclic stability of the  $\text{CuCo}_2\text{S}_4\text{-MoS}_2//\text{AC}$  supercapacitor was also evaluated by repeating the GCD test 1000 times at a stable current density of  $5 \text{ A g}^{-1}$ . As shown in Fig. 4.18, the fabricated device retained almost 89% of its initial specific capacitance after 1000 cycles, confirming its excellent long-term cyclic stability.

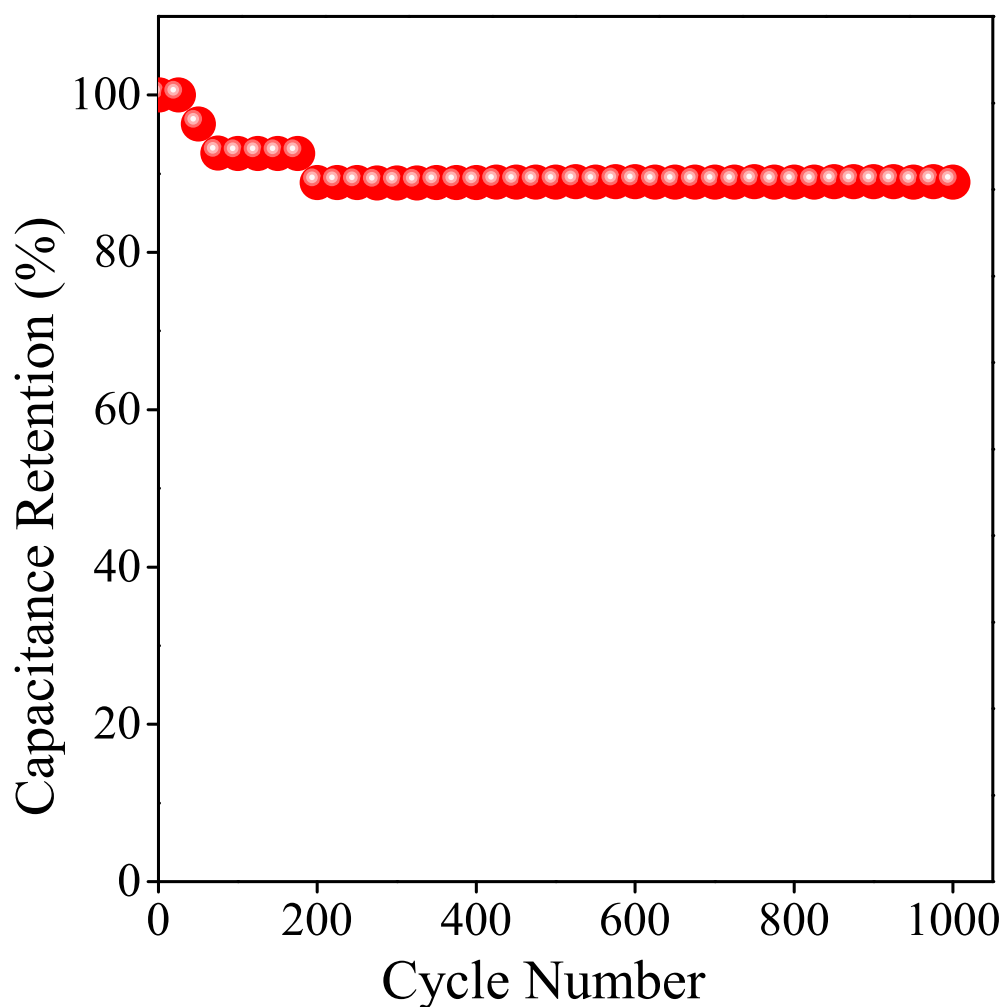


**Fig. 4.18** Retention of specific capacitance retention of  $\text{CuCo}_2\text{S}_4\text{-MoS}_2//\text{AC}$  asymmetric device.

In Fig. 4.19, the Ragone plot of the  $\text{CuCo}_2\text{S}_4\text{-MoS}_2//\text{AC}$  supercapacitor was displayed. As it was observed, the device had delivered a high  $E$  of  $55.56 \text{ Whkg}^{-1}$  at a  $P$  of  $400 \text{ Wkg}^{-1}$ . Even at a higher  $P$  of  $4000 \text{ Wkg}^{-1}$ , the device still had an  $E$  of  $20 \text{ Whkg}^{-1}$ . Further in Table 4.6, a comparative analysis was presented between the electrochemical performance of  $\text{CuCo}_2\text{S}_4\text{-MoS}_2//\text{AC}$  supercapacitor and previously reported analogous asymmetric devices in which AC was used as the negative electrode. Noticeably, both the specific capacitance and energy density of the fabricated device were reasonably higher than that of different  $\text{CuCo}_2\text{S}_4$  and  $\text{CuCo}_2\text{O}_4$  based devices. For instance, Li *et al.* [111] reported that a  $C_{\text{sp}}$  of  $30.5 \text{ Fg}^{-1}$  at  $0.5 \text{ Ag}^{-1}$  and an  $E$  of  $10.2 \text{ Whkg}^{-1}$  at the  $P$  of  $400 \text{ Wkg}^{-1}$  from an asymmetric supercapacitor could be achieved by employing  $\text{CuCo}_2\text{S}_4$  nanocrystals grown on the surface of N and S co-doped reduced graphene oxide ( $\text{CuCo}_2\text{S}_4/\text{N}$ , S-rGO) nanosheets. Conspicuously, at exactly same current and power density, the device displayed improved capacitance and energy density. Notably, another investigation demonstrated that at similar conditions, an asymmetric device assembled using  $\text{CuCo}_2\text{S}_4/\text{carbon}$  nanotubes composite as the positive electrode yielded a  $C_{\text{sp}}$  of  $65.1 \text{ Fg}^{-1}$  and an  $E$  of  $23.2 \text{ Whkg}^{-1}$  which was considerably smaller as compared to the reported device with  $\text{CuCo}_2\text{S}_4\text{-MoS}_2//\text{AC}$  supercapacitor.

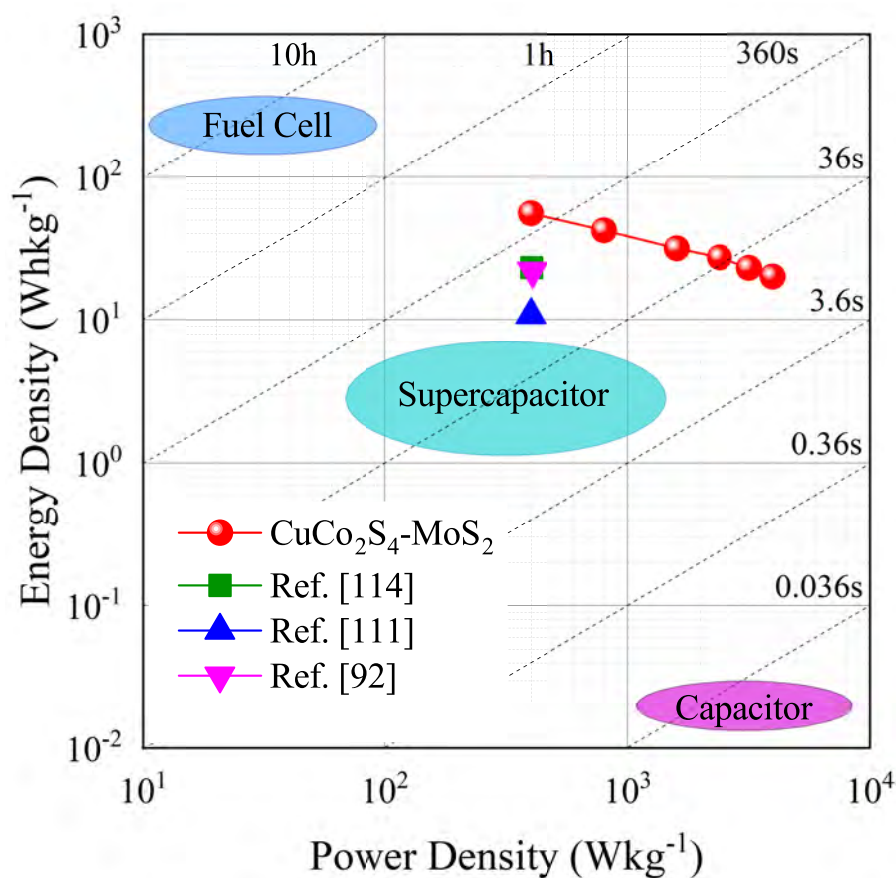


**Fig. 4.19** Ragone plot of  $\text{CuCo}_2\text{S}_4\text{-MoS}_2//\text{AC}$  asymmetric device.

**Table 4.6** Comparison of the asymmetric performance CuCo<sub>2</sub>S<sub>4</sub>-MoS<sub>2</sub> based on previous investigations.

Electrode	Electrolyte	Specific Capacitance (Fg <sup>-1</sup> ) at Current Density (Ag <sup>-1</sup> )	Retention, Cycles	Energy Density (Whkg <sup>-1</sup> ) at Power Density (Wkg <sup>-1</sup> )	Potential window (V)	Ref.
2D multilayer CuCo <sub>2</sub> S <sub>4</sub>	2 M KOH	231 at 1	82% after 10,000 cycles	63.6 at 700	1.6	[112]
CuCo <sub>2</sub> S <sub>4</sub> micro-sphere	3 M KOH	130 at 1	122% after 8,000 cycles	46.2 at 796	1.6	[113]
CuCo <sub>2</sub> S <sub>4</sub> /CNT	2 M KOH	65.1 at 0.5	85.7% after 10,000 cycles	23.2 at 402.7	1.6	[114]
Fl doped CuCo <sub>2</sub> S <sub>4</sub>	1 M KOH	224 at 1	89.2% after 10,000 cycles	49.8 at 897.39	1.6	[115]
CoMoO <sub>4</sub> @CuCo <sub>2</sub> S <sub>4</sub>	3 M KOH	171 at 1	83.3% after 4,000 cycles	60.4 at 800	1.6	[116]
CuCo <sub>2</sub> S <sub>4</sub>	2 M KOH	64 at 0.5	62% after 20,000 cycles	22 at 405	1.62	[92]
NiO@CuCo <sub>2</sub> S <sub>4</sub>	PVA-KOH gel	206 at 1	91% after 5,000 cycles	73 at 802	1.6	[117]
CuCo <sub>2</sub> S <sub>4</sub> nanobelt arrays	6 M KOH	113 at 1	90.89% after 5,000 cycles	40.2 at 800	1.6	[118]
CuCo <sub>2</sub> S <sub>4</sub> /N,S-rGO	2M KOH	30.5 at 0.5	88.9% after 5000 cycles	10.8 at 400	1.6	[111]
CuCo <sub>2</sub> S <sub>4</sub> -MoS <sub>2</sub>	[BMIM][Cl]	156 at 0.5	89% after 1,000 cycles	55.55 at 400	1.6	This work

Finally, to demonstrate a real application, the asymmetric  $\text{CuCo}_2\text{S}_4\text{-MoS}_2//\text{AC}$  device was connected in parallel with an LED as shown in Fig. 4.20 (a). Initially, the device was charged for 120 s at 5 V using an electrometer and then, the electrometer was disconnected. During discharging, the LED was connected and lit up. The LED was utilised to monitor the response of the supercapacitor device. The response of the LED at different times was presented in Fig. 4.20 (b)-(f). Notably, with 120 s of charging, the  $\text{CuCo}_2\text{S}_4\text{-MoS}_2//\text{AC}$  device could light up the LED for 290 s. Hence, the outcomes obtained via all three configurations clearly indicated that the prepared  $\text{CuCo}_2\text{S}_4\text{-MoS}_2$  electrode material could be effectively employed to fabricate highly efficient next generation supercapacitors.

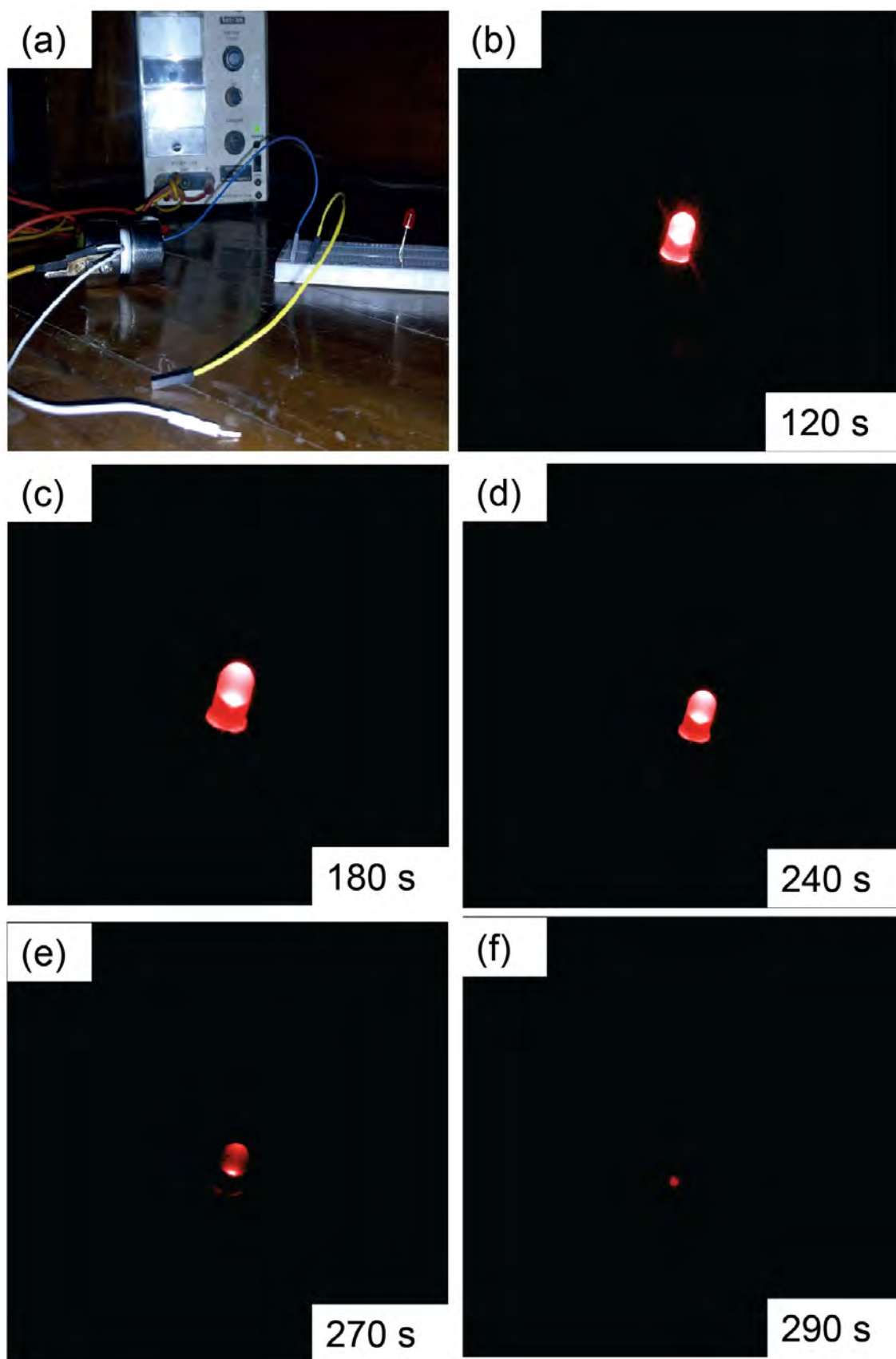


**Fig. 4.20** Snapshots of a practical demonstration of  $\text{CuCo}_2\text{S}_4\text{-MoS}_2//\text{AC}$  device containing prototype supercapacitor system; (a) snapshots of the device setup and connection of the real device for charging. (b-f) photographs of the LED to monitor the discharge process at various times.

## CHAPTER 5

### SUMMARY AND CONCLUSIONS

#### 5.1 Summary

In this investigation,  $\text{CuCo}_2\text{S}_4$  and  $\text{CuCo}_2\text{S}_4\text{-MoS}_2$  nanocomposite were prepared by a facile hydrothermal technique. The outcomes of this investigation are summarised as follows:

- The Rietveld refined powder XRD pattern confirmed the cubic crystal structure of  $\text{CuCo}_2\text{S}_4$  in both samples while  $\text{MoS}_2$  possessed the hexagonal structure in the composite. The absence of any undesired peak due to impurity confirmed the high phase purity of  $\text{CuCo}_2\text{S}_4$  and  $\text{CuCo}_2\text{S}_4\text{-MoS}_2$ .
- The FESEM images showed in-situ growth of  $\text{MoS}_2$  sheets during the hydrothermal process was also observed. The elemental compositions of the  $\text{CuCo}_2\text{S}_4$  and  $\text{CuCo}_2\text{S}_4\text{-MoS}_2$  were in good agreement with the theoretically calculated values.
- TEM investigation confirmed the desired morphology of  $\text{CuCo}_2\text{S}_4\text{-MoS}_2$ . The HRTEM images also demonstrated the coexistence of  $\text{CuCo}_2\text{S}_4$  and  $\text{MoS}_2$ . SAED pattern also confirmed the successful formation of the nanocomposite.
- FTIR demonstrated the presence of individual bonds among the constituents of  $\text{CuCo}_2\text{S}_4$  and  $\text{CuCo}_2\text{S}_4\text{-MoS}_2$ . Additionally, presence of bond between  $\text{CuCo}_2\text{S}_4$  and  $\text{MoS}_2$  was also detected.
- In the three electrode system, CV and GCD showed a significant improvement in capacity and irreversibility for  $\text{CuCo}_2\text{S}_4\text{-MoS}_2$  in comparison with  $\text{CuCo}_2\text{S}_4$  and  $\text{MoS}_2$ . Electrochemical impedance spectroscopy revealed that interfacial resistance between electrode and electrolyte was greatly reduced and this improvement in conductivity resulted in a superior electrochemical performance of  $\text{CuCo}_2\text{S}_4\text{-MoS}_2$  than  $\text{MoS}_2$  and  $\text{CuCo}_2\text{S}_4$ .
- The symmetric two electrode system support the enhancement electrochemical performance of  $\text{CuCo}_2\text{S}_4\text{-MoS}_2$  as demonstrated in three electrode system. Cyclic voltammetry revealed a stable electrochemical process while galvanostatic charge-discharge provided a high stability and retention after a long cyclic charging-discharging for  $\text{CuCo}_2\text{S}_4$ . Energy density of  $\text{CuCo}_2\text{S}_4\text{-MoS}_2$  was also found to be higher than  $\text{CuCo}_2\text{S}_4$  and EIS demonstrated the

improvement in conductivity for  $\text{CuCo}_2\text{S}_4\text{-MoS}_2$  reinforced the results of three electrode system.

- The trend of electrochemical performance of  $\text{CuCo}_2\text{S}_4\text{-MoS}_2$  in an asymmetric device was like the three-electrode and symmetric two-electrode system as explained by CV, GCD and EIS. Moreover, the asymmetric device was used to demonstrate a real-life application to exhibit its practicality.

## 5.2 Conclusions

The electrochemical measurements in the three-electrode and symmetric two-electrode setups demonstrated that the incorporation of a dilute amount of  $\text{MoS}_2$  (10% w/w) nanosheets significantly enhanced the electrochemical performance of ternary  $\text{CuCo}_2\text{S}_4$ . The  $\text{CuCo}_2\text{S}_4\text{-MoS}_2$  electrode exhibited superior charge storage capacity, higher electrical conductivity, better electrochemical stability and reversibility, faster ion transportation rate. It showed significantly larger specific capacitance as compared to the  $\text{CuCo}_2\text{S}_4$  electrode in both symmetric and asymmetric assembly of supercapacitors. The asymmetric supercapacitor constructed using  $\text{CuCo}_2\text{S}_4\text{-MoS}_2$  and activated carbon electrodes delivered a high device capacitance ( $107 \text{ Fg}^{-1}$ ), energy density ( $38.22 \text{ Whkg}^{-1}$ ), large stable potential window (1.6 V) and long cycle life which are superior to those of related  $\text{CuCo}_2\text{S}_4$  and graphene-based asymmetric supercapacitors reported in the literature. Such superior electrochemical performance of  $\text{CuCo}_2\text{S}_4\text{-MoS}_2$  nanocomposite is related to the good crystallinity, high structural stability, enhanced interlayer spacing of  $\text{MoS}_2$  nanosheets present in the nanocomposite and numerous ion transport channels created because of the ultra-small lateral size and thickness of the nanosheets. This work might originate an innovative pathway for the design and fabrication of novel transition metal dichalcogenides based efficient active electrode material for the next generation high-performance supercapacitors.

## 5.3 Scope for Future Work

- Since electrochemical performance depends heavily on the surface morphology, Brunauer–Emmett–Teller (BET) analysis of  $\text{CuCo}_2\text{S}_4$  and  $\text{CuCo}_2\text{S}_4\text{-MoS}_2$  may be carried out to estimate the specific surface area and further confirm the superior surface morphology of  $\text{CuCo}_2\text{S}_4\text{-MoS}_2$ .
- For a better understanding of the chemical binding energies and chemical states of  $\text{CuCo}_2\text{S}_4$  and  $\text{CuCo}_2\text{S}_4\text{-MoS}_2$  X-ray photoelectron spectroscopy analysis can be carried.

- Crystallinity plays an important role regulating electrochemical performance. Annealing at different temperature can be carried out to improve the crystallinity and investigate the effect of it on electrochemical performance of  $\text{CuCo}_2\text{S}_4$  and  $\text{CuCo}_2\text{S}_4\text{-MoS}_2$ .
- The hydrogen evolution reaction (HER) is the cathodic reaction in electrochemical water splitting. HER analysis of  $\text{CuCo}_2\text{S}_4\text{-MoS}_2$  can be carried out to evaluate its suitability to produce hydrogen by water splitting.



## References

- [1] Taiebat, M., Brown, A. L., Safford, H. R., Qu, S., and Xu, M., “A review on energy, environmental, and sustainability implications of connected and automated vehicles”, *Environ. Sci. Technol.*, vol. 52, pp. 11449–11465, 2018.
- [2] Luo, J., Hu, B., Hu, M., Zhao, Y., and Liu, T. L., “Status and prospects of organic redox flow batteries toward sustainable energy storage”, *ACS Energy Lett.*, vol. 4, pp. 2220–2240, 2019.
- [3] Zhou, G., Xu, L., Hu, G., Mai, L., and Cui, Y., “Nanowires for electrochemical energy storage”, *Chem. Rev.*, vol. 119, pp. 11042–11109, 2019.
- [4] Olabi, A. G., “Renewable energy and energy storage systems”, *Energy*, vol. 136, pp. 1–6, 2017.
- [5] Wang, Y. K., Liu, M. C., Cao, J., Zhang, H. J., Kong, L. B., Trudgeon, D. P., Li, X., and Walsh, F. C., “3D hierarchically structured CoS nanosheets: Li<sup>+</sup> storage mechanism and application of the high-performance lithium-ion capacitors”, *ACS Appl. Mater. Interfaces*, vol. 12, pp. 3709–3718, 2019.
- [6] Zhang, Y., Lv, C., Wang, X., Chen, S., Li, D., Peng, Z., and Yang, D., “Boosting sodium-ion storage by encapsulating NiS (CoS) hollow nanoparticles into carbonaceous fibers”, *ACS Appl. Mater. Interfaces*, vol. 10, pp. 40531–40539, 2018.
- [7] Mohammadi, A., Moosavifard, S. E., Goljanian Tabrizi, A., Abdi, M. M., and Karimi, G., “Nanoporous CuCo<sub>2</sub>S<sub>4</sub> microspheres: a novel positive electrode for high-performance hybrid energy storage devices”, *ACS Appl. Energy Mater.*, vol. 2, pp. 627–635, 2018.
- [8] Xiang, C., Liu, Y., Yin, Y., Huang, P., Zou, Y., Fehse, M., She, Z., Xu, F., Banerjee, D., Hermida Merino, D., and others., “Facile green route to Ni/Co oxide nanoparticle embedded 3D graphitic carbon nanosheets for high performance hybrid supercapacitor devices”, *ACS Appl. Energy Mater.*, vol. 2, pp. 3389–3399, 2019.
- [9] Wang, M., Yang, J., Liu, S., Hu, C., and Qiu, J., “Dual hybrid effect endowing nickel-cobalt sulfides with enhanced cycling stability for asymmetrical supercapacitors”, *ACS Appl. Energy Mater.*, vol. 3, pp. 6977–6984, 2020.
- [10] Hou, X., Zhang, Y., Dong, Q., Hong, Y., Liu, Y., Wang, W., Shao, J., Si, W., and Dong, X., “Metal organic framework derived core-shell structured Co<sub>9</sub>S<sub>8</sub>@N-C@MoS<sub>2</sub> nanocubes for supercapacitor”, *ACS Appl. Energy Mater.*, vol. 1, pp. 3513–3520, 2018.
- [11] Yuan, J., Yao, D., Jiang, L., Tao, Y., Che, J., He, G., and Chen, H., “Mn-doped NiMoO<sub>4</sub> mesoporous nanorods/reduced graphene oxide composite for high-performance all-solid-state supercapacitor”, *ACS Appl. Energy Mater.*, vol. 3, pp. 1794–1803, 2020.

- [12] Liu, T., Hou, S., Li, Y., Guo, Y., Yang, C., and Zhao, L., “Tailoring submicron cobblestone-like carbon-free  $\text{CoSe}_2$  with high energy density for sodium-ion batteries”, *ACS Appl. Energy Mater.*, vol. 3, pp. 9558–9567, 2020.
- [13] Miao, C., Xu, P., Zhao, J., Zhu, K., Cheng, K., Ye, K., Yan, J., Cao, D., Wang, G., and Zhang, X., “Binder-free hierarchical urchin-like manganese-cobalt selenide with high electrochemical energy storage performance”, *ACS Appl. Energy Mater.*, vol. 2, pp. 3595–3604, 2019.
- [14] Cheng, C., Zhang, X., Wei, C., Liu, Y., Cui, C., Zhang, Q., and Zhang, D., “Mesoporous hollow  $\text{ZnCo}_2\text{S}_4$  core-shell nanospheres for high performance supercapacitors”, *Ceram. Int.*, vol. 44, pp. 17464–17472, 2018.
- [15] Asadi, R., Azizi, S. N., and Davarani, S. S. H., “Hierarchical  $\text{FeCo}_2\text{S}_4$  nanosheet arrays for high-performance asymmetric supercapacitors”, *J. Mater. Sci.: Mater. Electron.*, vol. 31, pp. 19003–19012, 2020.
- [16] Lee, Y. H., Kang, B. K., Kim, M. S., Choi, H. W., Choi, D. S., Kumar, M., and Yoon, D. H., “Synthesis and characterization of highly uniform  $\text{CuCo}_2\text{S}_4$  ball-in-ball hollow nanospheres as high performance electrode for supercapacitors”, *Phys. Status Solidi A*, vol. 215, p. 1700936, 2018.
- [17] Naveenkumar, P. and Kalaignan, G. P., “Fabrication of core-shell like hybrids of  $\text{CuCo}_2\text{S}_4@ \text{NiCo}(\text{OH})_2$  nanosheets for supercapacitor applications”, *Compos. B. Eng.*, vol. 173, p. 106864, 2019.
- [18] Zhou, Q., Huang, J., Li, C., Lv, Z., Zhu, H., and Hu, G., “Wrapping  $\text{CuCo}_2\text{S}_4$  arrays on nickel foam with  $\text{Ni}_2(\text{CO}_3)(\text{OH})_2$  nanosheets as a high-performance faradaic electrode”, *New J. Chem.*, vol. 43, pp. 5904–5913, 2019.
- [19] Cheng, S., Shi, T., Chen, C., Zhong, Y., Huang, Y., Tao, X., Li, J., Liao, G., and Tang, Z., “Construction of porous  $\text{CuCo}_2\text{S}_4$  nanorod arrays via anion exchange for high-performance asymmetric supercapacitor”, *Sci. Rep.*, vol. 7, pp. 1–11, 2017.
- [20] Tributsch, H. and Bennett, J., “Electrochemistry and photochemistry of  $\text{MoS}_2$  layer crystals. I”, *J. Electroanal. Chem.*, vol. 81, pp. 97–111, 1977.
- [21] Geng, X., Zhang, Y., Han, Y., Li, J., Yang, L., Benamara, M., Chen, L., and Zhu, H., “Two-dimensional water-coupled metallic  $\text{MoS}_2$  with nanochannels for ultrafast supercapacitors”, *Nano Lett.*, vol. 17, pp. 1825–1832, 2017.
- [22] Soares, D. M., Mukherjee, S., and Singh, G., “TMDs beyond  $\text{MoS}_2$  for electrochemical energy storage”, *Chem. Eur. J.*, 2020.
- [23] Luo, W., Zhang, G., Cui, Y., Sun, Y., Qin, Q., Zhang, J., and Zheng, W., “One-step extended strategy for the ionic liquid-assisted synthesis of  $\text{Ni}_3\text{S}_4\text{-MoS}_2$  heterojunction electrodes for supercapacitors”, *J. Mater. Chem. A*, vol. 5, pp. 11278–11285, 2017.
- [24] Ramadoss, A., Kim, T., Kim, G.-S., and Kim, S. J., “Enhanced activity of a hydrothermally synthesized mesoporous  $\text{MoS}_2$  nanostructure for high

- performance supercapacitor applications”, *New J. Chem.*, vol. 38, pp. 2379–2385, 2014.
- [25] Wang, N., Pan, Q., Yang, X., Zhu, H., Ding, G., Jia, Z., Wu, Y., and Zhao, L., “High performance asymmetric supercapacitor based on  $\text{Ni}_x\text{S}_y/\text{MoS}_2$  nanoparticles”, *ACS Appl. Nano Mater.*, vol. 2, pp. 4910–4920, 2019.
- [26] Song, X.-Z., Sun, F.-F., Meng, Y.-L., Wang, Z.-W., Su, Q.-F., and Tan, Z., “Hollow core-shell  $\text{NiCo}_2\text{S}_4@\text{MoS}_2$  dodecahedrons with enhanced performance for supercapacitors and hydrogen evolution reaction”, *New J. Chem.*, vol. 43, pp. 3601–3608, 2019.
- [27] Yang, X., Zhao, L., and Lian, J., “Arrays of hierarchical nickel sulfides/ $\text{MoS}_2$  nanosheets supported on carbon nanotubes backbone as advanced anode materials for asymmetric supercapacitor”, *J. Power Sources*, vol. 343, pp. 373–382, 2017.
- [28] Rui, X., Tan, H., and Yan, Q., “Nanostructured metal sulfides for energy storage”, *Nanoscale*, vol. 6, pp. 9889–9924, 2014.
- [29] Sharma, N., Phase, D., Thotiyl, M. O., and Ogale, S., “Single-phase  $\text{Cu}_3\text{SnS}_4$  nanoparticles for robust high capacity lithium-ion battery anodes”, *ChemElectroChem*, vol. 6, pp. 1371–1375, 2019.
- [30] Tang, J., Ge, Y., Shen, J., and Ye, M., “Facile synthesis of  $\text{CuCo}_2\text{S}_4$  as a novel electrode material for ultrahigh supercapacitor performance”, *Chem. Commun.*, vol. 52, pp. 1509–1512, 2016.
- [31] Peng, H., Ma, G., Mu, J., Sun, K., and Lei, Z., “Controllable synthesis of  $\text{CuS}$  with hierarchical structures via a surfactant-free method for high-performance supercapacitors”, *Mater. Lett.*, vol. 122, pp. 25–28, 2014.
- [32] Wang, Q., Yan, J., Wang, Y., Wei, T., Zhang, M., Jing, X., and Fan, Z., “Three-dimensional flower-like and hierarchical porous carbon materials as high-rate performance electrodes for supercapacitors”, *Carbon*, vol. 67, pp. 119–127, 2014.
- [33] Zhu, Y., Chen, X., Zhou, W., Xiang, K., Hu, W., and Chen, H., “Controllable preparation of highly uniform  $\text{CuCo}_2\text{S}_4$  materials as battery electrode for energy storage with enhanced electrochemical performances”, *Electrochim. Acta*, vol. 249, pp. 64–71, 2017.
- [34] Zequine, C., Bhojate, S., Wang, F., Li, X., Siam, K., Kahol, P. K., and Gupta, R. K., “Effect of solvent for tailoring the nanomorphology of multinary  $\text{CuCo}_2\text{S}_4$  for overall water splitting and energy storage”, *J. Alloys Compd.*, vol. 784, pp. 1–7, 2019.
- [35] Zhang, Y., Xu, J., Zhang, Y., Zheng, Y., Hu, X., and Liu, Z., “Facile fabrication of flower-like  $\text{CuCo}_2\text{S}_4$  on Ni foam for supercapacitor application”, *J. Mater. Sci.*, vol. 52, pp. 9531–9538, 2017.

- [36] Du, J., Yan, Q., Li, Y., Cheng, K., Ye, K., Zhu, K., Yan, J., Cao, D., Zhang, X., and Wang, G., “Hierarchical copper cobalt sulfides nanowire arrays for high-performance asymmetric supercapacitors”, *Appl. Surf. Sci.*, vol. 487, pp. 198–205, 2019.
- [37] Moosavifard, S. E., Fani, S., and Rahmanian, M., “Hierarchical  $\text{CuCo}_2\text{S}_4$  hollow nanoneedle arrays as novel binder-free electrodes for high-performance asymmetric supercapacitors”, *Chem. Commun.*, vol. 52, pp. 4517–4520, 2016.
- [38] Wang, Y., Yang, D., Zhou, T., Pan, J., Wei, T., and Sun, Y., “Oriented  $\text{CuCo}_2\text{S}_4$  nanograss arrays/Ni foam as an electrode for a high-performance all-solid-state supercapacitor”, *Nanotechnology*, vol. 28, p. 465402, 2017.
- [39] Dong, Y., He, K., Yin, L., and Zhang, A., “A facile route to controlled synthesis of  $\text{Co}_3\text{O}_4$  nanoparticles and their environmental catalytic properties”, *Nanotechnology*, vol. 18, p. 435602, 2007.
- [40] Anil Kumar, Y., Srinivasa Rao, S., Punnoose, D., Venkata Tulasivarma, C., Gopi, C. V., Prabakar, K., and Kim, H. J., “Influence of solvents in the preparation of cobalt sulfide for supercapacitors”, *R. Soc. Open Sci.*, vol. 4, p. 170427, 2017.
- [41] Folkman, S. J., Zhou, M., Nicki, M., and Finke, R. G., “Alcohol solvent effects in the synthesis of  $\text{Co}_3\text{O}_4$  metal-oxide nanoparticles: Disproof of a surface-ligand thermodynamic effect en route to alternative kinetic and thermodynamic explanations”, *Inorg. Chem.*, vol. 57, pp. 1517–1526, 2018.
- [42] Guo, S. H., Chen, W. Q., Li, M., Wang, J., Liu, F., and Cheng, J. P., “Effect of reaction temperature on the amorphous-crystalline transition of copper cobalt sulfide for supercapacitors”, *Electrochim. Acta*, vol. 271, pp. 498–506, 2018.
- [43] Arrhenius, S., “Über die dissociationswärme und den einfluss der temperatur auf den dissociationsgrad der elektrolyte”, *Zeitschrift für physikalische Chemie*, vol. 4, pp. 96–116, 1889.
- [44] Wang, L., Yang, H., Shu, T., Chen, X., Huang, Y., and Hu, X., “Rational design of three-dimensional hierarchical nanomaterials for asymmetric supercapacitors”, *ChemElectroChem*, vol. 4, pp. 2428–2441, 2017.
- [45] Hu, L., Deng, Y., Liang, K., Liu, X., and Hu, W., “ $\text{LaNiO}_3/\text{NiO}$  hollow nanofibers with mesoporous wall: a significant improvement in NiO electrodes for supercapacitors”, *J. Solid State Electrochem.*, vol. 19, pp. 629–637, 2015.
- [46] Ma, K., Liu, F., Zhang, M., Zhang, X. B., and Cheng, J. P., “Core/shell microrod arrays of NiO/Co-Fe layered double hydroxides deposited on nickel foam for energy storage and conversion”, *Electrochim. Acta*, vol. 225, pp. 425–434, 2017.
- [47] Annamalai, K., Tao, Y.-s., and others., “A hierarchically porous  $\text{CuCo}_2\text{S}_4$ /graphene composite as an electrode material for supercapacitors”, *New Carbon Mater.*, vol. 31, pp. 336–342, 2016.

- [48] Wang, Z., Zhu, Z., Zhang, Q., Zhai, M., Gao, J., Chen, C., and Yang, B., “Fabrication of N-doped carbon coated spinel copper cobalt sulfide hollow spheres to realize the improvement of electrochemical performance for supercapacitors”, *Ceram. Int.*, vol. 45, pp. 21286–21292, 2019.
- [49] Ge, Y., Wu, J., Xu, X., Ye, M., and Shen, J., “Facile synthesis of  $\text{CoNi}_2\text{S}_4$  and  $\text{CuCo}_2\text{S}_4$  with different morphologies as prominent catalysts for hydrogen evolution reaction”, *Int. J. Hydrog. Energy*, vol. 41, pp. 19847–19854, 2016.
- [50] Tian, Z., Wang, X., Li, B., Li, H., and Wu, Y., “High rate capability electrode constructed by anchoring  $\text{CuCo}_2\text{S}_4$  on graphene aerogel skeleton toward quasi-solid-state supercapacitor”, *Electrochim. Acta*, vol. 298, pp. 321–329, 2019.
- [51] Ma, L., Chen, T., Li, S., Gui, P., and Fang, G., “A 3D self-supported coralline-like  $\text{CuCo}_2\text{S}_4@ \text{NiCo}_2\text{S}_4$  core-shell nanostructure composite for high-performance solid-state asymmetrical supercapacitors”, *Nanotechnology*, vol. 30, p. 255603, 2019.
- [52] Zhao, G., Zhang, Y., Yang, L., Jiang, Y., Zhang, Y., Hong, W., Tian, Y., Zhao, H., Hu, J., Zhou, L., and others., “Nickel chelate derived  $\text{NiS}_2$  decorated with bifunctional carbon: an efficient strategy to promote sodium storage performance”, *Adv. Funct. Mater.*, vol. 28, p. 1803690, 2018.
- [53] Xu, X., Liu, Y., Dong, P., Ajayan, P. M., Shen, J., and Ye, M., “Mesosstructured  $\text{CuCo}_2\text{S}_4/\text{CuCo}_2\text{O}_4$  nanoflowers as advanced electrodes for asymmetric supercapacitors”, *J. Power Sources*, vol. 400, pp. 96–103, 2018.
- [54] Parveen, N., Ansari, S. A., Alamri, H. R., Ansari, M. O., Khan, Z., and Cho, M. H., “Facile synthesis of  $\text{SnS}_2$  nanostructures with different morphologies for high-performance supercapacitor applications”, *ACS Omega*, vol. 3, pp. 1581–1588, 2018.
- [55] Choudhary, N., Li, C., Chung, H.-S., Moore, J., Thomas, J., and Jung, Y., “High-performance one-body core/shell nanowire supercapacitor enabled by conformal growth of capacitive 2D  $\text{WS}_2$  layers”, *ACS Nano*, vol. 10, pp. 10726–10735, 2016.
- [56] Feng, J., Sun, X., Wu, C., Peng, L., Lin, C., Hu, S., Yang, J., and Xie, Y., “Metallic few-layered  $\text{VS}_2$  ultrathin nanosheets: high two-dimensional conductivity for in-plane supercapacitors”, *J. Am. Chem. Soc.*, vol. 133, pp. 17832–17838, 2011.
- [57] Tang, C., Min, Y., Chen, C., Xu, W., and Xu, L., “Potential applications of heterostructures of TMDs with MXenes in Sodium-Ion and Na- $\text{O}_2$  batteries”, *Nano Lett.*, vol. 19, pp. 5577–5586, 2019.
- [58] Sharma, K., Arora, A., Tripathi, S. K., and others., “Review of supercapacitors: Materials and devices”, *J. Energy Storage*, vol. 21, pp. 801–825, 2019.
- [59] Raza, W., Ali, F., Raza, N., Luo, Y., Kim, K.-H., Yang, J., Kumar, S., Mehmood, A., and Kwon, E. E., “Recent advancements in supercapacitor technology”, *Nano Energy*, vol. 52, pp. 441–473, 2018.

- [60] Iro, Z. S., Subramani, C., and Dash, S., “A brief review on electrode materials for supercapacitor”, *Int. J. Electrochem. Sci.*, vol. 11, pp. 10628–10643, 2016.
- [61] Augustyn, V., Simon, P., and Dunn, B., “Pseudocapacitive oxide materials for high-rate electrochemical energy storage”, *Energy Environ. Sci.*, vol. 7, pp. 1597–1614, 2014.
- [62] Lu, Z., Chang, Z., Zhu, W., and Sun, X., “Beta-phased ni (oh)<sub>2</sub> nanowall film with reversible capacitance higher than theoretical faradic capacitance”, *ChemComm.*, vol. 47, pp. 9651–9653, 2011.
- [63] Xie, J., Sun, X., Zhang, N., Xu, K., Zhou, M., and Xie, Y., “Layer-by-layer  $\beta$ -ni (oh)<sub>2</sub>/graphene nanohybrids for ultraflexible all-solid-state thin-film supercapacitors with high electrochemical performance”, *Nano Energy*, vol. 2, pp. 65–74, 2013.
- [64] Stoller, M. D., Park, S., Zhu, Y., An, J., and Ruoff, R. S., “Graphene-based ultracapacitors”, *Nano Lett.*, vol. 8, pp. 3498–3502, 2008.
- [65] Das, S., Dutta, S., Tama, A. M., and Basith, M. A., “Nanostructured LaFeO<sub>3</sub>-MoS<sub>2</sub> for efficient photodegradation and photocatalytic hydrogen evolution”, *Mater. Sci. Eng. B*, vol. 271, p. 115295, 2021.
- [66] Tama, A. M., Das, S., Dutta, S., Bhuyan, M. D. I., Islam, M. N., and Basith, M. A., “MoS<sub>2</sub> nanosheet incorporated  $\alpha$ -Fe<sub>2</sub>O<sub>3</sub>/ZnO nanocomposite with enhanced photocatalytic dye degradation and hydrogen production ability”, *RSC Adv.*, vol. 9, pp. 40357–40367, 2019.
- [67] Mitzi, D. B., Feild, C., Schlesinger, Z., and Laibowitz, R., “Transport, optical, and magnetic properties of the conducting halide perovskite CH<sub>3</sub>NH<sub>3</sub>SnI<sub>3</sub>”, *J. Solid State Chem.*, vol. 114, pp. 159–163, 1995.
- [68] Rietveld, H. M., “A profile refinement method for nuclear and magnetic structures”, *J. Appl. Crystallogr.*, vol. 2, pp. 65–71, 1969.
- [69] Rietveld, H. M., “The rietveld method”, *Phys. Scr.*, vol. 89, p. 098002, 2014.
- [70] Toby, B. H., “R factors in Rietveld analysis: How good is good enough?”, *Powder Diffr.*, vol. 21, pp. 67–70, 2006.
- [71] Goldstein, J. I., Newbury, D. E., Michael, J. R., Ritchie, N. W. M., Scott, J. H. J., and Joy, D. C., *Scanning electron microscopy and X-ray microanalysis*, Springer, 2017.
- [72] Kirkland, E. J., *The Transmission Electron Microscope*, pp. 5–18, Boston, MA: Springer US, 1998.
- [73] Salzer, R., “Peter R. Griffiths, James A. de Haseth: Fourier transform infrared spectrometry (2nd edn.)”, *Anal. Bioanal. Chem.*, vol. 391, pp. 2379–2380, 2008.
- [74] Burns, J. C., Krause, L. J., Le, D.-B., Jensen, L. D., Smith, A. J., Xiong, D., and Dahn, J. R., “Introducing symmetric Li-ion cells as a tool to study cell degradation mechanisms”, *J. Electrochem. Soc.*, vol. 158, p. A1417, 2011.

- [75] Roy, C. K., Shah, S. S., Reaz, A. H., Sultana, S., Chowdhury, A.-N., Firoz, S. H., Zahir, M. H., Ahmed Qasem, M. A., and Aziz, M. A., “Preparation of hierarchical porous activated carbon from banana leaves for high-performance supercapacitor: Effect of type of electrolytes on performance”, *Chem. Asian J.*, vol. 16, pp. 296–308, 2021.
- [76] Zhang, J., Jiang, J., and Zhao, X. S., “Synthesis and capacitive properties of manganese oxide nanosheets dispersed on functionalized graphene sheets”, *J. Phys. Chem. C*, vol. 115, pp. 6448–6454, 2011.
- [77] Langhus, D. L., “Analytical Electrochemistry, 2nd Edition (Wang, Joseph)”, *J. Chem. Educ.*, vol. 78, p. 457, 2001.
- [78] Liu, Y. F., Yuan, G. H., Jiang, Z. H., and Yao, Z. P., “Solvothermal synthesis of Mn<sub>3</sub>O<sub>4</sub> nanoparticle/graphene sheet composites and their supercapacitive properties”, *J. Nanomater.*, vol. 2014, 2014.
- [79] Zhao, X., Hou, Y., Wang, Y., Yang, L., Zhu, L., Cao, R., and Sha, Z., “Prepared MnO<sub>2</sub> with different crystal forms as electrode materials for supercapacitors: experimental research from hydrothermal crystallization process to electrochemical performances”, *RSC adv.*, vol. 7, pp. 40286–40294, 2017.
- [80] Ghosh, K., Yue, C. Y., Sk, M. M., Jena, R. K., and Bi, S., “Development of a 3d graphene aerogel and 3D porous graphene/MnO<sub>2</sub>@polyaniline hybrid film for all-solid-state flexible asymmetric supercapacitors”, *Sustain. Energy Fuels*, vol. 2, pp. 280–293, 2018.
- [81] Lei, X., Ge, S., Tan, Y., Wang, Z., Li, J., Li, X., Hu, G., Zhu, X., Huang, M., Zhu, Y., and others., “High capacity and energy density of Zn-Ni-Co-P nanowire arrays as an advanced electrode for aqueous asymmetric supercapacitor”, *ACS Appl. Mater. Interfaces*, vol. 12, pp. 9158–9168, 2020.
- [82] Ragone, D. V., “Review of battery systems for electrically powered vehicles”, in *Mid-Year Meeting*, SAE International, feb 1968.
- [83] González, A., Goikolea, E., Barrena, J. A., and Mysyk, R., “Review on supercapacitors: Technologies and materials”, *Renew. Sustain. Energy Rev.*, vol. 58, pp. 1189–1206, 2016.
- [84] Winter, M. and Brodd, R. J., “What are batteries, fuel cells, and supercapacitors?”, *Chem. Rev.*, vol. 104, pp. 4245–4270, 2004.
- [85] Gao, Z., Wang, J., Li, Z., Yang, W., Wang, B., Hou, M., He, Y., Liu, Q., Mann, T., Yang, P., and others., “Graphene nanosheet/Ni<sup>2+</sup>/Al<sup>3+</sup> layered double-hydroxide composite as a novel electrode for a supercapacitor”, *Chem. Mater.*, vol. 23, pp. 3509–3516, 2011.
- [86] Rodriguez-Carvajal, J., “FULLPROF: a program for Rietveld refinement and pattern matching analysis”, in *satellite meeting on powder diffraction of the XV congress of the IUCr*, vol. 127, Toulouse, France:[sn], 1990.

- [87] Basith, M. A., Islam, M. A., Ahmmad, B., Hossain, M. S., and Mølhave, K., “Preparation of high crystalline nanoparticles of rare-earth based complex perovskites and comparison of their structural and magnetic properties with bulk counterparts”, *Mater. Res. Express*, vol. 4, p. 075012, 2017.
- [88] Oda, T., Shirai, M., Suzuki, N., and Motizuki, K., “Electronic band structure of sulphide spinels  $\text{CuM}_2\text{S}_4$  (M= Co, Rh, Ir)”, *J. Condens. Matter Phys.*, vol. 7, p. 4433, 1995.
- [89] Li, L., Xu, J., Ma, J., Liu, Z., and Li, Y., “A bimetallic sulfide  $\text{CuCo}_2\text{S}_4$  with good synergistic effect was constructed to drive high performance photocatalytic hydrogen evolution”, *J. Colloid Interface Sci.*, vol. 552, pp. 17–26, 2019.
- [90] Xu, J.-M., Wang, X.-C., and Cheng, J.-P., “Supercapacitive performances of ternary  $\text{CuCo}_2\text{S}_4$  sulfides”, *ACS Omega*, vol. 5, pp. 1305–1311, 2020.
- [91] Wang, Z., Ma, L., Chen, W., Huang, G., Chen, D., Wang, L., and Lee, J. Y., “Facile synthesis of  $\text{MoS}_2$ /graphene composites: effects of different cationic surfactants on microstructures and electrochemical properties of reversible lithium storage”, *RSC Adv.*, vol. 3, pp. 21675–21684, 2013.
- [92] Cheng, J. P., Gao, S. Q., Zhang, P. P., Wang, B. Q., Wang, X. C., and Liu, F., “Influence of crystallinity of  $\text{CuCo}_2\text{S}_4$  on its supercapacitive behavior”, *J. Alloys Compd.*, vol. 825, p. 153984, 2020.
- [93] Sheng, Y., Tang, X., Peng, E., and Xue, J., “Graphene oxide based fluorescent nanocomposites for cellular imaging”, *J. Mater. Chem. B*, vol. 1, pp. 512–521, 2013.
- [94] Yu, L., Hu, H., Wu, H. B., and Lou, X. W., “Complex hollow nanostructures: synthesis and energy-related applications”, *Adv. Mater.*, vol. 29, p. 1604563, 2017.
- [95] Nai, J. and Lou, X. W., “Hollow structures based on prussian blue and its analogs for electrochemical energy storage and conversion”, *Adv. Mater.*, vol. 31, p. 1706825, 2019.
- [96] Das, S., Sultana, I., Bhuyan, M. D. I., and Basith, M. A., “Enhanced magnetic softness of double-layered perovskite manganite  $\text{La}_{1.7}\text{Gd}_{0.3}\text{SrMn}_2\text{O}_7$ ”, *IEEE Magn. Lett.*, vol. 10, pp. 1–4, 2019.
- [97] Chavez, C. A., Antonio, J. A. T., and Jacome, M. A. C., *Chemical Quantification of Mo-S, W-Si and Ti-V by Energy Dispersive X-Ray Spectroscopy*, Rijeka: IntechOpen, 2012.
- [98] Shen, J., Tang, J., Dong, P., Zhang, Z., Ji, J., Baines, R., and Ye, M., “Construction of three-dimensional  $\text{CuCo}_2\text{S}_4$ /CNT/graphene nanocomposite for high performance supercapacitors”, *RSC Adv.*, vol. 6, pp. 13456–13460, 2016.



- [99] Das, S., Tama, A. M., Dutta, S., Ali, M. S., and Basith, M. A., “Facile high-yield synthesis of MoS<sub>2</sub> nanosheets with enhanced photocatalytic performance using ultrasound driven exfoliation technique”, *Mater. Res. Express*, vol. 6, p. 125079, 2019.
- [100] Lv, X., Huang, W., Shi, Q., Tang, L., and Tang, J., “Synthesis of amorphous NiCo<sub>z</sub>V<sub>x</sub>O<sub>y</sub> nanosphere as a positive electrode materials via a facile route for asymmetric supercapacitors”, *J. Power Sources*, vol. 492, p. 229623, 2021.
- [101] Pan, Z., Chen, H., Yang, J., Ma, Y., Zhang, Q., Kou, Z., Ding, X., Pang, Y., Zhang, L., Gu, Q., and others., “CuCo<sub>2</sub>S<sub>4</sub> nanosheets@N-doped carbon nanofibers by sulfurization at room temperature as bifunctional electrocatalysts in flexible quasi-solid-state zn-air batteries”, *Adv. Sci.*, vol. 6, p. 1900628, 2019.
- [102] Lin, J.-H., “The influence of the interlayer distance on the performance of thermally reduced graphene oxide supercapacitors”, *Materials*, vol. 11, p. 263, 2018.
- [103] Nardekar, S. S., Krishnamoorthy, K., Pazhamalai, P., Sahoo, S., Mariappan, V. K., and Kim, S.-J., “Exceptional interfacial electrochemistry of few-layered 2D MoS<sub>2</sub> quantum sheets for high performance flexible solid-state supercapacitors”, *J. Mater. Chem. A*, vol. 8, pp. 13121–13131, 2020.
- [104] Wu, Y. and Cao, C., “The way to improve the energy density of supercapacitors: Progress and perspective”, *Sci. China Mater.*, vol. 61, pp. 1517–1526, 2018.
- [105] Saeed, G., Bandyopadhyay, P., Kumar, S., Kim, N. H., and Lee, J. H., “ZnS-Ni<sub>7</sub>S<sub>6</sub> nanosheet arrays wrapped with nanopetals of Ni(OH)<sub>2</sub> as a novel core-shell electrode material for asymmetric supercapacitors with high energy density and cycling stability performance”, *ACS Appl. Mater. Interfaces*, vol. 12, pp. 47377–47388, 2020.
- [106] Huang, S., Zhu, X., Sarkar, S., and Zhao, Y., “Challenges and opportunities for supercapacitors”, *APL Mater.*, vol. 7, p. 100901, 2019.
- [107] Huang, Y., Zeng, Y., Yu, M., Liu, P., Tong, Y., Cheng, F., and Lu, X., “Recent smart methods for achieving high-energy asymmetric supercapacitors”, *Small Methods*, vol. 2, p. 1700230, 2018.
- [108] Moitra, D., Anand, C., Ghosh, B. K., Chandel, M., and Ghosh, N. N., “One-dimensional BiFeO<sub>3</sub> nanowire-reduced graphene oxide nanocomposite as excellent supercapacitor electrode material”, *ACS Appl. Energy Mater.*, vol. 1, pp. 464–474, 2018.
- [109] Huang, Y.-Y. and Lin, L.-Y., “Synthesis of ternary metal oxides for battery-supercapacitor hybrid devices: influences of metal species on redox reaction and electrical conductivity”, *ACS Appl. Energy Mater.*, vol. 1, pp. 2979–2990, 2018.

- [110] Liang, H., Lin, J., Jia, H., Chen, S., Qi, J., Cao, J., Lin, T., Fei, W., and Feng, J., “Hierarchical NiCo-LDH/NiCoP@ NiMn-LDH hybrid electrodes on carbon cloth for excellent supercapacitors”, *J. Mater. Chem. A*, vol. 6, pp. 15040–15046, 2018.
- [111] Li, Z., Lv, H., Wang, Z., Gu, A., He, X., and Wang, L., “In situ growth of  $\text{CuCo}_2\text{S}_4$  nanocrystals on N, S-codoped reduced graphene oxide nanosheets for supercapacitors”, *Mater. Res. Express*, vol. 6, p. 085523, 2019.
- [112] Jiang, J., Chen, Y., Hu, X., Cong, H., Zhou, Q., Rong, H., Sun, Y., and Han, S., “Designed synthesis of 2D multilayer  $\text{CuCo}_2\text{S}_4$  nanomaterials for high-performance asymmetric supercapacitors”, *Vacuum*, vol. 182, p. 109698, 2020.
- [113] Xie, T., Xu, J., Wang, J., Ma, C., Su, L., Dong, F., and Gong, L., “In situ preparation of flaky attached  $\text{CuCo}_2\text{S}_4$  microspheres for high-performance asymmetric supercapacitors”, *Ionics*, vol. 26, pp. 3555–3563, 2020.
- [114] Li, H., Li, Z., Wu, Z., Sun, M., Han, S., Cai, C., Shen, W., Liu, X., and Fu, Y., “Enhanced electrochemical performance of  $\text{CuCo}_2\text{S}_4$ /carbon nanotubes composite as electrode material for supercapacitors”, *J. Colloid Interface Sci.*, vol. 549, pp. 105–113, 2019.
- [115] Kang, L., Huang, C., Zhang, J., Zhang, M., Zhang, N., Liu, S., Ye, Y., Luo, C., Gong, Z., Wang, C., and others., “Effect of fluorine doping and sulfur vacancies of  $\text{CuCo}_2\text{S}_4$  on its electrochemical performance in supercapacitors”, *Chem. Eng. Sci.*, vol. 390, p. 124643, 2020.
- [116] Xie, T., Xu, J., Wang, J., Xuan, C., Ma, C., Su, L., Dong, F., and Gong, L., “In situ growth of core-shell heterostructure  $\text{CoMoO}_4$ @ $\text{CuCo}_2\text{S}_4$  meshes as advanced electrodes for high-performance supercapacitors”, *Energy Fuels*, vol. 34, pp. 16791–16799, 2020.
- [117] Wang, S., Fang, S., Zhang, K., Zou, Y., Xiao, Z., Xu, F., Sun, L., and Xiang, C., “Growth of yolk-shell  $\text{CuCo}_2\text{S}_4$  on NiO nanosheets for high-performance flexible supercapacitors”, *Ceram. Int.*, 2021.
- [118] Han, L., Liu, X., Cui, Z., Hua, Y., Wang, C., Zhao, X., and Liu, X., “Hierarchical copper cobalt sulfide nanobelt arrays for high performance asymmetric supercapacitors”, *Inorganic Chemistry Frontiers*, 2021.

## List of publications

### List of publication as a co-author

- [1] Noor, M., Sharmin, F., Mamun, M. A., **Hasan, S.**, Hakim, M., and Basith, M. A., “Effect of Gd and Y co-doping in BiVO<sub>4</sub> photocatalyst for enhanced degradation of methylene blue dye”, *J. Alloys Compd.*, p. 162639, 2021

### Conference presentations

- [1] **Hasan, S.**, Reaz, A. H., Das, S., Roy, C. K. and Basith, M. A., “Investigation of CuCo<sub>2</sub>S<sub>4</sub>-MoS<sub>2</sub> Nanocomposite as Electrode Material for Supercapacitor”, Poster presentation, National Conference on Physics-2021, 06-07 August 2021 (Awarded, **Best Oral Presentation Award**, Nanomaterials session).
- [2] **Hasan S.** , Zaman S. and Basith M. A. , “Powder MoS<sub>2</sub> as Electrode Material for Supercapacitors”, Oral presentation, International Conference on Physics - 2020, 05-07 March, 2020.